6. SENSITIVITY STUDIES

As in every numerical simulation of a groundwater system, the modeling of Amchitka Island is conducted in the face of significant uncertainties. Where data allowed, uncertainty in critical parameter values was incorporated directly in the modeling process. Performing the modeling with mean values and distributions of important parameters allows the uncertainty in those parameters to be accounted for and carried into the subsequent risk assessment through a standard deviation in the breakthrough curves. However, some uncertainties cannot be addressed through that process, either due to a lack of data from which to derive means and distributions (as in the case of the matrix diffusion parameter), or because the uncertainty is in the underlying conceptual model or numerical approach. A variety of sensitivity analyses are presented now to address some of these issues. The first set of sensitivity problems can be addressed using the two-dimensional model formulation presented in the previous section. The second set requires expanding the model into the third dimension.

6.1 Two-dimensional Sensitivity Studies

The two-dimensional FEFLOW formulation of the three sites is used to evaluate the following topics: issues related to the numerical solution of the transport problem, the sensitivity of transport results to the matrix diffusion coefficient, the possibility of transport by colloids, the impact of the island half-width on the model, and finally, the possible system response to sea level change.

6.1.1 Numerical Solution Issues

The density variations due to the saltwater intrusion problem lead to a spatially varying velocity field as shown in Figure 6.1 and Figure 6.2. The velocity values are only known at specific points according to the finite-element solution of the flow problem. These points do not form a uniform grid, as would be the case in the finite difference models. For computational convenience, we grid the non-uniformly spaced velocity vectors using nearest-neighbor interpolation and obtain the velocity vectors at a uniformly-spaced two-dimensional grid. This facilitates the interpolation of the velocity needed for determining particle velocity for radionuclide transport simulations. Particle velocity needs to be interpolated from the surrounding known velocity values. A number of studies dealt with the velocity interpolation and presented different alternatives for computing particle velocity in purely advective transport regimes. These include, but are not limited to, Pollock (1988), Goode (1990), Schafer-Perini and Wilson (1991) and LaBolle et al. (1996). The common result of these approaches is that for heterogeneous media, the linear and bilinear interpolation schemes yield similar results [e.g., Goode (1990, Fig. 17) and LaBolle et al. (1996, Figs. 12-14)]. Although we do not consider medium heterogeneity, the salinity variability leads to heterogeneous velocity distribution for which the interpolation schemes need to be evaluated.

First, we check the aspects of the velocity gridding and interpolation. The accuracy of the conversion of the non-uniformly spaced velocity vectors into uniform grid values is evaluated in Figures 6.1 and 6.2. In these figures, we compare the original velocity vectors obtained from FEFLOW on the finite-element mesh to the interpolated-velocity (or the gridded-velocity) streamlines. As can be seen from different insets in the figures, the streamlines obtained from the
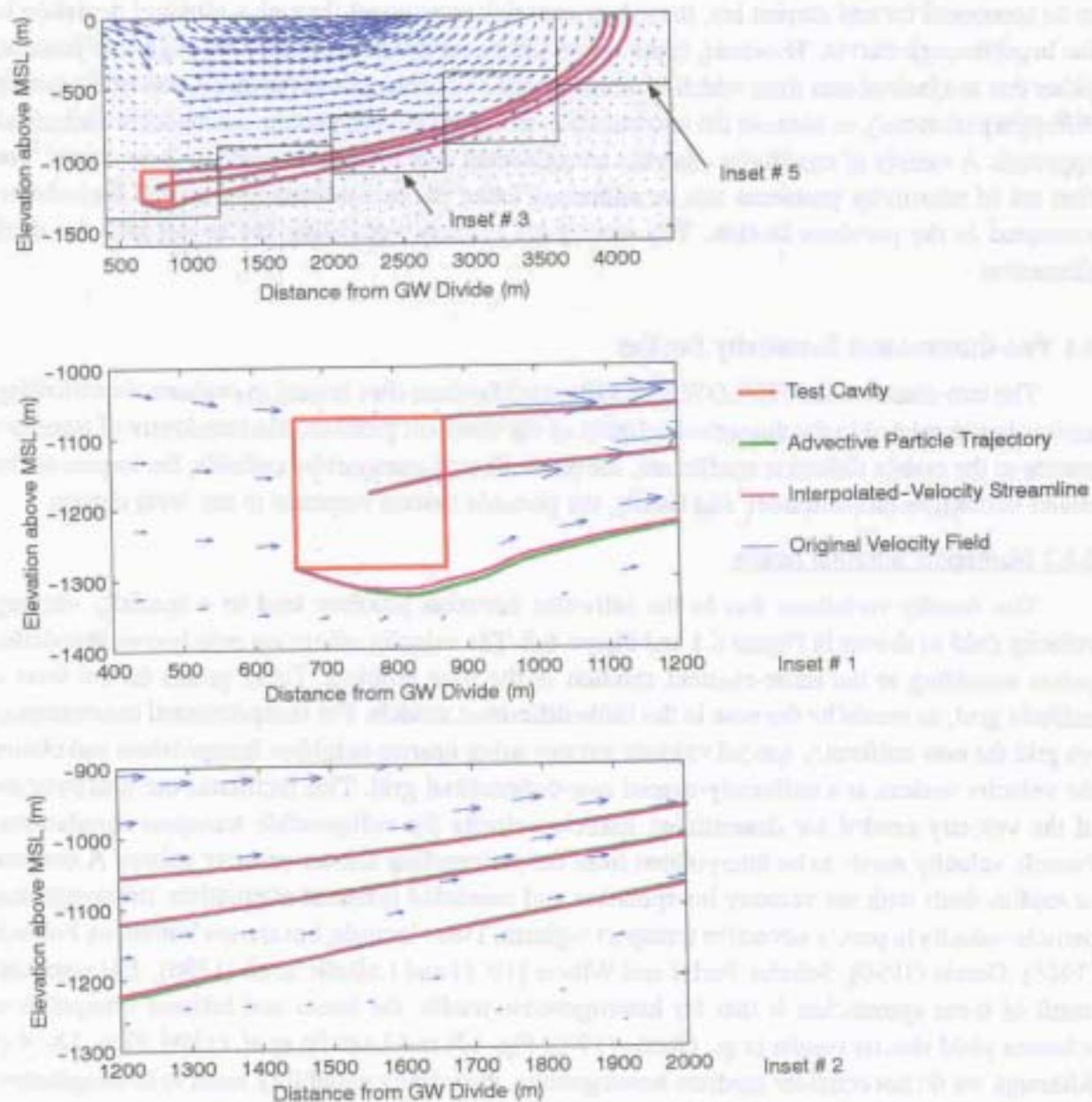
Figure 6.1.   Comparison between original velocity streamlines, gridded (or interpolated) velocity streamlines and advective particle trajectory for the entire travel distance and two areas of inset.
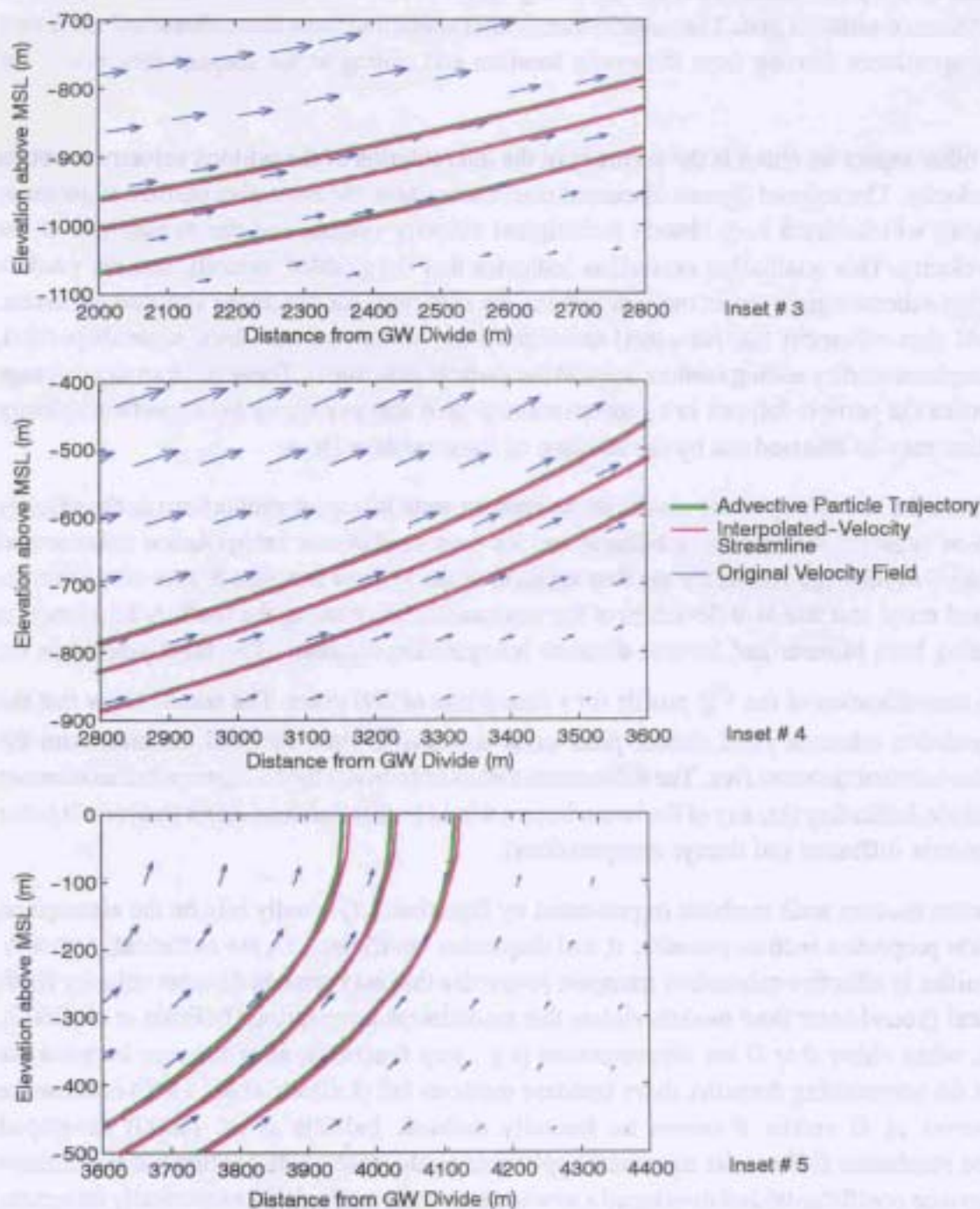
Figure 6.2.   Comparison between original velocity streamlines, gridded (or interpolated) velocity streamlines and advective particle trajectory for the three areas of inset closest to the seafloor as shown in Figure 6.1.

interpolated velocity (magenta lines) are following very closely the original velocity vectors (blue arrows) of the non-uniform grid. The velocity vectors run parallel to these streamlines and show very good correspondence starting from the cavity location and ending at the seepage face across the seafloor.

The other aspect we check is the accuracy of the interpolation of the gridded velocity to obtain particle velocity. The colored figures discussed above also show the advective particle trajectories (green lines), which match very closely the original velocity vectors and the streamlines of the gridded velocity. This qualitative evaluation indicates that the gridded velocity and the particle interpolation scheme employed in our simulations are sufficient for obtaining accurate estimates. One should also remember that the actual simulations are performed with local-scale dispersion, which is implemented by adding random steps to the particle movement. These random steps change the streamline the particle follows in a random manner such that any errors in the particle velocity interpolation may be smeared out by the addition of these random steps.

To check the sensitivity of the results of the random walk transport simulations to the velocity interpolation scheme, we employ a bilinear and an inverse distance interpolation scheme and compare the breakthrough results for the first scenario of the Milrow settings. Figure 6.3 shows the non-decayed mean and standard deviation of the total mass flux crossing the seafloor as a function of time using both bilinear and inverse-distance interpolation schemes. The third subplot in the figure is a magnification of the $^\sigma Q$ profile for a time frame of 200 years. The results show that the two interpolation schemes yield similar peak value and arrival time for both the mean and the standard deviation of the mass flux. The differences that exist between the two interpolation schemes are very minor, indicating that any of the two schemes would lead to the same exact final result (after applying matrix diffusion and decays computations).

Standard random walk methods (represented by Equation 3.7) usually rely on the assumption that medium properties such as porosity, θ, and dispersion coefficient, D, are sufficiently smooth. Discontinuities in effective subsurface transport properties that may arise in discrete velocity fields of numerical groundwater flow models violate this smoothness assumption (LaBolle et al., 2000). Therefore, when either θ or D are discontinuous (e.g., step functions, as is the case between the cavity and the surrounding domain), these standard methods fail (LaBolle et al., 1996) because the gradient terms of D and/or θ cannot be formally defined. LaBolle et al. (2000) developed generalized stochastic differential equations applicable to the case of discontinuous coefficients (e.g., dispersion coefficients) and developed a new random walk method that numerically integrates these equations. That method is applicable for cases of abrupt changes in transport parameters and velocity values. The new random-walk equations proposed by LaBolle et al. (2000) can be written as

$$X_{t+\Delta t} = X_t + V_x(X_t, t)\Delta t + (2D(V(X_t + \delta, t))\Delta t)^{1/2} \cdot Z \qquad (6.1)$$

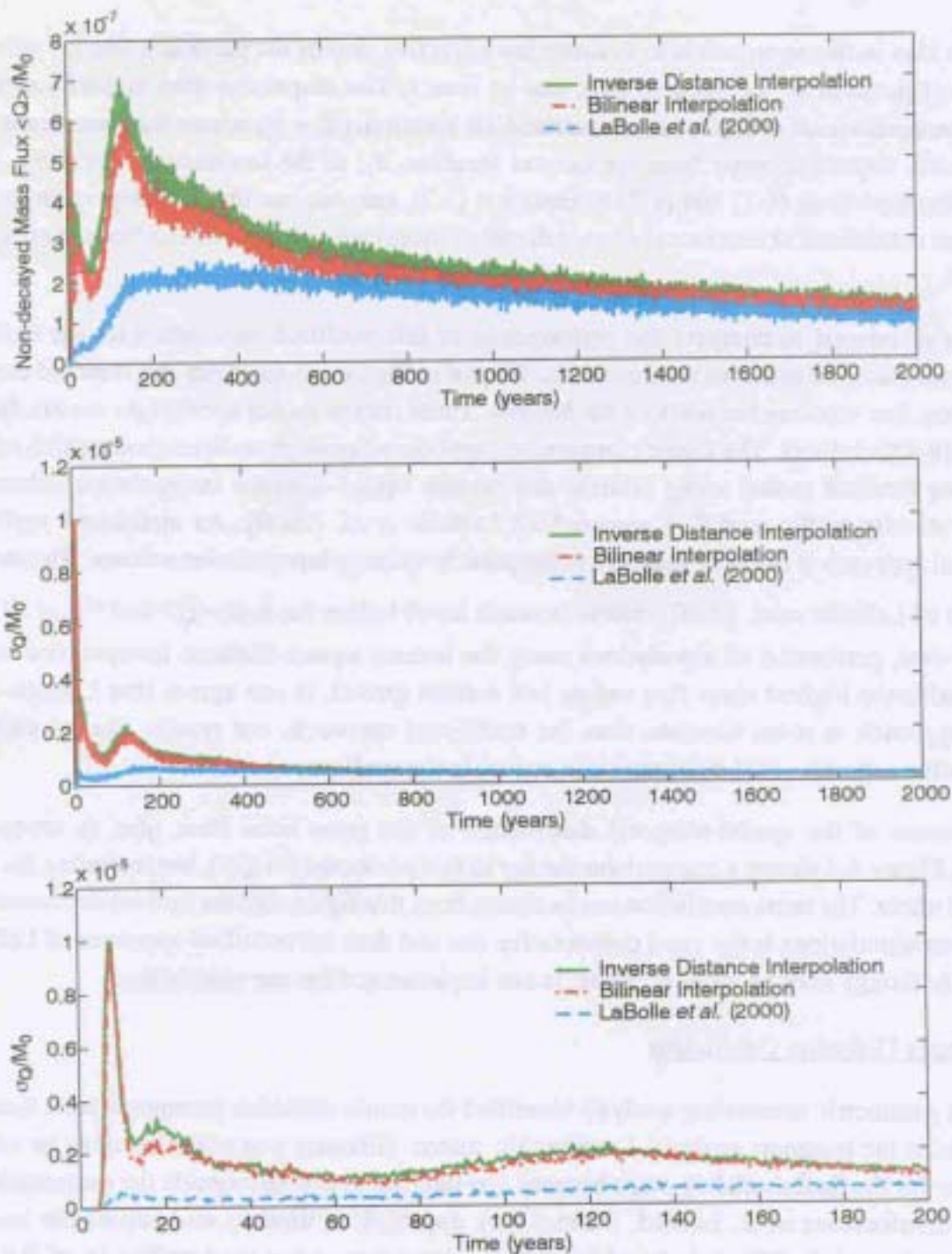where the displacement vector δ is defined as

174

Figure 6.3. Comparison between bilinear and inverse-distance interpolation schemes and between these two traditional random walk techniques and the modified method of LaBolle *et al.* (2000) that avoids computing dispersion and porosity gradient terms.

$$\delta = (2D(V(X_t,t))\Delta t)^{1/2} \cdot Z \tag{6.2}$$

The idea in this approach is to evaluate the advective step of the particle using the velocity at the current position of the particle (X_t), and at time t. The dispersive step is performed using dispersion coefficients evaluated at an intermediate location, ($X_t + \delta$), where the increments vector δ represents dispersive steps from the current location, X_t, to the intermediate location, $X_t + \delta$. Comparing Equations (6.1) and (6.2) to Equation (3.7), one can see that the dispersion gradients (which are not defined at interfaces between domain blocks) are not needed in LaBolle *et al.*'s (2000) approach.

It is of interest to compare the performance of this modified approach with the traditional random walk method in one of the three tests. We plot in Figure 6.3 the mean and standard deviation of the mass flux crossing the seafloor for Milrow. These results do not account for matrix diffusion or for radioactive decay. The figure compares the traditional random walk method (which relies on computing gradient terms) using bilinear and inverse square-distance interpolation schemes for particle velocity to the modified approach of LaBolle *et al.* (2000). As mentioned earlier, the traditional approach is not very sensitive to the particle velocity interpolation scheme. The modified approach of LaBolle *et al.* (2000) results in much lower values for both $<Q>$ and $^\sigma Q$ at all times. We, however, performed all simulations using the inverse square-distance interpolation scheme, which yields the highest mass flux values and earliest arrival. If one agrees that LaBolle *et al.*'s (2000) approach is more accurate than the traditional approach, our results can be viewed as conservative estimates of the radionuclide arrival to the seafloor.

In terms of the spatial-temporal distribution of the point mass flux, $q(x_i, t)$, crossing the seafloor, Figure 6.4 shows a comparison similar to that presented for $Q(t)$, but including the matrix diffusion effect. The same conclusion can be drawn from this figure that the inverse distance scheme used in our simulations is the most conservative one and thus the modified approach of LaBolle *et al.* (2000), though may be more accurate, is not implemented for our simulations.

6.1.2 Matrix Diffusion Coefficient

The parametric uncertainty analysis identified the matrix diffusion parameter, κ, as a sensitive parameter in the transport analysis. Despite this, matrix diffusion was not selected as an uncertain parameter for the final modeling stage because few data are available to guide the generation of the random distributions of κ. Instead, a sensitivity approach is used to understand the impact of uncertainty in matrix diffusion. In addition to the base-case value used earlier (κ of 0.434), an order-of-magnitude lower κ is evaluated here to assess the sensitivity of the transport results to the uncertainty associated with this parameter. Recall that the value of 0.434 itself already allows less diffusion than the best estimate of κ of 1.37 $day^{-1/2}$. This particular sensitivity analysis is performed using all of the flow realizations generated for the three sites and includes parameter uncertainty as used in the base-case models presented in Section 5, with the only difference being the lower κ of 0.0434 $day^{-1/2}$.
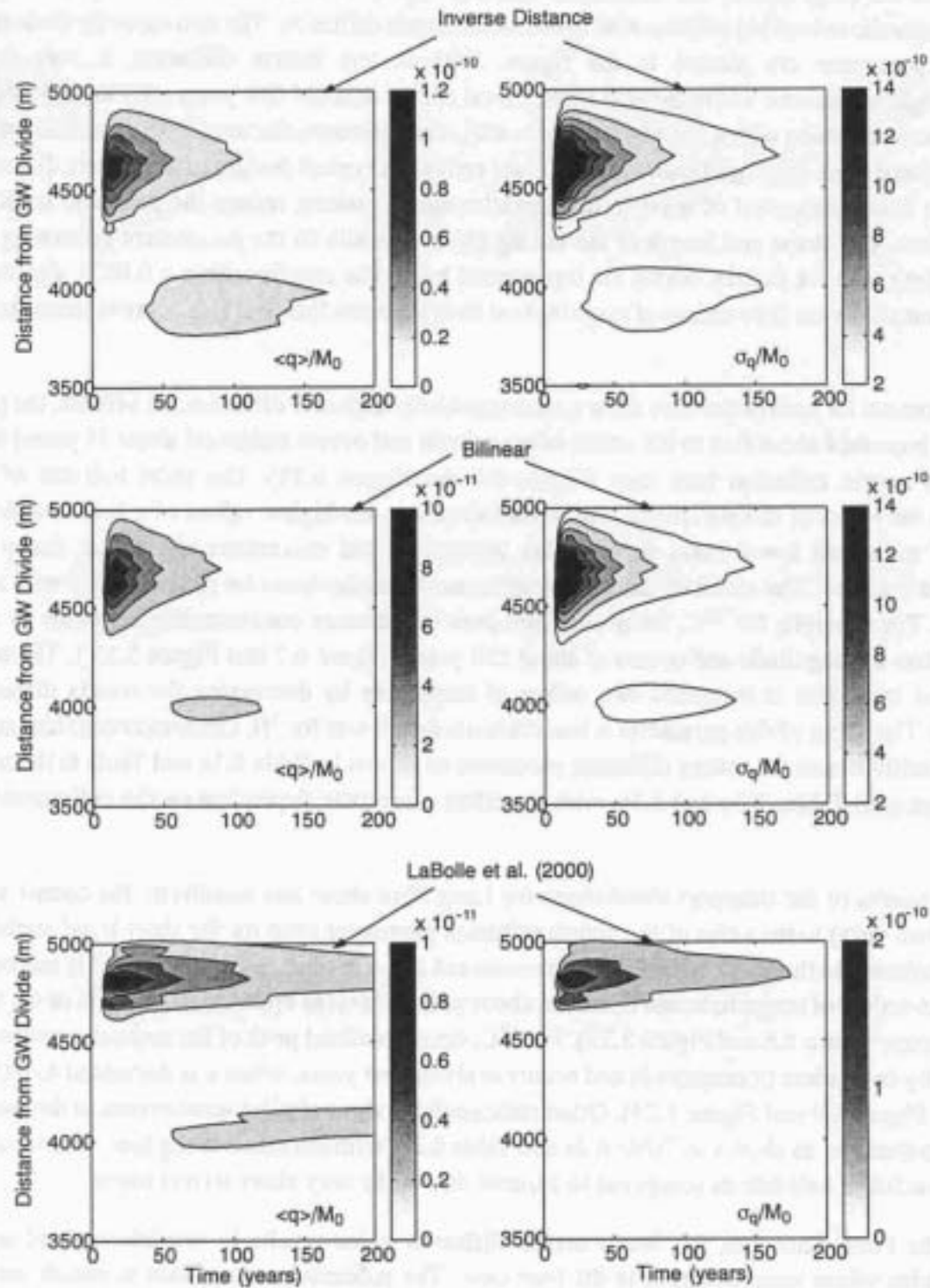
Figure 6.4. Comparison between bilinear and inverse-distance interpolation schemes and between these two traditional random walk techniques and the modified method of LaBolle *et al.* (2000) that avoids computing dispersion and porosity gradient terms.

Figure 6.5 (top) shows the undecayed breakthrough curves for the first solute class (100 percent hydraulic release) at Milrow with and without matrix diffusion. The two cases for the matrix diffusion parameter are plotted in the figure. Without any matrix diffusion, a very early breakthrough is observed where the first mass arrival occurs at about five years after the test. When adding matrix diffusion with κ = 0.434 (the base case), a significant reduction in the mass flux values is obtained and there is a significant delay in mass arrival. A typical feature of the matrix diffusion effect is to delay the arrival of mass to the breakthrough boundary, reduce the peak and induce a tailing effect. The shape and length of the tailing effect depends on the parameters governing the diffusion into the rock matrix, which are represented by κ. The results with κ = 0.0434 also show a significant reduction (two orders of magnitude at least) in mass flux, but less delay in mass arrival time.

The results for each of the sites show a great sensitivity to matrix diffusion. At Milrow, the peak ^{3}H flux is increased about five to six orders of magnitude and occurs earlier (at about 15 years) than the higher matrix diffusion base case (Figure 6.6 and Figure 5.14). The short half-life of ^{3}H magnifies the effect of this parameter. As alluded to earlier, the higher values of κ lead to delayed arrival of mass and lower mass fluxes. This delayed arrival encounters significant decay for short-lived nuclides. The effect of this parameter is much less dramatic for radionuclides with long half-lives. For example, for ^{14}C, the normalized peak of the mean concentration increases by one to two orders of magnitude and occurs at about 250 years (Figure 6.7 and Figure 5.15). The peak of the total mass flux is increased two orders of magnitude by decreasing the matrix diffusion parameter. The effect of this parameter is less dramatic than it was for ^{3}H. Other radionuclides show similar sensitivities to the matrix diffusion parameter as shown in Table 6.1a and Table 6.1b and in comparison with Tables 5.3a and 5.3b, with the effect essentially dependent on the radionuclide's half-life.

The results of the transport simulations for Long Shot show less sensitivity (as compared to the other two tests) to the value of the matrix diffusion parameter even for the short-lived nuclides. This is attributed to the short arrival times encountered at Long Shot. The peak for ^{3}H is increased about three orders of magnitude and occurs at about seven years (as opposed to 30 years in the base case; compare Figure 6.8 and Figure 5.23). For ^{14}C, the normalized peak of the mean concentration increases by two orders of magnitude and occurs at about four years, when κ is decreased to 0.0434 (compare Figure 6.9 and Figure 5.24). Other radionuclides show similar sensitivities to the matrix diffusion parameter as shown in Table 6.2a and Table 6.2b, with the effect being less dependent on the radionuclide's half-life as compared to Milrow due to the very short arrival times.

At the Long Shot site, the lower matrix diffusion value results in breakthrough of some radionuclides where none occurred in the base case. The radionuclides in Class 6, which did not survive the base-case transport scenarios for any of the sites, showed detectable amounts of mass flux and concentration for the Long Shot case with the smaller matrix diffusion. With the short arrival times and the smaller value of the matrix diffusion parameter, the elements in that category break through but with much lower concentrations and mass fluxes as compared to elements in the first five classes. Since Class 6 survived the scenario with the small matrix diffusion (κ =
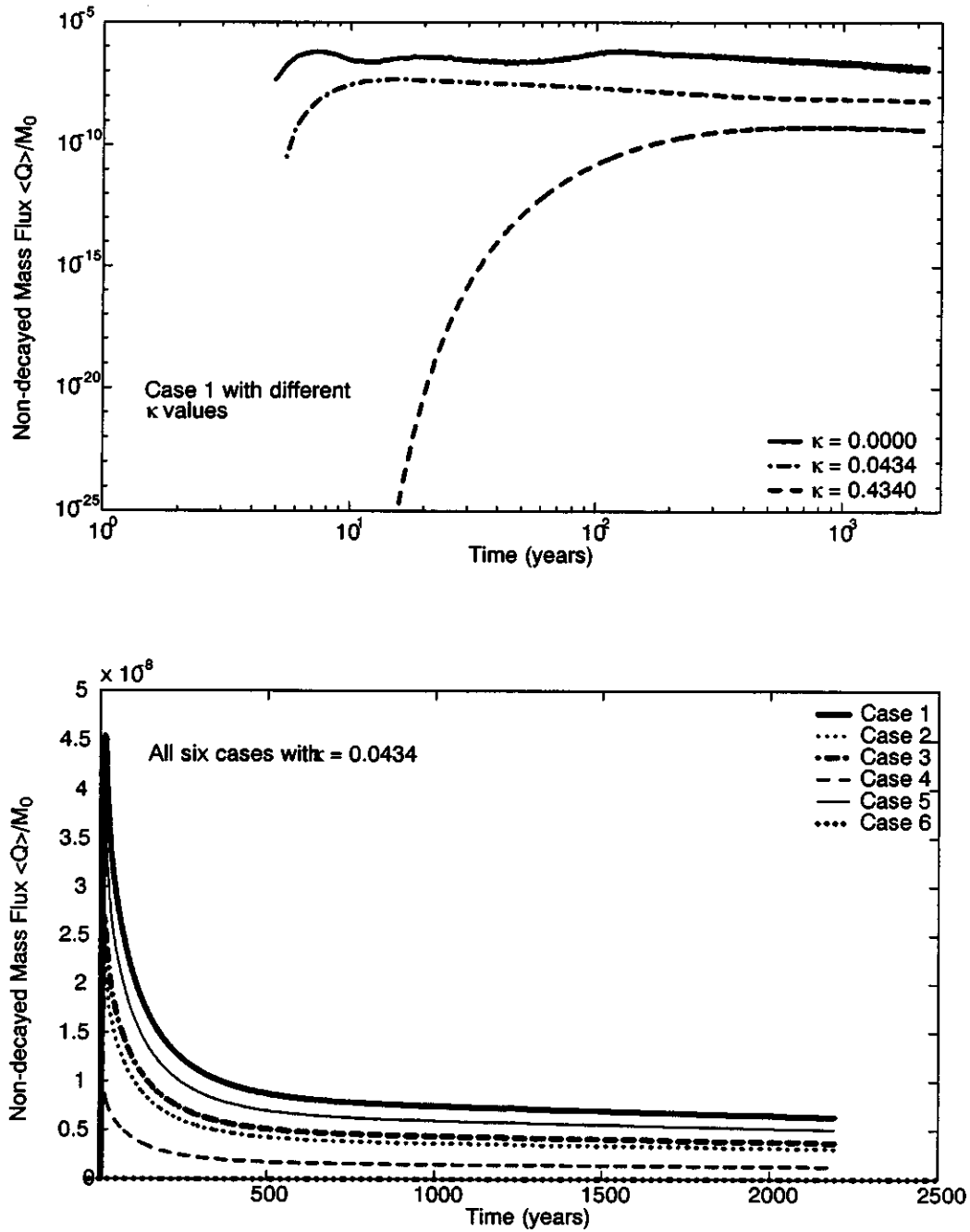
Figure 6.5. Undecayed breakthrough curves for the first solute class with different matrix diffusion strengths (top) and for the six solute classes with κ = 0.0434 (bottom).
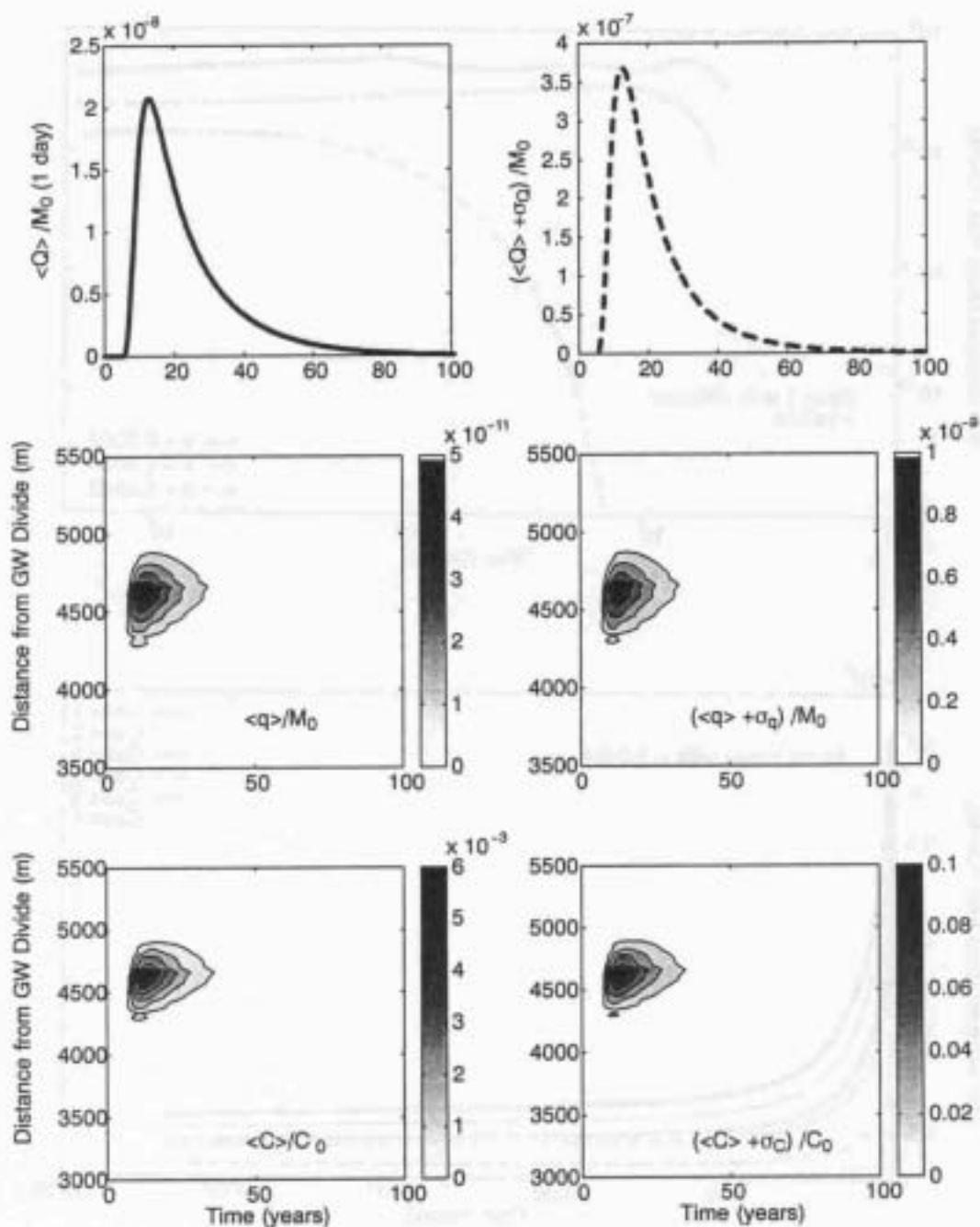
Figure 6.6.   Statistics of mass flux and concentration for ^{3}H with $\kappa = 0.0434$ at Milrow.
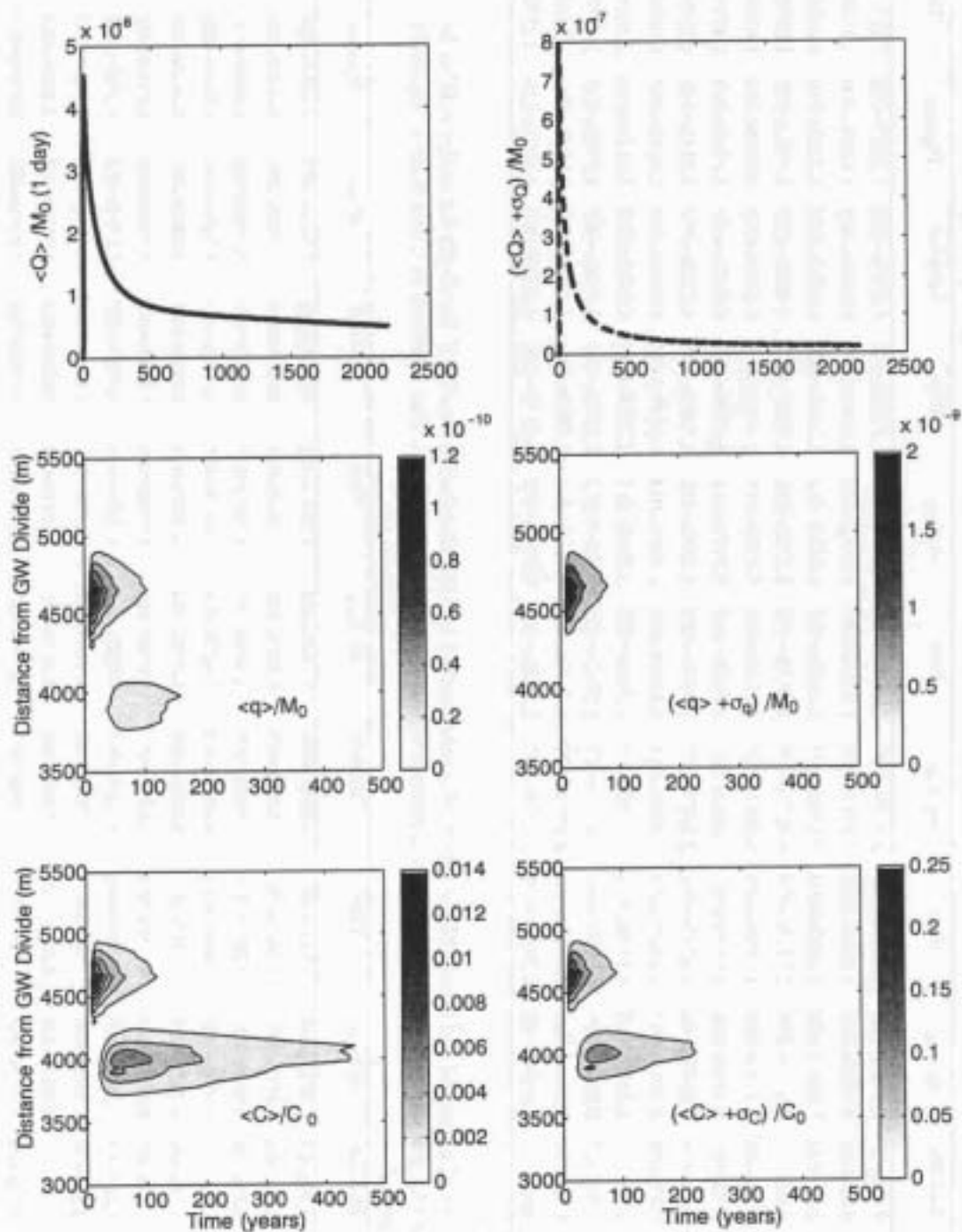
Figure 6.7. Statistics of mass flux and concentration for ^{14}C with $\kappa = 0.0434$ at Milrow.

Table 6.1a. Peaks of expected and standard deviation of mass flux and the associated times and locations for radionuclides in the Milrow source term for the matrix diffusion sensitivity case of $\kappa=0.0434$. The elements in Class 6 are completely decayed.

Case	Radio-nuclide	Half-life	$\langle Q\rangle_{max}$	Time	$(\sigma_Q)_{max}$	Time	$\langle q\rangle_{max}$	Time	Location	Time	$(\sigma_q)_{max}$	Time	Location
1	^{3}H	4.49e+03	2.0708e-008	1.3151e+001	3.4778e-007	1.2603e+001	5.6285e-011	1.3151e+001	4.6600e+003	1.3151e+001	9.7327e-010	1.3151e+001	4.6600e+003
	^{14}C	2.09e+06	4.5348e-008	1.5342e+001	7.4917e-007	1.4795e+001	1.2312e-010	1.5342e+001	4.6600e+003	1.5342e+001	2.1289e-009	1.5342e+001	4.6600e+003
	^{85}Kr	3.91e+03	1.8637e-008	1.2603e+001	3.1300e-007	1.2603e+001	5.0462e-011	1.2603e+001	4.6600e+003	1.2603e+001	8.7257e-010	1.2603e+001	4.6600e+003
	^{85}Rb	stable	3.1055e-008	2.1918e+001	4.9171e-007	1.8630e+001	8.1260e-011	1.8630e+001	4.6600e+003	1.8630e+001	1.4051e-009	1.8630e+001	4.6600e+003
2	^{36}Cl	1.10e+08	2.2195e-008	1.5890e+001	3.6651e-007	1.5342e+001	5.3925e-011	1.5342e+001	4.6200e+003	1.4795e+001	9.3246e-010	1.4795e+001	4.6200e+003
	^{129}I	5.73e+09	2.2196e-008	1.5890e+001	3.6652e-007	1.5342e+001	5.3927e-011	1.5342e+001	4.6200e+003	1.4795e+001	9.3249e-010	1.4795e+001	4.6200e+003
3	^{90}Sr	1.06e+04	1.8993e-008	1.4247e+001	3.1675e-007	1.3699e+001	4.6348e-011	1.3699e+001	4.6200e+003	1.3699e+001	8.0143e-010	1.3699e+001	4.6200e+003
	^{90}Y	2.67e+00	4.7854e-012	1.4247e+001	7.9804e-011	1.3699e+001	1.1677e-014	1.3699e+001	4.6200e+003	1.3699e+001	2.0192e-013	1.3699e+001	4.6200e+003
	^{90}Zr	stable	1.2129e-008	6.1370e+001	1.5440e-007	2.2466e+001	2.2048e-011	2.3014e+001	4.6600e+003	2.3014e+001	3.8124e-010	2.3014e+001	4.6600e+003
4	^{99m}Tc	7.78e+07	8.8346e-009	1.5890e+001	1.4577e-007	1.5342e+001	2.5324e-011	1.4247e+001	4.6200e+003	1.4247e+001	4.3790e-010	1.4247e+001	4.6200e+003
5	^{137}Cs	1.10e+04	2.5847e-008	1.4247e+001	4.2943e-007	1.4247e+001	6.4015e-011	1.3699e+001	4.5800e+003	1.3699e+001	1.1069e-009	1.3699e+001	4.5800e+003
	^{137}Ba	stable	1.6260e-008	6.2466e+001	2.0338e-007	2.2466e+001	2.9495e-011	2.1370e+001	4.5800e+003	2.1370e+001	5.1001e-010	2.1370e+001	4.5800e+003

Table 6.1b. Peaks of expected and standard deviation of concentration and the associated times and locations for radionuclides in the Milrow source term for the matrix diffusion sensitivity case of $\kappa=0.0434$. The elements in Class 6 are completely decayed.

| Case	Radio-nuclide	Half-life	$\langle C\rangle_{max}$	Time	Location	$(\sigma_C)_{max}$	Time	Location	σ_{Time}	$\sigma_{Location}$
1	^{3}H	4.49e+03	6.5022e-003	1.3151e+001	4.6600e+003	1.1243e-001	1.3151e+001	4.6600e+003	3.7456e+002	6.0644e+002
	^{14}C	2.09e+06	1.4223e-002	1.5342e+001	4.6600e+003	2.4593e-001	1.5342e+001	4.6600e+003	3.7456e+002	6.0644e+002
	^{85}Kr	3.91e+03	5.8294e-003	1.2603e+001	4.6600e+003	1.0080e-001	1.2603e+001	4.6600e+003	3.7456e+002	6.0644e+002
	^{85}Rb	stable	9.3873e-003	1.8630e+001	4.6600e+003	1.6232e-001	1.8630e+001	4.6600e+003	3.7456e+002	6.0644e+002
2	^{36}Cl	1.10e+08	6.2295e-003	1.4795e+001	4.6200e+003	1.0772e-001	1.4795e+001	4.6200e+003	3.8422e+002	6.0644e+002
	^{129}I	5.73e+09	6.2297e-003	1.4795e+001	4.6200e+003	1.0772e-001	1.4795e+001	4.6200e+003	3.8422e+002	6.0644e+002
3	^{90}Sr	1.06e+04	5.3542e-003	1.3699e+001	4.6200e+003	9.2582e-002	1.3699e+001	4.6200e+003	3.8794e+002	6.1059e+002
	^{90}Y	2.67e+00	1.3490e-006	1.3699e+001	4.6200e+003	2.3326e-005	1.3699e+001	4.6200e+003	3.8794e+002	6.1059e+002
	^{90}Zr	stable	3.5467e-003	8.1644e+001	3.9800e+003	5.1870e-002	7.2877e+001	3.9800e+003	3.8794e+002	6.1059e+002
4	^{99m}Tc	7.78e+07	2.9255e-003	1.4247e+001	4.6200e+003	5.0586e-002	1.4247e+001	4.6200e+003	4.0143e+002	6.0781e+002
5	^{137}Cs	1.10e+04	7.3429e-003	1.3699e+001	4.6200e+003	1.2697e-001	1.3699e+001	4.6200e+003	3.8413e+002	6.0905e+002
	^{137}Ba	stable	4.6785e-003	7.8356e+001	4.0200e+003	7.1420e-002	7.1233e+001	4.0200e+003	3.8413e+002	6.0905e+002
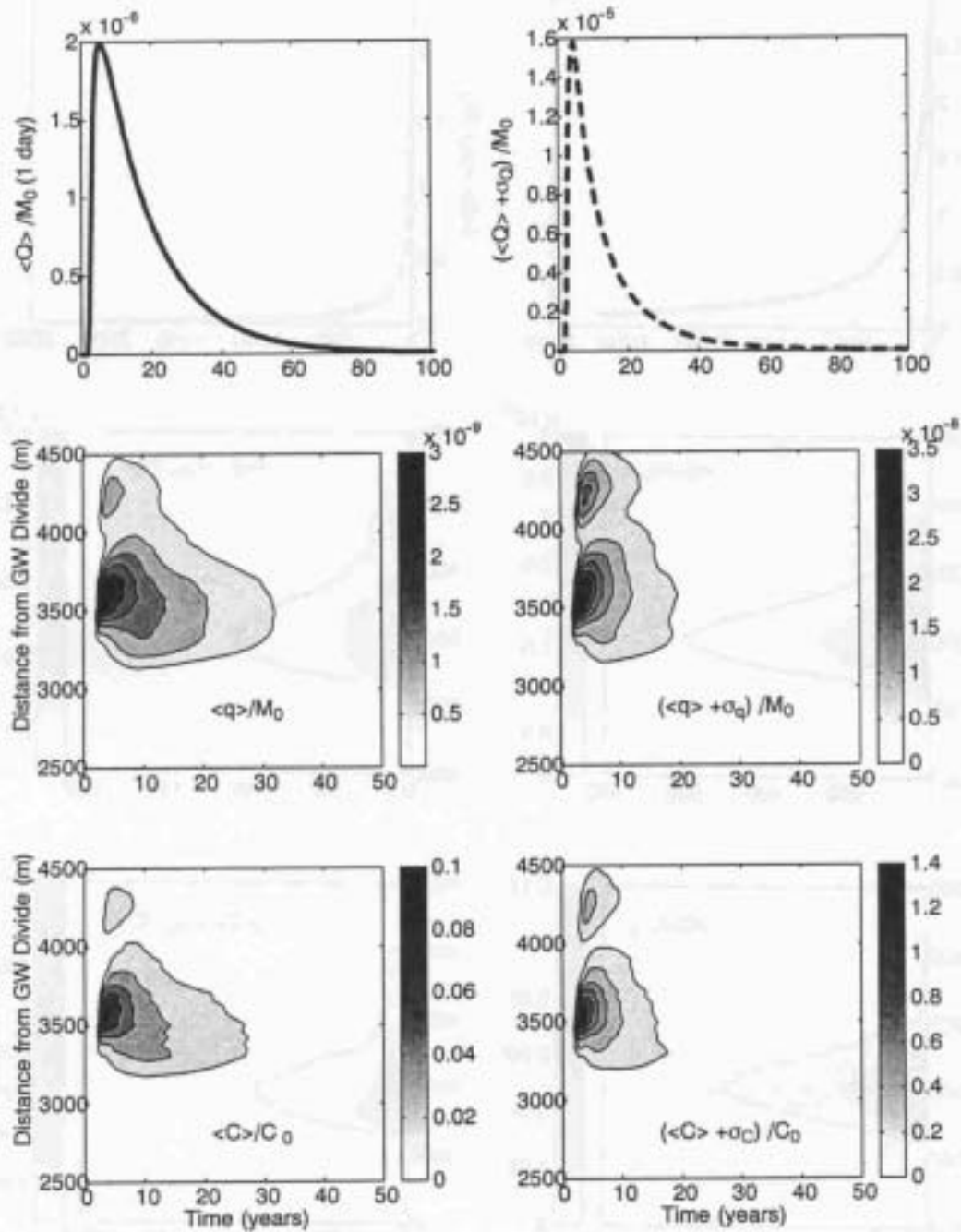
Figure 6.8. Statistics of mass flux and concentration for ^3H with $\kappa = 0.0434$ at Long Shot.
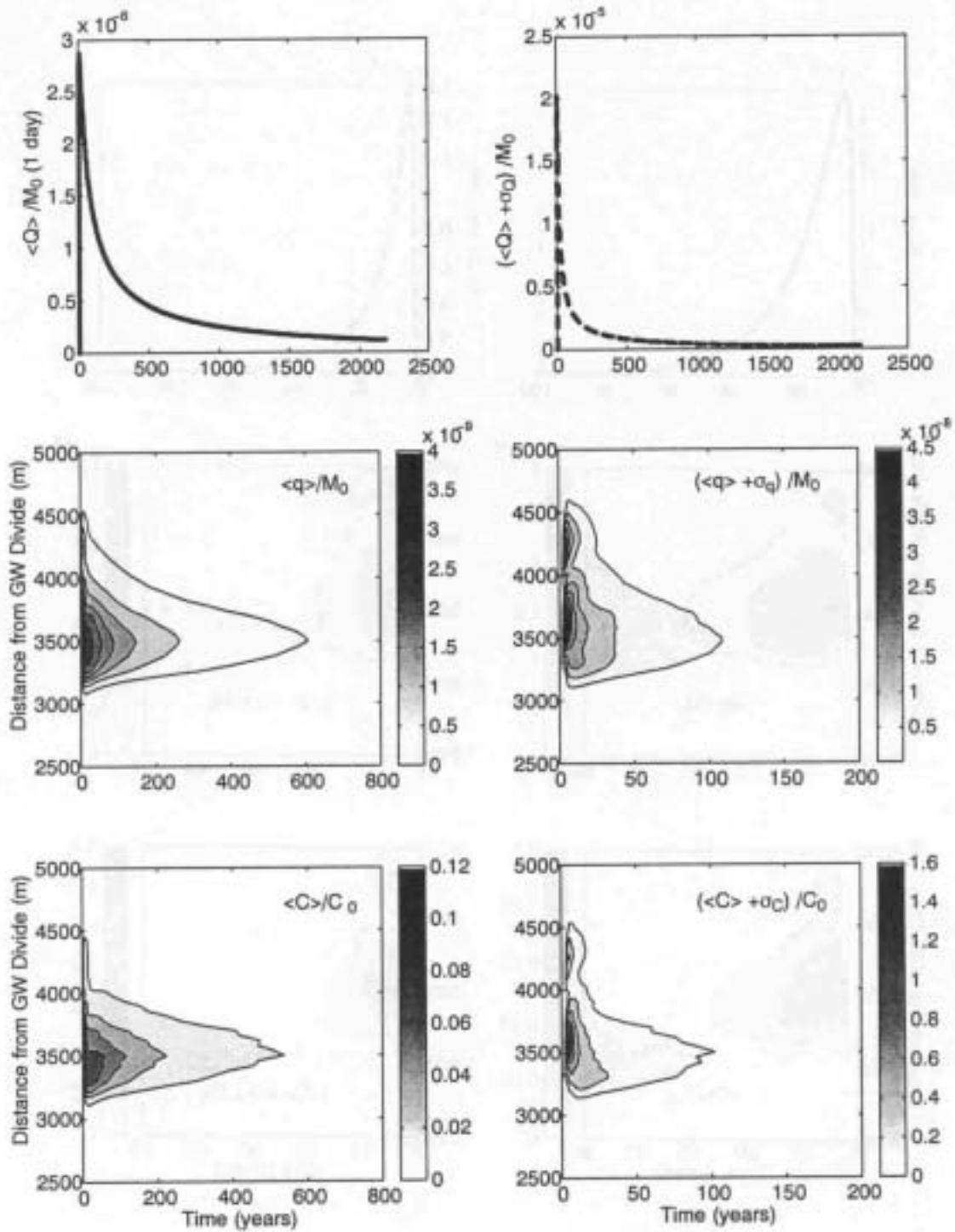
Figure 6.9. Statistics of mass flux and concentration for ^{14}C with $\kappa = 0.0434$ at Long Shot.

Table 6.2a. Peaks of expected and standard deviation of mass flux and the associated times and locations for radionuclides in the Long Shot source term for the matrix diffusion sensitivity case of κ=0.0434.

Case	Radionuclide	Half-life	$\langle Q \rangle_{max}$	Time	$(\sigma_Q)_{max}$	Time	$\langle q \rangle_{max}$	Time	Location	$(\sigma_q)_{max}$	Time	Location
1	^{3}H	4.49e+03	1.9907e-006	5.4795e+000	1.3867e-005	4.3836e+000	3.4989e-009	3.8356e+000	3.5800e+003	3.4803e-008	3.2877e+000	3.5400e+003
	^{14}C	2.09e+06	2.8710e-006	8.7671e+000	1.7743e-005	4.3836e+000	4.3411e-009	3.8356e+000	3.5800e+003	4.2802e-008	3.8356e+000	3.5800e+003
	^{85}Kr	3.91e+03	1.9057e-006	4.9315e+000	1.3369e-005	4.3836e+000	3.3885e-009	3.8356e+000	3.5800e+003	3.3860e-008	3.2877e+000	3.5400e+003
	^{85}Rb	stable	2.0015e-006	3.1233e+001	5.4926e-006	1.0959e+001	2.6448e-009	3.3973e+001	3.5000e+003	1.0244e-008	4.9315e+000	3.6200e+003
2	^{36}Cl	1.10e+08	1.4316e-006	8.7671e+000	8.8275e-006	4.3836e+000	2.1534e-009	4.3836e+000	3.6600e+003	2.1044e-008	3.8356e+000	3.5800e+003
	^{129}I	5.73e+09	1.4316e-006	8.7671e+000	8.8275e-006	4.3836e+000	2.1535e-009	4.3836e+000	3.6600e+003	2.1044e-008	3.8356e+000	3.5800e+003
3	^{90}Sr	1.06e+04	2.3994e-006	6.5753e+000	1.6000e-005	4.3836e+000	3.9651e-009	3.8356e+000	3.5800e+003	3.9076e-008	3.8356e+000	3.5800e+003
	^{90}Y	2.67e+00	6.0453e-010	6.5753e+000	4.0313e-009	4.3836e+000	9.9900e-013	3.8356e+000	3.5800e+003	9.8451e-012	3.8356e+000	3.5800e+003
	^{90}Zr	stable	1.3455e-006	5.6986e+001	2.5908e-006	1.7534e+001	1.8528e-009	6.1918e+001	3.5000e+003	4.5222e-009	2.5753e+001	3.5800e+003
4	^{99}Tc	7.78e+07	5.7862e-007	8.7671e+000	3.5777e-006	4.3836e+000	9.0926e-010	3.8356e+000	3.5800e+003	8.9610e-009	3.8356e+000	3.5800e+003
5	^{137}Cs	1.10e+04	1.9463e-006	6.0274e+000	1.2946e-005	4.3836e+000	3.2331e-009	3.8356e+000	3.6200e+003	3.1716e-008	3.8356e+000	3.5800e+003
	^{137}Ba	stable	1.0610e-006	5.8630e+001	2.0156e-006	1.8082e+001	1.4601e-009	6.4658e+001	3.5000e+003	3.5121e-009	2.7945e+001	3.6200e+003
6	^{151}Sm	3.29e+04	1.2841e-018	8.9425e+002	1.9841e-017	8.9425e+002	1.2826e-020	8.9315e+002	3.3800e+003	0.0000e+000	0.0000e+000	2.0000e+001
	^{151}Eu	stable	7.8188e-013	4.3836e+003	8.5068e-012	4.3836e+003	2.7120e-015	4.3836e+003	3.5000e+003	0.0000e+000	0.0000e+000	2.0000e+001
	^{152}Eu	4.93e+03	0.0000e+000	NA	0.0000e+000	NA	0.0000e+000	0.0000e+000	0.0000e+000	0.0000e+000	NA	NA
	^{152}Gd	stable	7.8188e-013	4.3836e+003	8.5068e-012	4.3836e+003	2.7120e-015	4.3836e+003	3.5000e+003	0.0000e+000	0.0000e+000	2.0000e+001
	^{234}U	8.99e-07	7.7229e-013	4.3836e+003	8.4025e-012	4.3836e+003	2.6787e-015	4.3836e+003	3.5000e+003	0.0000e+000	0.0000e+000	2.0000e+001
	^{238}U	1.64e+12	7.8188e-013	4.3836e+003	8.5068e-012	4.3836e+003	2.7120e-015	4.3836e+003	3.5000e+003	0.0000e+000	0.0000e+000	2.0000e+001
	^{237}Np	7.82e+08	7.8077e-013	4.3836e+003	8.4947e-012	4.3836e+003	2.7081e-015	4.3836e+003	3.5000e+003	0.0000e+000	0.0000e+000	2.0000e+001
	^{239}Pu	8.77e+06	6.8900e-013	4.3836e+003	7.4963e-012	4.3836e+003	2.3898e-015	4.3836e+003	3.5000e+003	0.0000e+000	0.0000e+000	2.0000e+001
	^{240}Pu	2.40e+06	4.9255e-013	4.3836e+003	5.3589e-012	4.3836e+003	1.7084e-015	4.3836e+003	3.5000e+003	0.0000e+000	0.0000e+000	2.0000e+001
	^{236}U	8.40e09	2.8931e-013	4.3836e+003	3.1476e-012	4.3836e+003	1.0035e-015	4.3836e+003	3.5000e+003	0.0000e+000	0.0000e+000	2.0000e+001
	^{241}Am	1.58e+05	2.5203e-015	2.3419e+003	3.3496e-014	2.1512e+003	1.8115e-017	1.8422e+003	3.3800e+003	0.0000e+000	0.0000e+000	2.0000e+001
	^{237}Np#2	7.82e_08	7.8116e-013	4.3836e+003	8.4989e-012	4.3836e+003	2.7095e-015	4.3836e+003	3.5000e+003	0.0000e+000	0.0000e+000	2.0000e+001

185

Table 6.2b. Peaks of expected and standard deviation of concentration and the associated times and locations for radionuclides in the Long Shot source term for the matrix diffusion sensitivity case of κ=0.0434.

Case	Radionu-clide	Half-life	$\langle C \rangle_{max}$	Time	Location	$(\sigma_C)_{max}$	Time	Location	σ_{Time}	$\sigma_{Location}$
1	^{3}H	4.49e+03	1.0370e-001	3.8356e+000	3.5800e+003	1.3045e+000	3.2877e+000	3.5000e+003	5.1946e+002	3.3752e+002
	^{14}C	2.09e+06	1.2866e-001	3.8356e+000	3.5800e+003	1.5694e+000	3.2877e+000	3.5000e+003	5.1946e+002	3.3752e+002
	^{85}Kr	3.91e+03	1.0076e-001	3.2877e+000	3.5400e+003	1.2692e+000	3.2877e+000	3.5000e+003	5.1946e+002	3.3752e+002
	^{85}Rb	stable	8.2466e-002	4.0000e+001	3.4200e+003	3.3648e-001	4.9315e+000	3.5800e+003	5.1946e+002	3.3752e+002
2	^{36}Cl	1.10e+08	6.3302e-002	3.8356e+000	3.6200e+003	7.5662e-001	3.2877e+000	3.5400e+003	5.1963e+002	3.3820e+002
	^{129}I	5.73e+09	6.3303e-002	3.8356e+000	3.6200e+003	7.5663e-001	3.2877e+000	3.5400e+003	5.1963e+002	3.3820e+002
3	^{90}Sr	1.06e+04	1.1749e-001	3.8356e+000	3.5800e+003	1.4515e+000	3.2877e+000	3.5000e+003	5.1946e+002	3.3740e+002
	^{90}Y	2.67e+00	2.9601e-005	3.8356e+000	3.5800e+003	3.6572e-004	3.2877e+000	3.5000e+003	5.1946e+002	3.3740e+002
	^{90}Zr	stable	6.2070e-002	7.1781e+001	3.5000e+003	1.6611e-001	2.7397e+001	3.3000e+003	5.1946e+002	3.3740e+002
4	^{99}Tc	7.78e+07	2.7239e-002	4.3836e+000	3.6200e+003	3.1002e-001	3.2877e+000	3.5400e+003	5.1950e+002	3.3854e+002
5	^{137}Cs	1.10e+04	9.7587e-002	3.8356e+000	3.6200e+003	1.1162e+000	3.2877e+000	3.5400e+003	5.1984e+002	3.3761e+002
	^{137}Ba	stable	4.9305e-002	7.3973e+001	3.5000e+003	1.2845e-001	2.9041e+001	3.3000e+003	5.1984e+002	3.3761e+002
6	^{151}Sm	3.29e+04	4.6052e-013	8.9315e+002	3.3800e+003	7.1193e-012	8.9315e+002	3.3800e+003	2.2290e+002	2.8897e+002
	^{151}Eu	stable	9.8812e-008	4.3836e+003	3.5000e+003	1.3924e-006	4.3836e+003	3.5000e+003	2.2290e+002	2.8897e+002
	^{152}Eu	4.93e+03	0.0000e+000	NA	NA	0.0000e+000	NA	NA	NA	NA
	^{152}Gd	stable	9.8812e-008	4.3836e+003	3.5000e+003	1.3924e-006	4.3836e+003	3.5000e+003	2.2290e+002	2.8897e+002
	^{234}U	8.99e-07	9.7600e-008	4.3836e+003	3.5000e+003	1.3753e-006	4.3836e+003	3.5000e+003	2.2290e+002	2.8897e+002
	^{238}U	1.64e+12	9.8812e-008	4.3836e+003	3.5000e+003	1.3924e-006	4.3836e+003	3.5000e+003	2.2290e+002	2.8897e+002
	^{237}Np	7.82e+08	9.8672e-008	4.3836e+003	3.5000e+003	1.3904e-006	4.3836e+003	3.5000e+003	2.2290e+002	2.8897e+002
	^{239}Pu	8.77e+06	8.7074e-008	4.3836e+003	3.5000e+003	1.2270e-006	4.3836e+003	3.5000e+003	2.2290e+002	2.8897e+002
	^{240}Pu	2.40e+06	6.2247e-008	4.3836e+003	3.5000e+003	8.7716e-007	4.3836e+003	3.5000e+003	2.2290e+002	2.8897e+002
	^{236}U	8.40e09	3.6562e-008	4.3836e+003	3.5000e+003	5.1521e-007	4.3836e+003	3.5000e+003	2.2290e+002	2.8897e+002
	^{241}Am	1.58e+05	6.4704e-010	1.8334e+003	3.3800e+003	9.9693e-009	1.8279e+003	3.3800e+003	2.2290e+002	2.8897e+002
	^{237}Np#2	7.82e-08	9.8720e-008	4.3836e+003	3.5000e+003	1.3911e-006	4.3836e+003	3.5000e+003	2.2290e+002	2.8897e+002

186

$0.0434\sqrt{9,000}$ = 4.117), Figure 6.10 presents the mass flux and concentration plots for [151]Sm with a half-life of 3,290 days. [151]Sm is a rare-earth element with a high boiling point, low solubility and high K_d for clays and zeolites, and thus has a behavior analogous to that of the actinides. The results show very small concentration and mass flux values as compared to ^{3}H and [14]C. The normalized peak of the mean plus one standard deviation of concentration is about 7.0×10^{-12} and occurs at about 900 years and 1,400 m from the divide. Table 6.2b shows some higher concentrations for other elements in Case 6 due to longer half-lives.

More similar to Milrow, the results for Cannikin show a great sensitivity to the matrix diffusion parameter. For tritium, the peak is increased about six orders of magnitude and occurs much earlier (at about 20 years) than in the base case (compare Figure 6.11 and Figure 5.33). As mentioned earlier, the short half-life of ^{3}H magnifies the effect of this parameter. For ^{14}C, the normalized peak of the mean concentration increases by two orders of magnitude and occurs at about 30 years in this sensitivity case (compare Figure 6.12 and Figure 5.34). The effect of this parameter is less dramatic than it was for [3]H. Other radionuclides show similar sensitivities to the matrix diffusion parameter as shown in Table 6.3a and Table 6.3b, with the effect being dependent on the radionulclide's half-life.

6.1.3 Colloid Transport

The most extreme sensitivity case regarding matrix diffusion is to consider no diffusion at all. Given the high porosity measured for rocks from Amchitka, this is physically reasonable only if the conceptual model is one of porous medium flow, rather than fracture flow. This scenario was evaluated during the parametric uncertainty analysis and transport times were much longer for porous medium flow with no matrix diffusion than for fracture flow with matrix diffusion. However, there is one transport mechanism within the conceptual model of fracture flow that could allow for unretarded transport, and that is transport via colloids.

Colloids are submicrometer-size suspended particles that can be mobile in groundwater and have the potential to enhance transport of non-soluble contaminants through sorption. Buddemeier and Hunt (1988) demonstrated that colloids can play a role in moving relatively insoluble radionuclides (particularly rare-earth fission products such as [151]Sm) away from underground nuclear tests. This transport process has been proposed to explain the occurrence of very low concentrations of plutonium (Pu) 1.3 km from an underground nuclear test on the NTS (Kersting *et al.*, 1999). The ability of colloids to migrate significant distances and move significant mass is questionable, particularly under the geochemical conditions of a saltwater intrusion environment. Of particular concern are the reversibility of radionuclide sorption onto colloids, attachment of colloids to fracture walls, and aggregation with resultant filtering of colloids. These processes and experiments studying them are described by Triay *et al.* (1997).

The IAEA evaluated the issue of fast plutonium transport via natural colloids as one extreme of their K_d model. They assumed that 10 percent of the plutonium did not undergo sorption, but they only applied this scenario to the 12 "CRTV" tests (tests where the cavity breached the volcanic cover and was in direct contact with highly permeable carbonates). The readily anticipated result was rapid breakthrough of plutonium into the adjacent lagoon, leading to the conclusion that if colloids
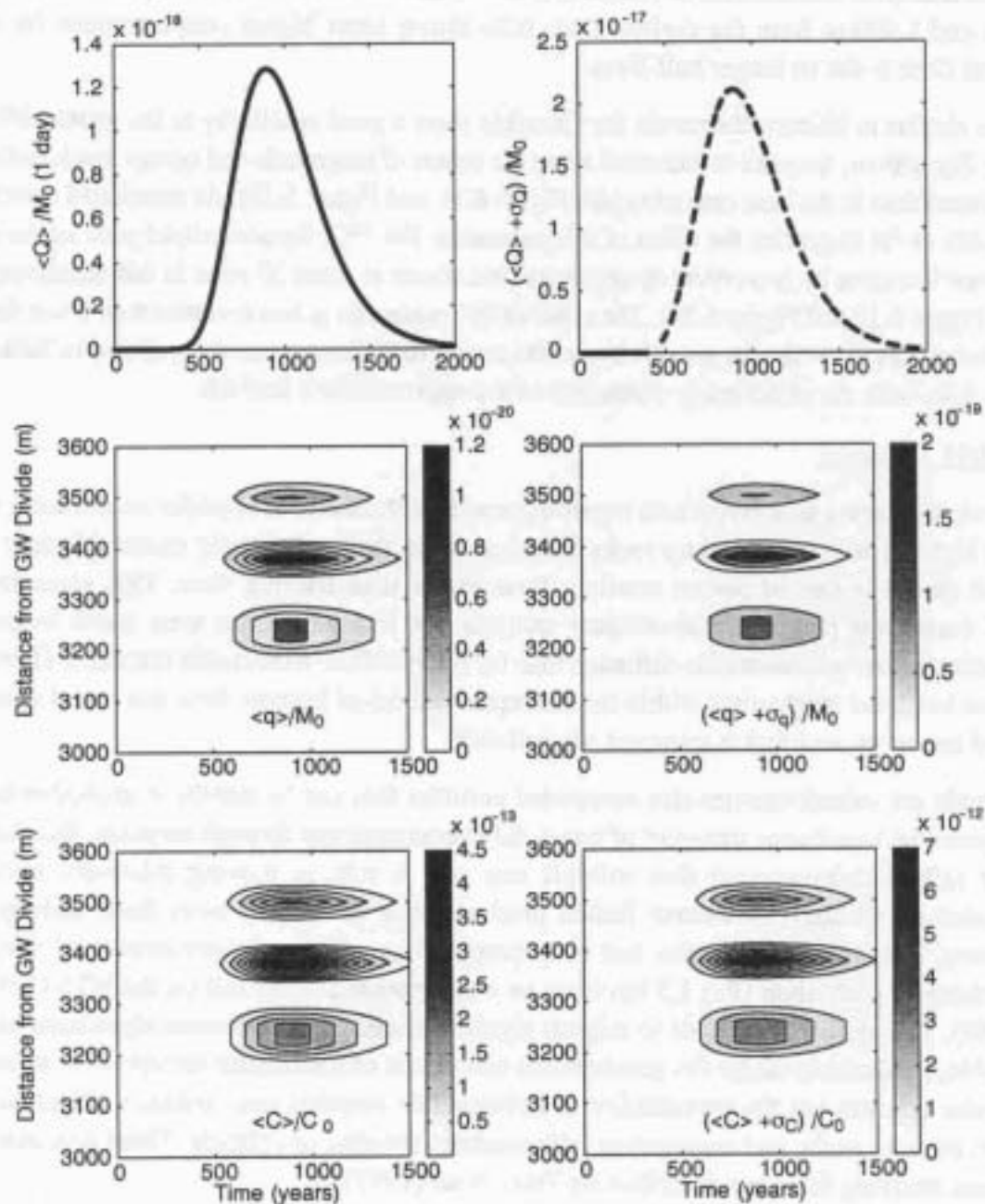
Figure 6.10. Statistics of mass flux and concentration for ^{151}Sm with $\kappa = 4.117$ at Long Shot.
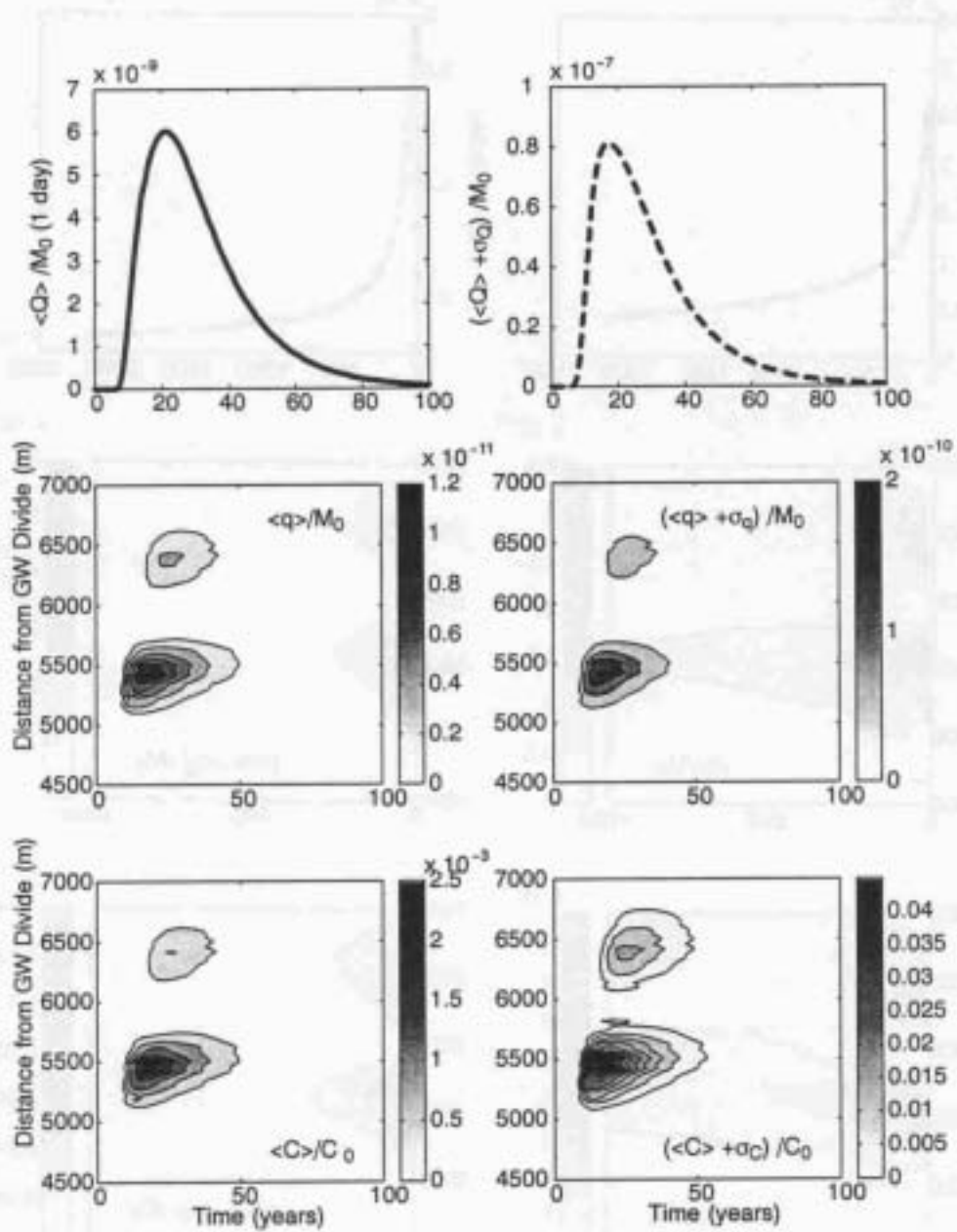
Figure 6.11. Statistics of mass flux and concentration for ^3H with $\kappa = 0.0434$ at Cannikin.
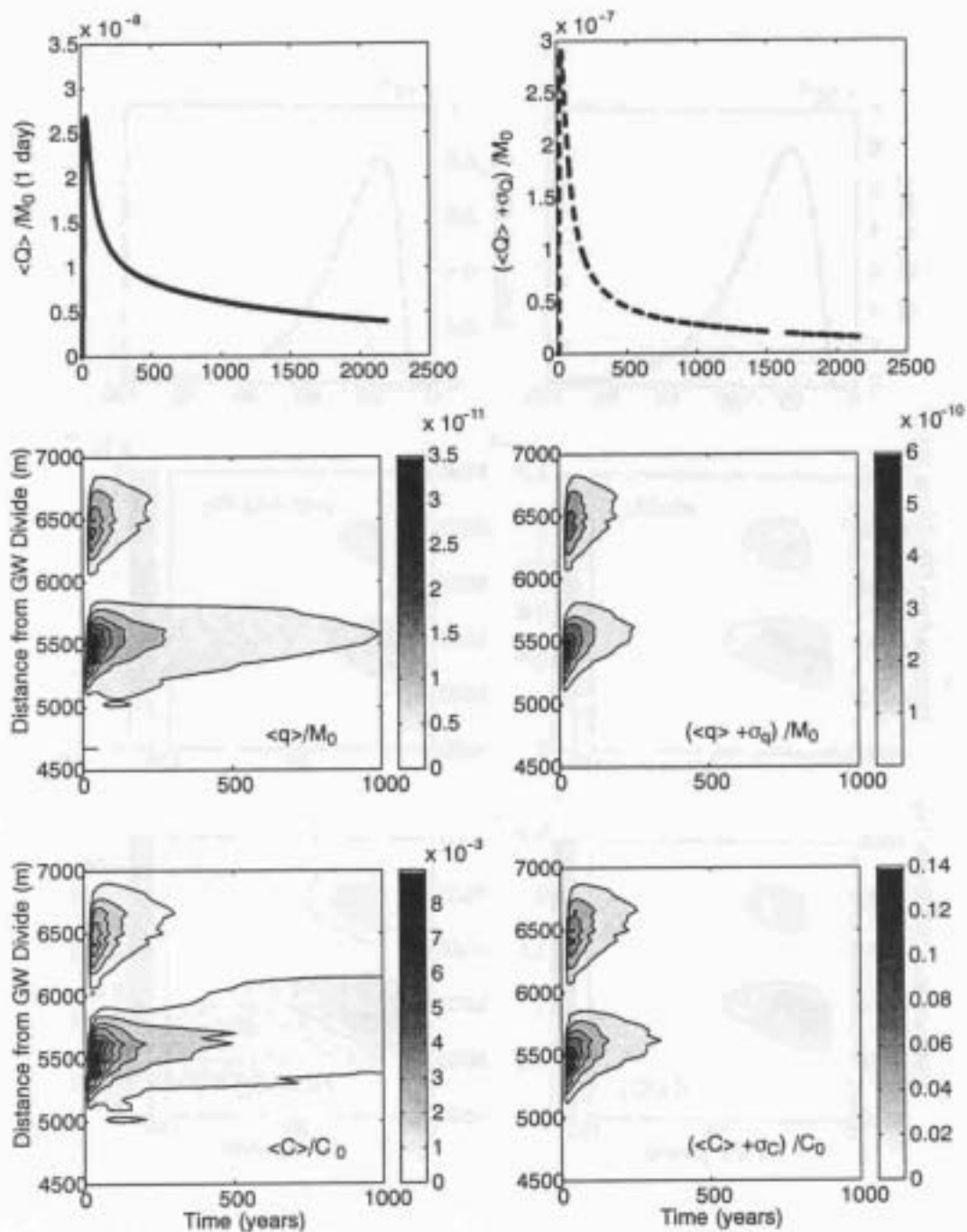
Figure 6.12. Statistics of mass flux and concentration for ^{14}C with $\kappa = 0.0434$ at Cannikin.

Table 6.3a. Peaks of expected and standard deviation of mass flux and the associated times and locations for radionuclides in the Cannikin source term for the matrix diffusion sensitivity case of $\kappa = 0.0434$. The elements in Class 6 are completely decayed.

Case	Radionuclide	Half-life	$\langle Q \rangle_{max}$	Time	$(\sigma_Q)_{max}$	Time	$\langle q \rangle_{max}$	Time	Location	$(\sigma_q)_{max}$	Time	Location
1	³H	4.49e+03	6.0165e-009	2.1370e+001	7.5566e-008	1.6986e+001	1.2878e-011	1.6986e+001	5.4200e+003	2.0654e-010	1.6986e+001	5.4200e+003
	¹⁴C	2.09e+06	2.6831e-008	3.6712e+001	2.6385e-007	3.1781e+001	3.9113e-011	2.4658e+001	5.4200e+003	5.9390e-010	2.1370e+001	5.4200e+003
	⁸⁵Kr	3.91e+03	5.0526e-009	2.0274e+001	6.5699e-008	1.6438e+001	1.1173e-011	1.6986e+001	5.4200e+003	1.7920e-010	1.6986e+001	5.4200e+003
	⁸⁵Rb	stable	2.4896e-008	4.2740e+001	2.3682e-007	3.7808e+001	3.4705e-011	3.6164e+001	5.5000e+003	4.6480e-010	2.5753e+001	5.4200e+003
2	³⁶Cl	1.10e+08	1.3161e-008	3.7260e+001	1.2930e-007	3.2329e+001	1.8997e-011	2.5205e+001	5.4200e+003	2.8172e-010	2.2466e+001	5.4200e+003
	¹²⁹I	5.73e+09	1.3162e-008	3.7260e+001	1.2931e-007	3.2329e+001	1.8998e-011	2.5205e+001	5.4200e+003	2.8174e-010	2.2466e+001	5.4200e+003
3	⁹⁰Sr	1.06e+04	7.6751e-009	2.6849e+001	8.3424e-008	2.2466e+001	1.3511e-011	1.8082e+001	5.3800e+003	2.1518e-010	1.7534e+001	5.3800e+003
	⁹⁰Y	2.67e+00	1.9338e-012	2.6849e+001	2.1019e-011	2.2466e+001	3.4040e-015	1.8082e+001	5.3800e+003	5.4216e-014	1.7534e+001	5.5000e+003
4	⁹⁰Zr	stable	1.0678e-008	5.8630e+001	9.6573e-008	5.0411e+001	1.4001e-011	5.2055e+001	5.5400e+003	1.6991e-010	4.1096e+001	5.5000e+003
	⁹⁹Tc	7.78e+07	5.4650e-009	3.7260e+001	5.3838e-008	3.1781e+001	9.0239e-012	2.5205e+001	5.4600e+003	1.3845e-010	1.9726e+001	5.3800e+003
5	¹³⁷Cs	1.10e+04	1.0715e-008	2.6849e+001	1.1639e-007	2.2466e+001	1.7956e-011	2.0822e+001	5.4600e+003	2.8198e-010	1.8082e+001	5.4200e+003
	¹³⁷Ba	stable	1.4179e-008	5.9726e+001	1.2765e-007	5.0411e+001	1.9057e-011	5.0959e+001	5.5400e+003	2.2036e-010	4.7671e+001	5.5400e+003

Table 6.3b. Peaks of expected and standard deviation of concentration and the associated times and locations for radionuclides in the Cannikin source term for the matrix diffusion sensitivity case of $\kappa = 0.0434$. The elements in Class 6 are completely decayed.

Case	Radionuclide	Half-life	$\langle C \rangle_{max}$	Time	Location	$(\sigma_C)_{max}$	Time	Location	σ_{Time}	$\sigma_{Location}$
1	³H	4.49e+03	2.8678e-003	1.6986e+001	5.4200e+003	4.5998e-002	1.6986e+001	5.4200e+003	4.1543e+002	7.3178e+002
	¹⁴C	2.09e+06	9.5445e-003	3.0137e+001	5.5000e+003	1.3471e-001	2.4110e+001	5.5000e+003	4.1543e+002	7.3178e+002
	⁸⁵Kr	3.91e+03	2.4882e-003	1.6986e+001	5.4200e+003	3.9910e-002	1.6986e+001	5.4200e+003	4.1543e+002	7.3178e+002
	⁸⁵Rb	stable	8.4663e-003	3.6164e+001	5.5000e+003	1.1200e-001	3.0685e+001	5.5000e+003	4.1543e+002	7.3178e+002
2	³⁶Cl	1.10e+08	4.4612e-003	3.0685e+001	5.5400e+003	6.2736e-002	2.2466e+001	5.4200e+003	4.2154e+002	7.1099e+002
	¹²⁹I	5.73e+09	4.4615e-003	3.0685e+001	5.5400e+003	6.2739e-002	2.2466e+001	5.4200e+003	4.2154e+002	7.1099e+002
3	⁹⁰Sr	1.06e+04	3.0718e-003	2.3014e+001	5.5000e+003	4.5738e-002	2.1370e+001	5.5000e+003	4.0949e+002	7.3105e+002
	⁹⁰Y	2.67e+00	7.7395e-007	2.3014e+001	5.5000e+003	1.1524e-005	2.1370e+001	5.5000e+003	4.0949e+002	7.3105e+002
4	⁹⁰Zr	stable	3.3852e-003	5.1507e+001	5.5400e+003	4.1700e-002	4.0548e+001	5.5000e+003	4.0949e+002	7.3105e+002
	⁹⁹Tc	7.78e+07	2.0043e-003	2.5205e+001	5.4600e+003	2.8304e-002	1.9726e+001	5.3800e+003	4.2125e+002	7.1595e+002
5	¹³⁷Cs	1.10e+04	4.0868e-003	2.1918e+001	5.5000e+003	6.2798e-002	1.8082e+001	5.4200e+003	4.1706e+002	7.3982e+002
	¹³⁷Ba	stable	4.6088e-003	5.0411e+001	5.5400e+003	5.3604e-002	4.6575e+001	5.4000e+003	4.1706e+002	7.3982e+002

191

occurred and did not undergo sorption, they could induce an early breakthrough of plutonium, with the magnitude proportional to the proportion of plutonium fixed on the colloids. The IAEA (1999) emphasized that sampling at the atolls provided no evidence of the presence of natural colloids. In addition, they observed that "...the measured radionuclide concentrations in the waters of the cavity-chimney and the monitoring wells (Appendix V, Tables V.4, V.6 and V.11) as well as the K_d values calculated from these measurements (Appendix V, Table V.10) do not support the hypothesis of an accelerated plutonium or ^{241}Am transport by colloids."

Modeling to simulate colloid transport of radionuclides is essentially a simplification of the transport calculations performed previously; no retardation is included, either through sorption or matrix diffusion. The result of such a sensitivity is readily predictable: breakthrough will be faster and with higher mass than for situations including the retardation processes. As found by the IAEA, the impact will be directly proportional to the amount of radionuclide mass assumed to migrate on surfaces of colloidal particles and its release function. The amount migrating on colloids at Amchitka is unknown though reasonably expected to be quite small. The release apportioning assumed throughout the modeling here, that five percent of the refractory elements are available for immediate migration, is conservative and can be easily argued to be much smaller based on nuclear test studies.

Despite the lack of constraints on the sensitivity analysis, representatives of the State of Alaska Department of Environmental Conservation requested that transport calculations be performed that assume five percent of the mass of otherwise immobile radionuclides travels as colloids. The colloid-transport case was run for Long Shot because it was the only test displaying breakthrough of the Class 6 (refractory) radionuclides, though only for the matrix diffusion sensitivity case (see previous section). The results for ^{151}Sm are shown on Figure 6.13 for comparison with the matrix diffusion sensitivity case with ^{151}Sm breakthrough. The rare-earth elements have high boiling points, low solubilities, and high sorption to clays and zeolites. They have also already been implicated in colloid transport at the NTS (Buddemeier and Hunt, 1988) and as such are good analogs for plutonium and other actinides. ^{151}Sm is chosen over ^{152}Eu for its longer half-life (90 versus 13 years), as decay significantly impacts the effect of velocity variations and most of the radionuclides of interest for colloid transport are longer lived.

Comparing the peak mass breakthrough of ^{151}Sm for the low matrix diffusion sensitivity case with the case of no matrix diffusion or sorption shown here indicates an increase in peak mass of over 10 orders of magnitude for both the mean and standard deviation. Using a unit mass, the reasonableness of the State of Alaska scenario cannot be evaluated in terms of predicted concentration. However, once scaled by the classified data, the colloid concentrations resulting from this scenario can be evaluated in terms of solubility limits, colloid stability, and colloid concentration to determine if they are consistent with knowledge of radionuclide transport by colloids.

6.1.4 Transient Responses to Sea Level Change

As discussed in regard to the steady-state assumption of the conceptual flow model, the most significant transient process for the Amchitka groundwater system is the rise and fall of sea level in response to glacial cycles. These transients are documented as going in both directions: increases
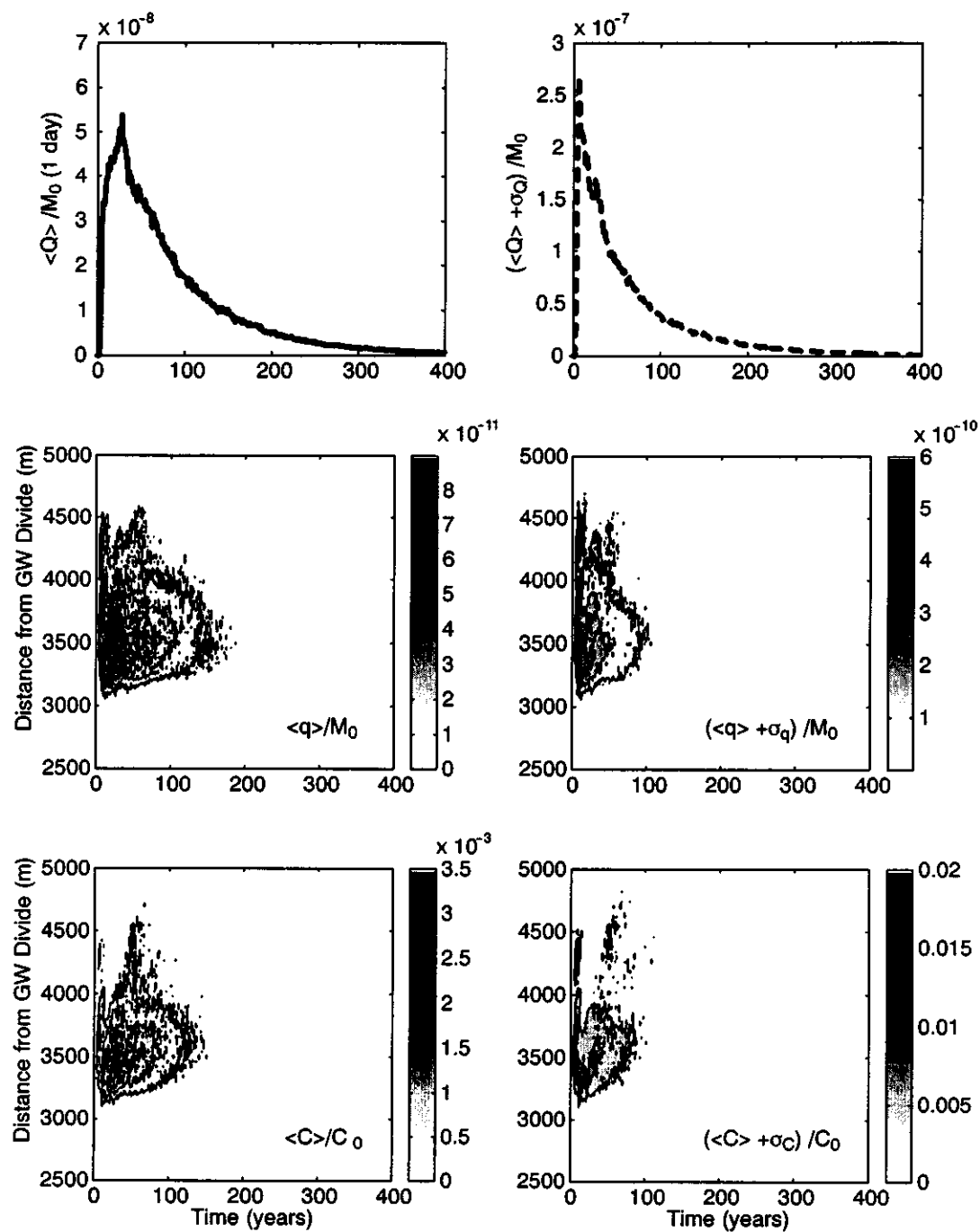
Figure 6.13. Results of simulating that five percent of the [151]Sm travels unretarded, simulating colloid-facilitated migration.

in sea level of up to 76 m above current sea level and decreases of as much as 91 m below current sea level have been identified by mapping marine terraces (Gard, 1977). The last major regression is estimated to have ended about 127,000 years ago, whereas the last major transgression presumably peaked in late Wisconsinian time, on the order of 10,000 years ago (Gard, 1977). As a result, the scenario of concern is that of a mean sea level lower than that today, followed by a rise to current sea level, and the response of hydraulic head and groundwater chemistry to that sea level increase.

This sensitivity was performed for the Cannikin site, as it has the largest discrepancy between pressure and chemical data. A representative flow realization was selected and the modeling parameters held constant. Using the site's bathymetry, decreasing the sea level pressure boundary, and increasing the recharge area to include the area between the current shoreline and 30 m below current sea level, equilibrium head and chemical distributions were generated. Then the sea level was instantaneously increased to its present level and the system's reaction to this change monitored for 5,000 years.

The results show the large difference in the response times of the pressure and chemical systems that the conceptual model suggested. Within 100 years of the sea level rising 30 m, the head in the freshwater lens and in the underlying seawater body are very close to their new equilibrium values (Figure 6.14 and Figure 6.15). Heads within the transition zone slowly approach their stable values over a couple of thousand years, but they differ from the equilibrium value by generally less than 10 m. The transition zone heads actually move in a rebounding fashion, re-approaching the lower initial values after rapidly increasing from the pressure change. This reflects the impact of density on the environmental head as the salinity profile slowly changes. In contrast, after 100 years from the sea level rise, the chemical profile is a little different from that in equilibrium with the 30-m-lower sea level. The simulations do not approach a new equilibrium for at least 2,000 years across much of the transition zone. For example, the Cl concentration at a depth of about 2,000 m below land surface at the location of UAe-1 begins at a concentration of about 5,200 mg/L under the lower sea level condition. One hundred years after the sea level rises, it has increased to only 7,600 mg/L, after 1,000 years it is about 12,600 mg/L, and another thousand years brings it to 14,000 mg/L. After 5,000 years, the salinity is at about 15,600 mg/L.

This slow modeled response in the chemical system is probably overly rapid compared to reality because the process of matrix diffusion is not included in the simulation (it is simulated in the radionuclide transport calculations through the particle tracking). The equilibration presented in Figure 6.14 is a result solely of the varying velocity field. Presuming that the low sea level stand was of sufficient duration to equilibrate the matrix blocks as well as fractures with fresh water, the equilibration time as sea level rose would exhibit an even longer tailing as fresh water diffuses from the blocks and more saline water diffuses into them.

The significance of this sensitivity analysis is that it substantiates the conception that of the two sets of calibration data, the head data are more likely to be in equilibrium with the current conditions than the groundwater chemical data. Comparing the chemical data from UAe-1 to the simulation, many of the data appear representative of a much lower sea level condition than present, a situation consistent with the ^{14}C age dates in excess of 8,000 years. At Milrow, the large degree of vertical
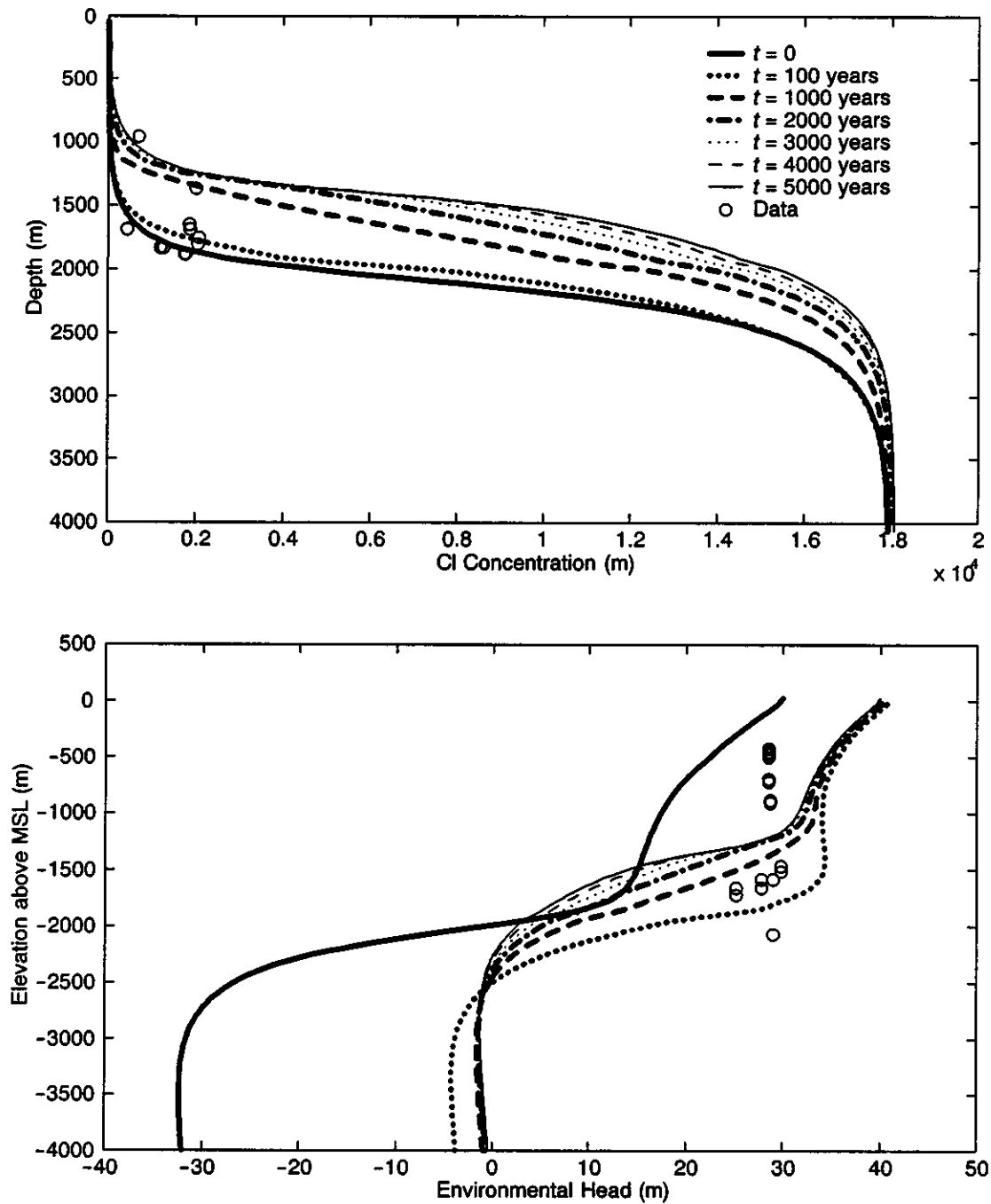
Figure 6.14. Changes in the concentration and head profiles at the UAe-1 location in response to a rise in sea level from an assumed glacial condition at 30 m below present sea level.
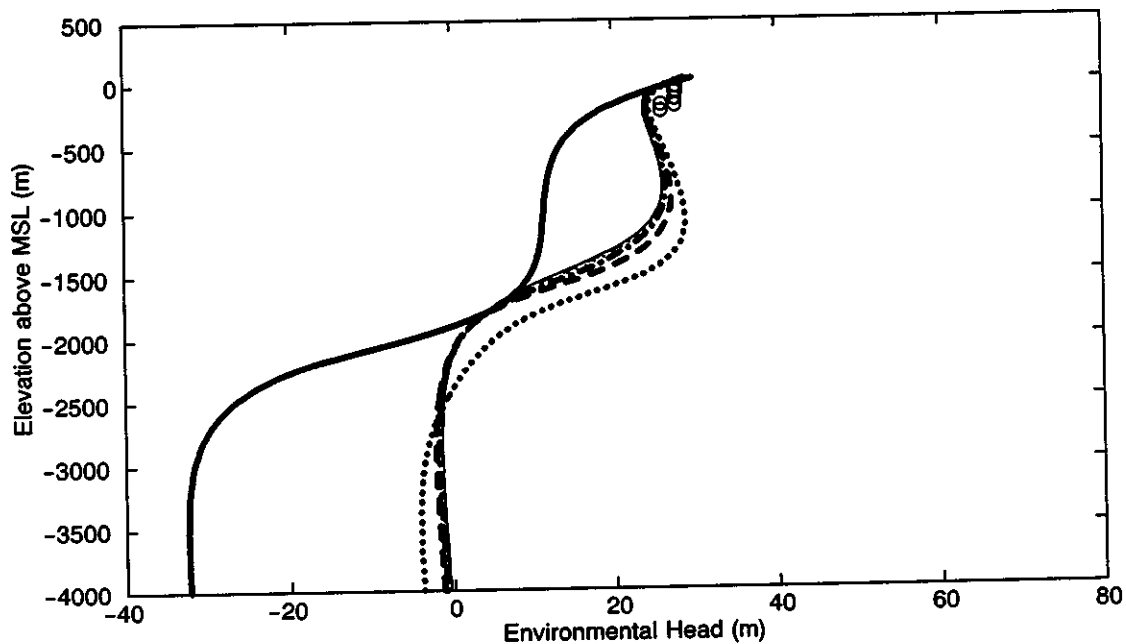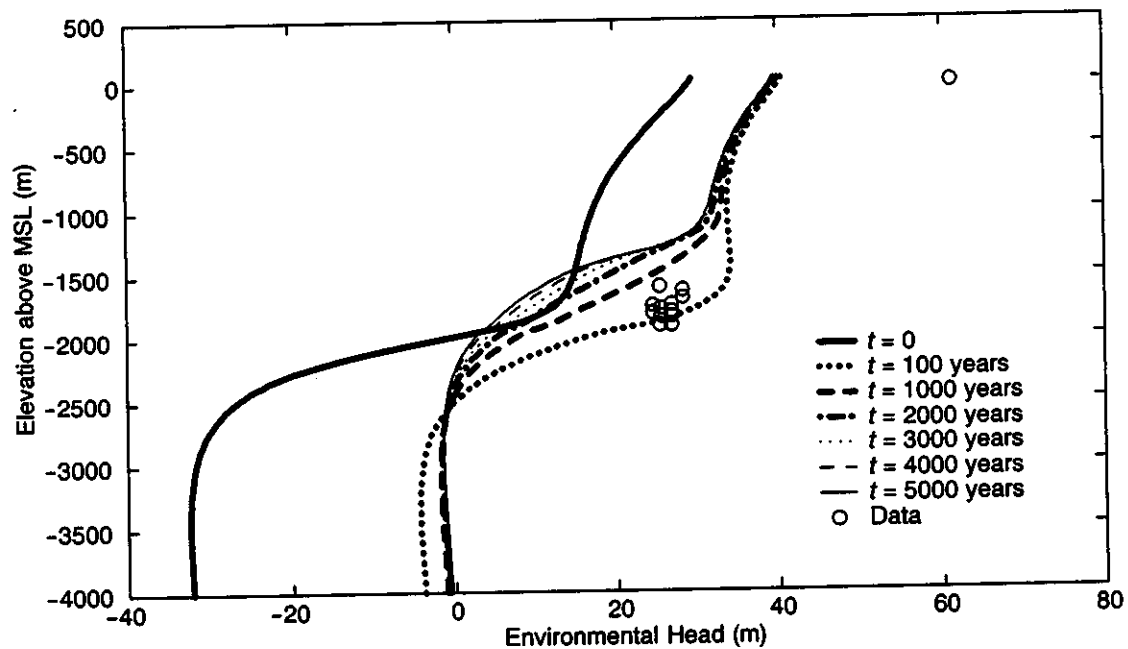
Figure 6.15. Changes in the head profiles at the UA-1 and HTH-1 locations in response to a rise in sea level from an assumed glacial condition at 30 m below present sea level.

spreading evident for the transition zone in the groundwater chemical data may also be due to the slow chemical equilibration to sea level changes, again indicating that dispersion observed in the chemical profile represents a transient effect.

6.1.5 Island Half-Width

As discussed in Section 2.1.1, the conceptual model for groundwater flow at Amchitka assumes that a groundwater divide runs along the long axis of the island, separating flow to the Bering Sea on one side and flow to the Pacific Ocean on the other. The position of the divide is also assumed to coincide with that of the surface water divide. This assumption can be called into question due to the observation of asymmetry in the freshwater lens beneath the island (Fenske, 1972). This asymmetry is supported by the data analysis and modeling performed here, which suggests that the freshwater lens is deeper at Long Shot and Cannikin than at Milrow.

Not only is there uncertainty as to whether the groundwater and surface water divides coincide, there is additional uncertainty in the location of the surface water divide itself, as the topography of the island in the area of the nuclear tests is very subdued. The surface water divide was estimated using a detailed series of topographic maps at a scale 1:6,000 and with a 10-foot contour interval, created for Amchitka by the U.S. AEC (41 map sheets known as the Amchitka Island Map Atlas; Holmes and Narver, 1976). Despite this resolution, the distance between 10-foot elevation contours can reach over 100 m in places.

To understand the impact of this uncertainty on the groundwater modeling, several sensitivity cases were evaluated. In these, the island half-width was assumed to be 200 and 400 m wider than the estimate for Milrow, and also assumed to be 200 and 400 m narrower than used in the base-case model. For reference, the base-case half-width used at Milrow is 2,062 m so that plus and minus 10 and 20 percent differences are considered here. One realization was used for these calculations, one in which the cavity is located in the freshwater lens. It shows a 100 percent mass breakthrough and has the parameter values $K = 2.34$ x 10^{-2} m/d, $Rech = 1.82$ cm/yr and $\theta = 1.62$ cx 10^{-4}.

Varying the island half-width both affects the depth to the transition zone (through varying the land surface available for recharge) and the position of the cavity in the flow system (by virtue of changing the distance from the test to the no-flow boundary). These effects can be seen on Figure 6.16 and Figure 6.17. Reducing the island half-width decreases the depth of the transition zone, and cuts the distance between the cavity and the transition in half for the 400-m-shorter half-width. Conversely, the transition zone is deepened by an increasing half-width, increasing the distance from the cavity to the transition zone by a factor of two for the 400-m-wide island. The flowpath distance to the seafloor from the cavity is also affected, lengthening for a wider island and shrinking for a smaller one.

The impact of these various configurations on transport is shown in Figure 6.18. What is first obvious from the breakthrough curves is that a difference of ± 200 m in the island half-width has a limited influence on the breakthrough behavior, despite the transition zone moving up or down a couple of hundred meters. This sensitivity can be expected to be higher if the cavity is positioned closer to the transition zone than evaluated here. Once the half-width changes by 20 percent,
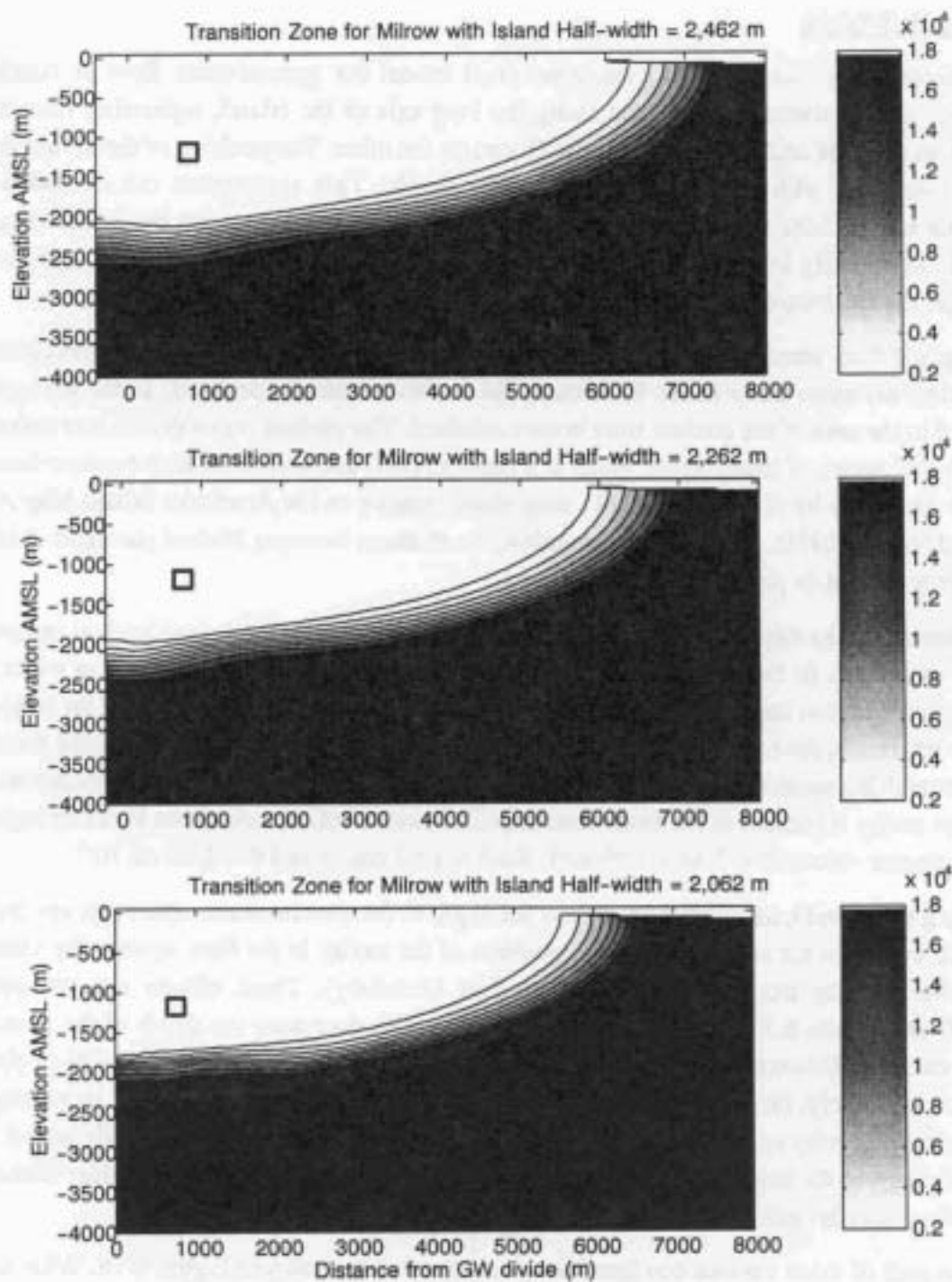
Figure 6.16. Variation in transition zone configuration for one realization of the Milrow model with the base-case island half-width (2,062 m) and 200 and 400 m wider.
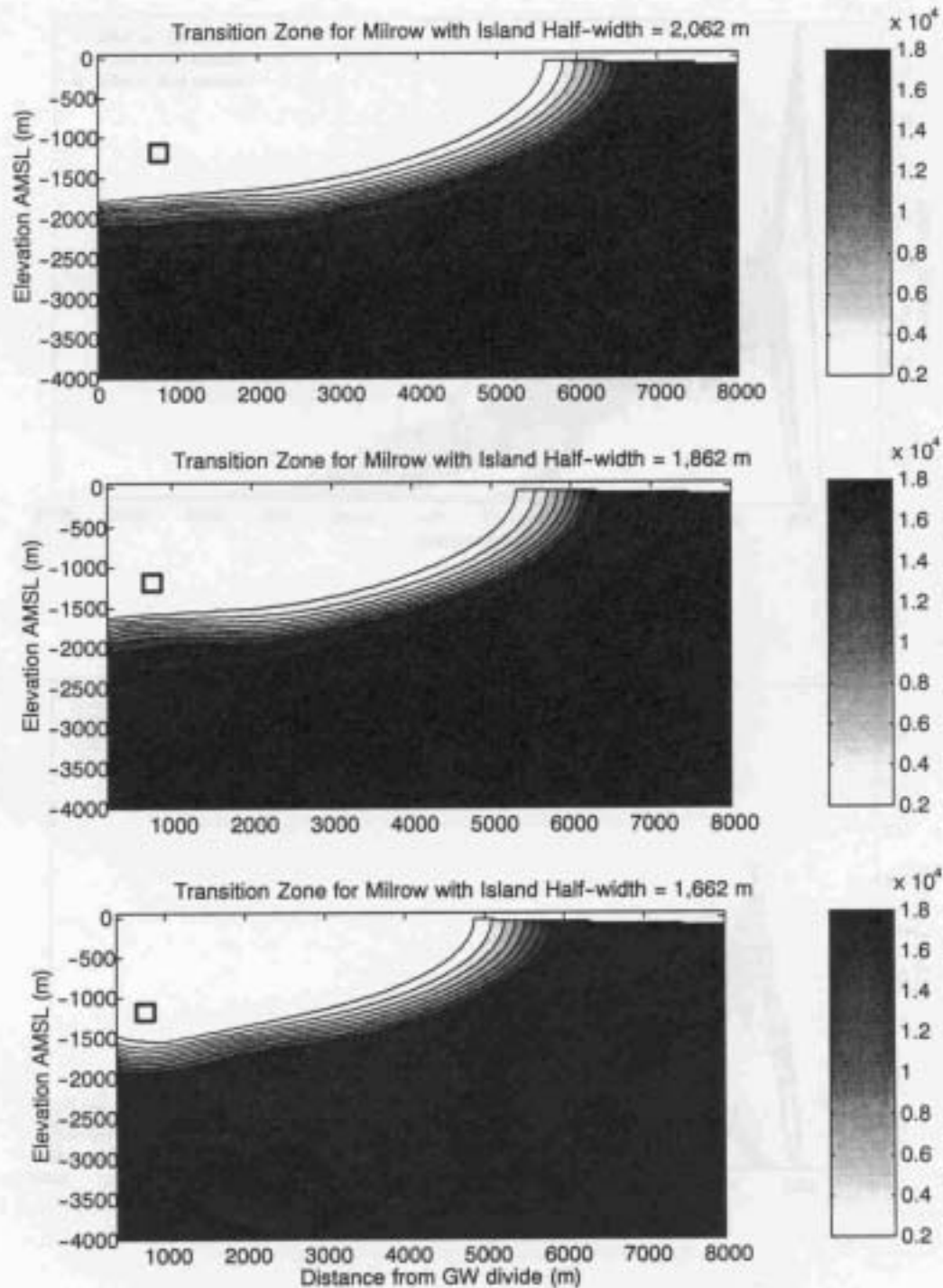
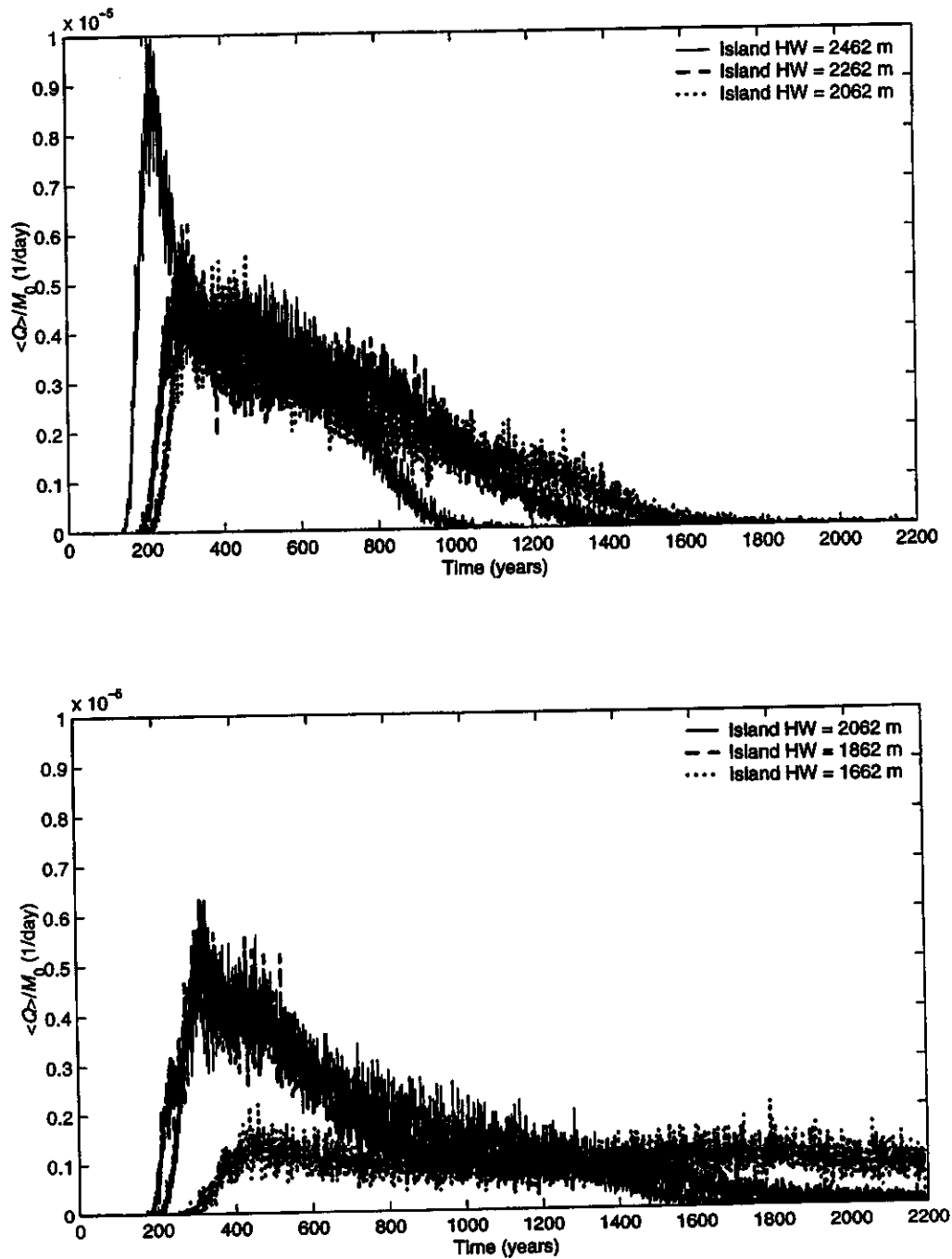Figure 6.17. Variation in transition zone configuration for one realization of the Milrow model with the base-case island half-width (2,062 m) and 200 and 400 m shorter.

Figure 6.18. Undecayed, non-retarded breakthrough curves for one realization of the Milrow model under conditions of varying island half-width. The base case is 2,062 m.

however, a noticeable impact on the breakthrough is observed. A 400-m-longer half-width leads to an earlier breakthrough of mass at a peak flux about two times larger than the base case. A 400-m-shorter half-width results in a delay in breakthrough at a peak mass about five times lower than the base case.

If the half-width estimates are in error in the site models, the noted asymmetry in the freshwater lens can be used to infer the direction of the error. As the transition zone is more shallow at Milrow than the Bering-side sites, it is possible that the groundwater divide may be closer to the Pacific side of the island. If so, the Milrow breakthrough results in Section 5 would be too high and the Long Shot and Cannikin results too low. From the sensitivity runs, the magnitude of this potential error is probably on the order of a factor of two or three. It is important to note that the flat topography and ready availability of recharge do not support a groundwater divide largely different from the topographic divide. The asymmetry in the freshwater lens may be due to hydrogeologic factors other than the half-width, such as hydraulic conductivity, variations of which are accounted for in the site-specific calibrations.

6.1.6 Geothermal Heat

This Section describes the impacts of including geothermal heat in the Milrow model (referred to here as the geothermal model). The availability of hydraulic head, concentration, and temperature data sets and their high degree of confidence at Milrow make this site the most suitable for the sensitivity study of geothermal effects. These simulations are run using FEFLOW, and use the same two-dimensional finite-element mesh as the Milrow isothermal flow simulations described in Sections 2, 4, and 5. The geothermal model is configured to simulate pre-nuclear test conditions; therefore, the chimney is not included and K and θ are treated as homogeneous properties throughout the domain. With the exceptions noted below, values of the groundwater flow parameters are the same as the values used in the calibrated flow model of Milrow (as described in Section 2.4.1). These values, as well as the values of the parameters required for the geothermal component are listed in Table 6.4. Fluid density and viscosity are dependent on both concentration and temperature, based on a nonlinear relationship of density to temperature incorporated in the FEFLOW code. The value of rock volumetric heat capacity, $c_s \varrho_s$, is estimated from a specific heat capacity, c_s, of 0.84 J/gm-°C determined from EH-1 core samples (Greene, 1965) and an average rock density, ϱ_s, of 2.3 gm/cm^3 determined from laboratory derived dry bulk density values of core samples from UAe-1, UAe-2, UAe-3, and UAe-6 (Lee, 1969a, b, c, d) and the lithologic log of UAe-2 (Ballance, 1968). The value of rock thermal conductivity, λ_s, is estimated from laboratory tests of core samples from EH-1 (Greene, 1965). The volumetric heat capacity and thermal conductivity of water are FEFLOW default values.

Temperature profiles measured in several deep Amchitka Island boreholes (Sass and Moses, 1969) guide the choices of fixed temperature boundary conditions. UAe-2 displays the highest temperature gradient of all the Amchitka boreholes, a gradient of 3.2°C per 100 m. This gradient is considerably higher than an average crustal value of 2.5°C per 100 m reported by Freeze and Cherry (1979), presumably as a result of volcanic activity along the Aleutian Ridge. Extrapolation of the UAe-2 profile to ground surface indicates a mean annual ground-surface temperature of about

4°C and this value is used for the temperature boundary along the upper surface of the model. This is consistent with the 3.9°C daily mean temperature noted for Amchitka (Armstrong, 1977). Likewise, the temperature of 125°C specified at the bottom boundary of the model is estimated by extrapolating the UAe-2 temperature profile to an elevation of -4,000 m AMSL. Temperatures specified along the right (seaward) boundary vary linearly with depth from 4°C at the top to 125°C at the base. The specified-recharge and concentration boundary conditions are the same as those used in the calibrated isothermal model, but the specified-head boundaries now account for the buoyancy effect imparted by the increased geothermal temperature at depth.

Table 6.4.   Values of parameters used in FEFLOW for simulations incorporating geothermal heat.

Parameter	Value
Horizontal Hydraulic Conductivity, K_{xx}	6.77×10^{-3} m/d
Vertical Hydraulic Conductivity, K_{zz}	6.77×10^{-4} m/d
Specific Storage, S_s	1.0×10^{-4}
Recharge, *Rech*	1.125 cm/yr
Fracture Porosity, θ	5.0×10^{-4}
Mass Longitudinal Macrodispersivity, A_L	100 m
Mass Transverse Macrodispersivity, A_T	10 m
Mass Diffusion, D^*	1.0×10^{-9} m^2/s
Density Ratio	0.025
Rock Volumetric Heat Capacity, $\varrho_s c_s$	1.9×10^6 J/m^{3}C
Water Volumetric Heat Capacity, $\varrho_0 c_0$	4.2 J/m^{3}C
Rock Thermal Conductivity, λ_s	2.59 J/m^{3}C
Water Thermal Conductivity, λ_0	0.56 J/m^{3}C
Thermal Longitudinal Dispersivity, B_L	100 m
Thermal Transverse Dispersivity, B_T	10 m
Water Density and Viscosity, ϱ_0 and μ_0	6th order function of temperature

The geothermal sensitivity run adds geothermal heat to the base-case Milrow model, with the values of all flow parameters unchanged from the base-case model. Thermally driven buoyant flow caused by the geothermal gradient in this case increases the vertical upward flux below the island and shifts the transition zone almost 200 m higher relative to the isothermal case (Figure 6.19). At the transition zone, this increased vertical flux is then directed seaward, resulting in higher velocities along the transition zone as compared to the isothermal case. Despite these differences, the overall patterns of flow are similar to the isothermal case.

The upward and left (toward the divide) components of velocities simulated below the transition zone are both larger due to the buoyancy-driven flow simulated in the geothermal model. Higher flow rates mean that velocities near the working point, which is located below the transition zone at Milrow, are higher when including the effects of geothermal heat (Figure 6.20). The vertical
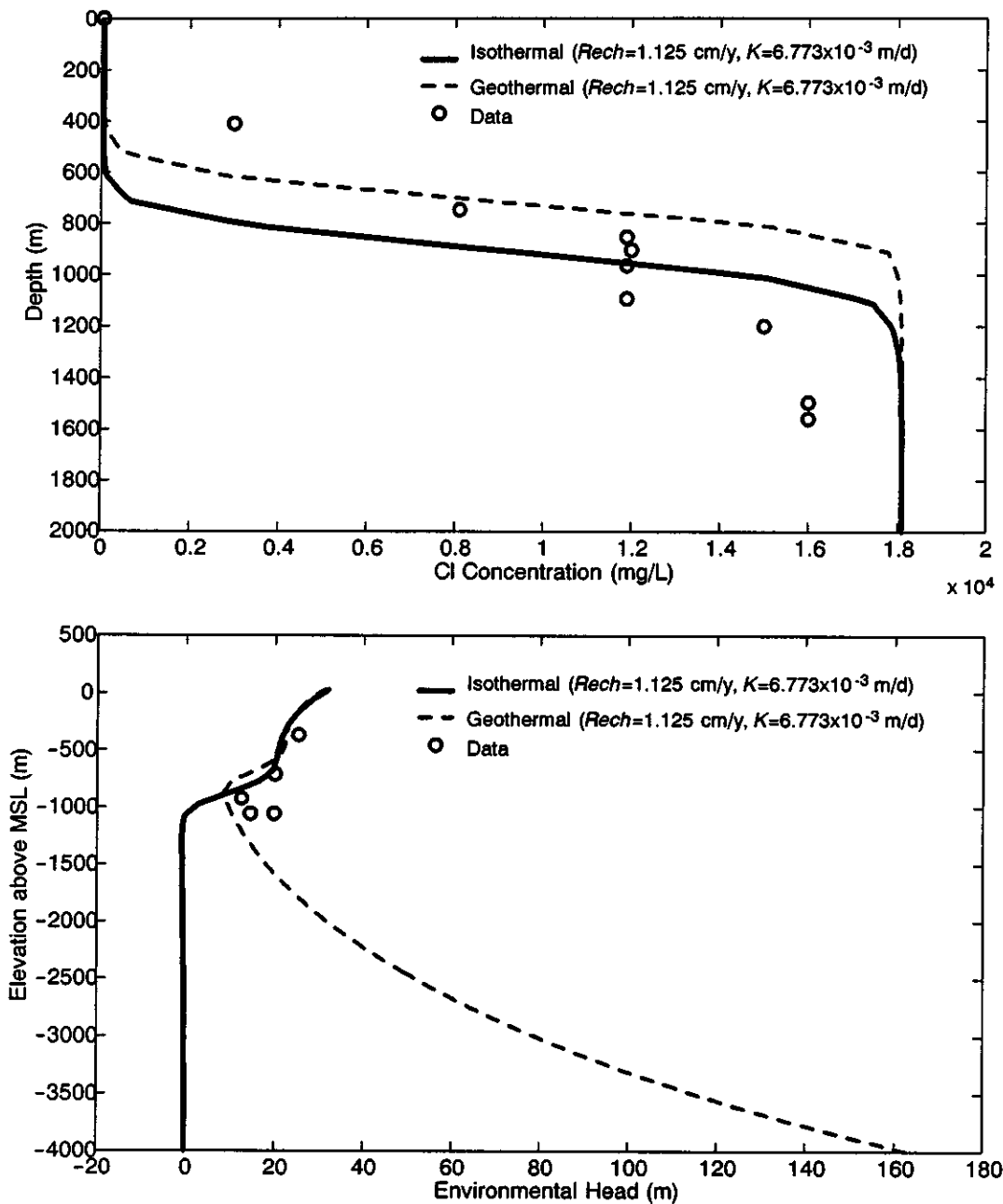
Figure 6.19. Comparison of profiles of head, concentration and temperature simulated by the isothermal and geothermal models, and values measured at UAe-2.

and horizontal velocities at the Milrow working point are about twofold higher in the geothermal model. Velocities higher than the isothermal model are generally maintained along the predicted flowpaths from the working point toward the sea, suggesting that inclusion of geothermal heat in the model simulations has the effect of reducing contaminant travel times for the Milrow and Cannikin sites where the working points are below the transition zone in many of the realizations considered.
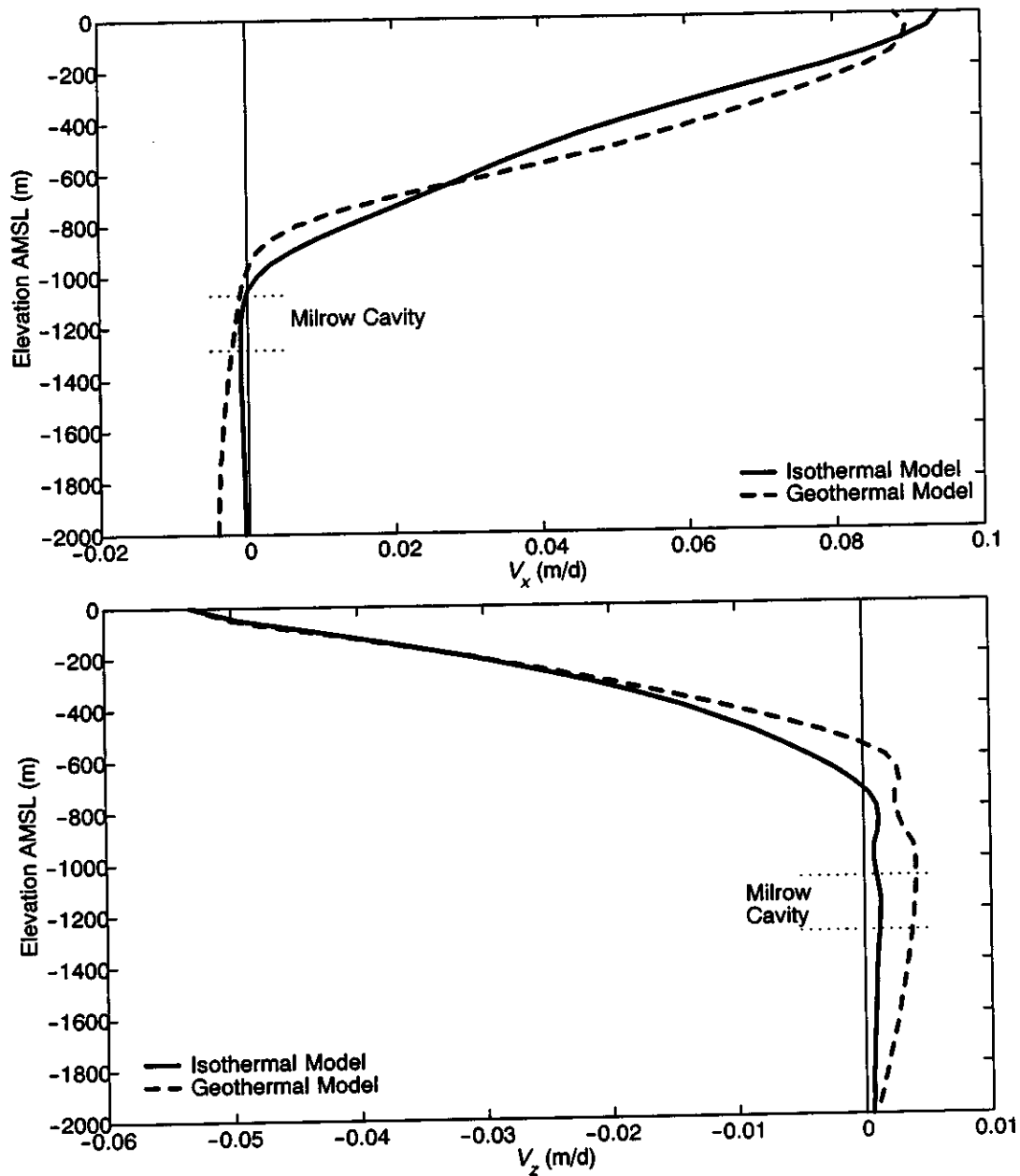
Figure 6.20.   Comparison of velocity profiles along a vertical line through the working point of Milrow for isothermal and geothermal models.

The comparison of non-decayed, non-retarded breakthrough curves shows the impact of the higher velocities for the geothermal as compared to the isothermal case (Figure 6.21). The geothermal case exhibits more rapid breakthrough and a peak mass value between three and four times higher than in the isothermal simulation. Recall that this difference applies only when the transition zone is at or above the test cavity and that the impact of including geothermal heat is minimal above the transition zone as can be seen from the velocity profiles of Figure 6.20.
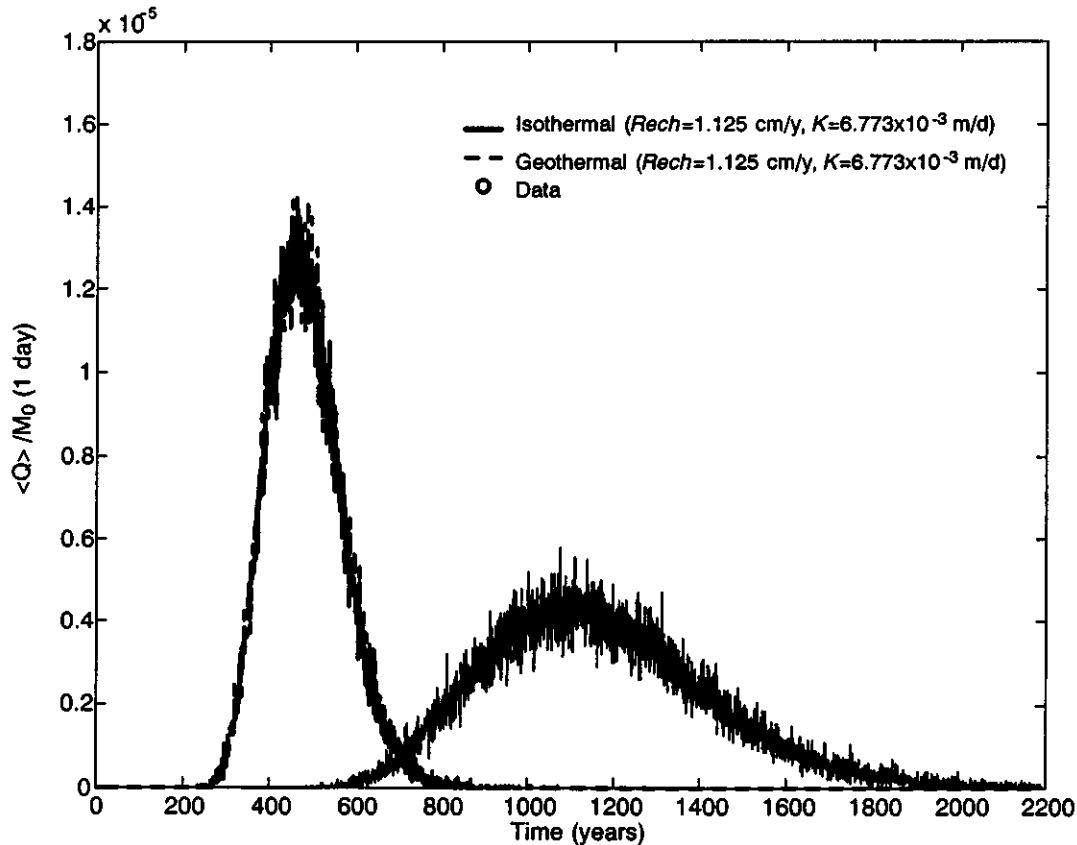
Figure 6.21. Comparison of mass breakthrough at the sea floor for non-decayed, unretarded, solutes under isothermal conditions and geothermal conditions.

6.2 Three-Dimensional Sensitivity Studies

The modeling presented thus far uses a two-dimensional (2-D) perspective to analyze the flow and transport problem. As discussed in Section 2.1.1, the island hydraulic environment lends itself to a 2-D approach. The 2-D vertical formulation of the base-case model relies on the assumption that groundwater flow is essentially perpendicular to the long axis and shoreline of the island, such that the mesh configuration is parallel to this flow. This simplifying assumption is considered reasonable for the conceptual model and is significantly more computationally efficient than a fully three-dimensional (3-D) formulation. However, there are several conceptual model assumptions that require a 3-D approach to analyze and this in turn causes an evaluation of the effect of neglecting the third dimension in the majority of modeling.

The 3-D density-dependent flow and mass transport simulations are run using the FEFLOW code. The coordinate directions of the models are such that x and z are the same as in the 2-D case and the third dimension of y is the horizontal distance parallel to the shore. The finite-element mesh geometry of each vertical slice in the 3-D models is identical to the mesh geometry of the 2-D Cannikin model, with the addition of a width of each element in the y direction (perpendicular to

205

the axes of the 2-D model). Each slice is of uniform width such that there is no variation in model geometry across the overall width of the model.

All of the sensitivity studies presented here are applied to three realizations out of the 260 run for the Cannikin model in 2-D. The three realizations were chosen to span the gamut of breakthrough behavior observed in the simulations, ranging from about 28 percent to 60 percent to almost 100 percent breakthrough at the ocean floor (Figure 6.22). The 260 realizations were first categorized according to amount of breakthrough and porosity and three realizations were selected that spanned the breakthrough range but had virtually identical porosity (the realizations selected all have a porosity of about 2.67 x 10^{-4}). As already demonstrated, the velocity field is very sensitive to porosity, so it was held constant to reveal the impact of the sensitivity cases. The recharge-conductivity ratios of these three realizations were then used for the sensitivity modeling to derive the velocity field for particle tracking. Note that these ratios result in poor fits to the calibration data in some cases, but the objective here is simply to assess the possible impact on breakthrough. The three realizations encompass the variety of positions of the transition zone relative to the test cavity that result from the various parameter combinations.
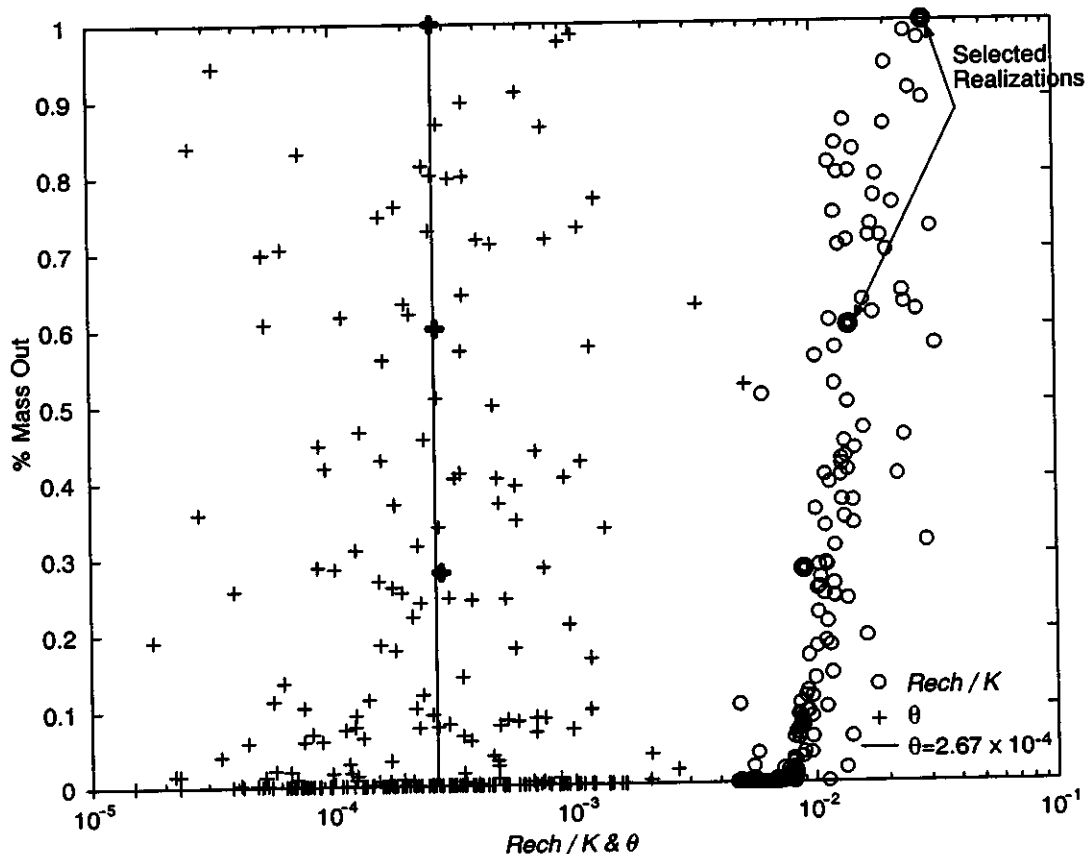

Figure 6.22. Selection of realizations for 3-D modeling. Three realizations were chosen from the Milrow simulations that covered the range of breakthrough behavior (percent mass breakthrough at the ocean floor), but that had very similar porosity values. The corresponding recharge-conductivity ratios were used in the 3-D modeling.

206

The relative position of the transition zone to the Cannikin cavity for the three selected realizations can be seen in Figure 6.23. Though these realizations were selected from the Monte Carlo realizations generated for Cannikin, the various positions of the transition zone relative to the cavity allow them to represent flow fields possible for all three tests. The realization with the transition zone well below the cavity is representative of Long Shot. The realizations with the cavity within and below the transition zone are likely to be more representative of Milrow and Cannikin.

6.2.1 Flow in the Rubble Chimney

The rubble chimney formed in response to a nuclear explosion disrupts the natural state of the surrounding rock, creating heterogeneity in the spatial distributions of K and porosity. Unlike the homogeneity assumed for the natural rock, the changes in K and porosity are a limited local feature, centered over the working point of the nuclear test. The 2-D formulation correctly accounts for the vertical boundaries of the chimney only in the direction parallel to the mesh configuration (the x-axis of the model), i.e., parallel to the natural flow direction, and treats the chimney as extending infinitely in the lateral direction (perpendicular to the model mesh and perpendicular to the natural flow direction). The implication is that the 2-D model treats flow in the chimney as occurring in an infinitely wide feature (that is, wide in the direction perpendicular to the 2-D mesh). In reality, the chimney is only as wide perpendicular as it is parallel to natural flow, and can be treated realistically only in a 3-D model.

The geometry of the model representing 3-D flow in the rubble chimney is based on the Cannikin site to be consistent with the model incorporating heat derived from the Cannikin nuclear test (described in section 6.2.2 below). The model is comprised of 15 100-m-wide vertical layers of elements, giving a total model width of 1,500 m perpendicular to the natural flow direction (Figure 6.24). There are, therefore, 16 vertical layers of nodes separating these layers. The location and configuration of the chimney in the x-z plane is identical to the chimney in the 2-D Cannikin simulations, and extends across three slices, or 300 m, in the center of the 3-D domain. The chimney is simulated as a vertical, rectangular column having a width in the x-y plane of about two R_c, where R_c is the cavity radius (estimated to be 157 m). The hydraulic properties of the rock beyond this radius are considered to be not significantly affected by the nuclear explosion and are assigned the background values of K and porosity. IAC (1998) modeled filling times of underground nuclear tests at Mururoa and Fangataufa atolls under several scenarios of fracturing beyond the cavity and concluded that observed filling rates are consistent with very little damage (fracturing) outside the cavity/chimney.

Boundary conditions and values of the groundwater flow and mass transport parameters for the three realizations are shown in Table 6.5. Conceptually, the rubble chimney acts as a conduit that promotes vertical flux, given the higher vertical conductivity in that region. Modeling the chimney in 3-D provides the geometry required to simulate groundwater entering the chimney from all radial directions, rather than the two directions allowed by the 2-D representation. Similarly, horizontal flow may exit the chimney at the transition zone in radial directions other than the seaward direction simulated in the 2-D model.
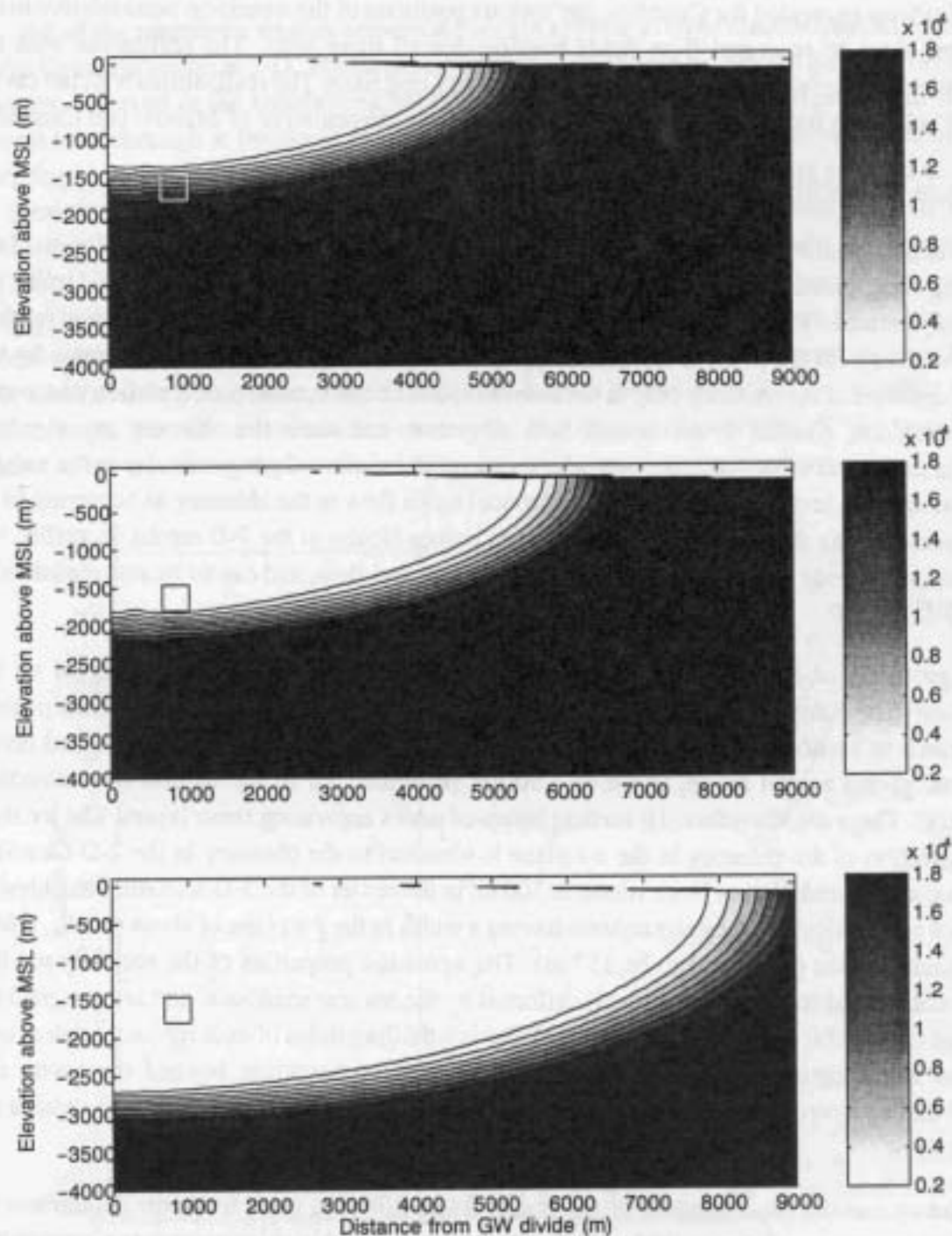
207

Figure 6.23. Salinity in the island groundwater system, expressed as concentration of chloride in mg/L, for the three realizations identified in Figure 6.22, as calculated in 2-D with the nuclear chimney included.
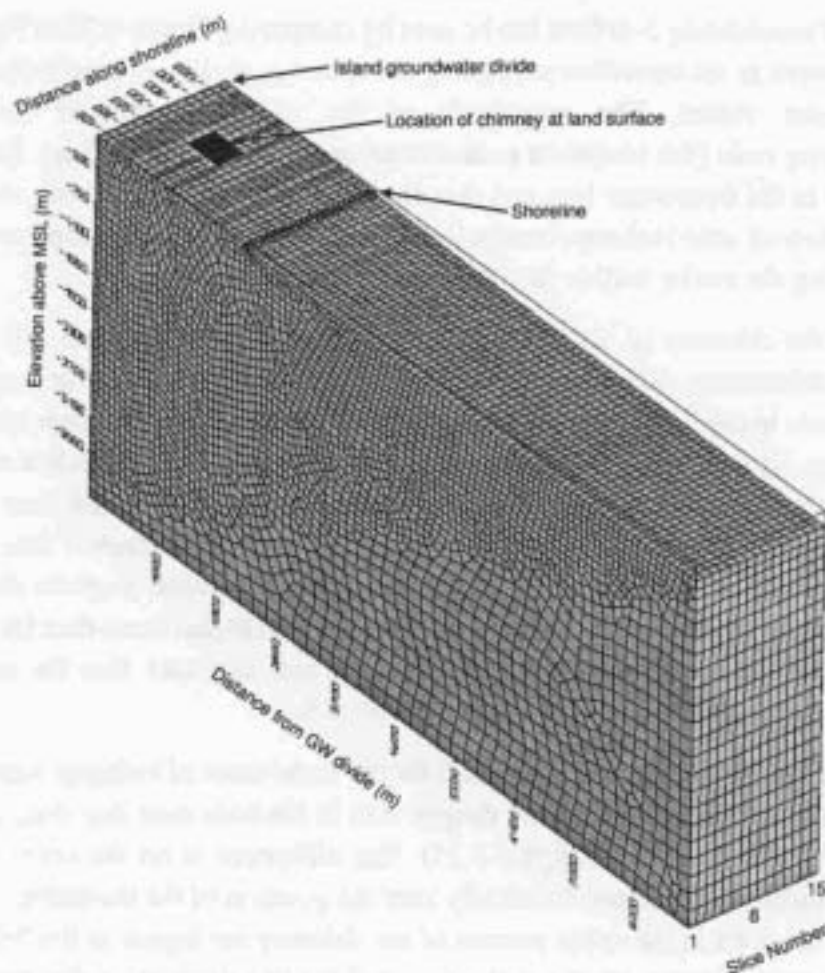
Figure 6.24.   Design of finite-element mesh used for the 3-D model of flow in the Cannikin cavity
and rubble chimney. All vertical layers are 100 m wide.

Table 6.5. Values of parameters used in three-dimensional simulations incorporating the rubble chimney.

Parameter	Realization #1	Realization #2	Realization #3	All Cases
Horizontal Hydraulic Conductivity, K_{xx} and K_{yy}	1.86×10^{-2} m/d	6.48×10^{-3} m/d	1.78×10^{-3} m/d	
Vertical Hydraulic Conductivity, K_{zz}	1.86×10^{-3} m/d	6.48×10^{-4} m/d	1.78×10^{-4} m/d	
Cavity and Chimney, K_{xx}, K_{yy} and K_{zz}	1.86×10^{-2} m/d	6.48×10^{-3} m/d	1.78×10^{-3} m/d	
Specific Storage, Ss				$1.\times10^{-4}$
Recharge, Rech	6.13 cm/yr	3.33 cm/yr	1.89 cm/yr	
Fracture Porosity, θ	2.81×10^{-4}	2.71×10^{-4}	2.67×10^{-4}	
Chimney Porosity				0.07
Mass Longitudinal Macrodispersivity, A_L				100
Mass Longitudinal Macrodispersivity, A_T				10
Mass Diffusion, D^*				1.0×10^{-9} m²/s
Density Ratio				0.025

The impact of considering 3-D flow can be seen by comparing Figure 6.25 to Figure 6.23. The 3-D formulation results in the transition zone being simulated as shallower than in the 2-D case with the same parameter values. The magnitude of the change is largest for the highest recharge/conductivity ratio (the transition zone moves upward by about 500 m). Despite this, the test cavity remains in the freshwater lens and thus flow velocities from the cavity are not impacted significantly. The lowest ratio recharge/conductivity case sees the transition zone move upward by about 100 m, placing the cavity further into the low velocity saltwater zone.

The effect of the chimney on the transport results is larger in 3-D than in 2-D (Figure 6.26). In 2-D, the two realizations with the cavity in or below the transition zone experience more breakthrough of mass in the 2,200 year model timeframe (28 vs. 18 percent mass breakthrough for realization #1, 52 vs. 33 percent for realization #2). With the transition zone below the cavity, both the 2-D and 3-D calculations result in 100 percent breakthrough in the model time frame, but the breakthrough is later and spread over more time for the 3-D case. The result is that the 2-D model underestimates the effect of the chimney on slowing particle velocities, neglects dispersion in the third dimension, and results in slightly earlier breakthrough with higher mass than the 3-D case. This result is true for all three recharge/conductivity ratios and indicates that the use of the 2-D approximation for transport from the cavities is conservative.

The impact of the chimney on the flow field for the three cases of recharge/conductivity ratio is to cause the transition zone to be pushed deeper than in the base case that does not include the chimney (compare Figure 6.27 with Figure 6.25). The difference is on the order of a couple of hundred meters at most, and does not drastically alter the position of the transition zone relative to the cavity. Darcy velocities in the upper portion of the chimney are higher in the 3-D formulation, and are directed downward from ground surface toward the transition zone. Because the chimney is simulated as extending to ground surface, it captures a larger proportion of recharge through radial flow into the chimney than the 2-D formulation, and this may account for the resulting deeper transition zone.

The greater flux through the chimney causes lateral spreading of particles originating in the cavity, a process that does not occur in the 2-D model. Comparing particle trajectories and distribution for 3-D realization #1 with and without the chimney (Figure 6.28) shows the plume width closely approximating the cavity size when the chimney is not included. With the chimney, lateral spreading (parallel to the shore) occurs, at least doubling the width of the plume. Some of the spread even occurs away from shore, toward the groundwater divide. The lateral spreading is due to the higher flux, induced by the high vertical conductivity, exiting in all directions from the chimney conduit. The net effect will be lower contaminant concentrations as the plume is diluted with a larger volume of groundwater.

The impact of the chimney on the transport results for the three cases is dramatic (Figure 6.29). Without the chimney, all three realizations experience breakthrough of 100 percent of the mass in the 2200-year model timeframe. When the chimney is included, only the case with the transition zone well below the cavity has complete breakthrough, and even then the breakthrough is spread over a much longer time. The large impact is not related to the relatively minor effect of the chimney
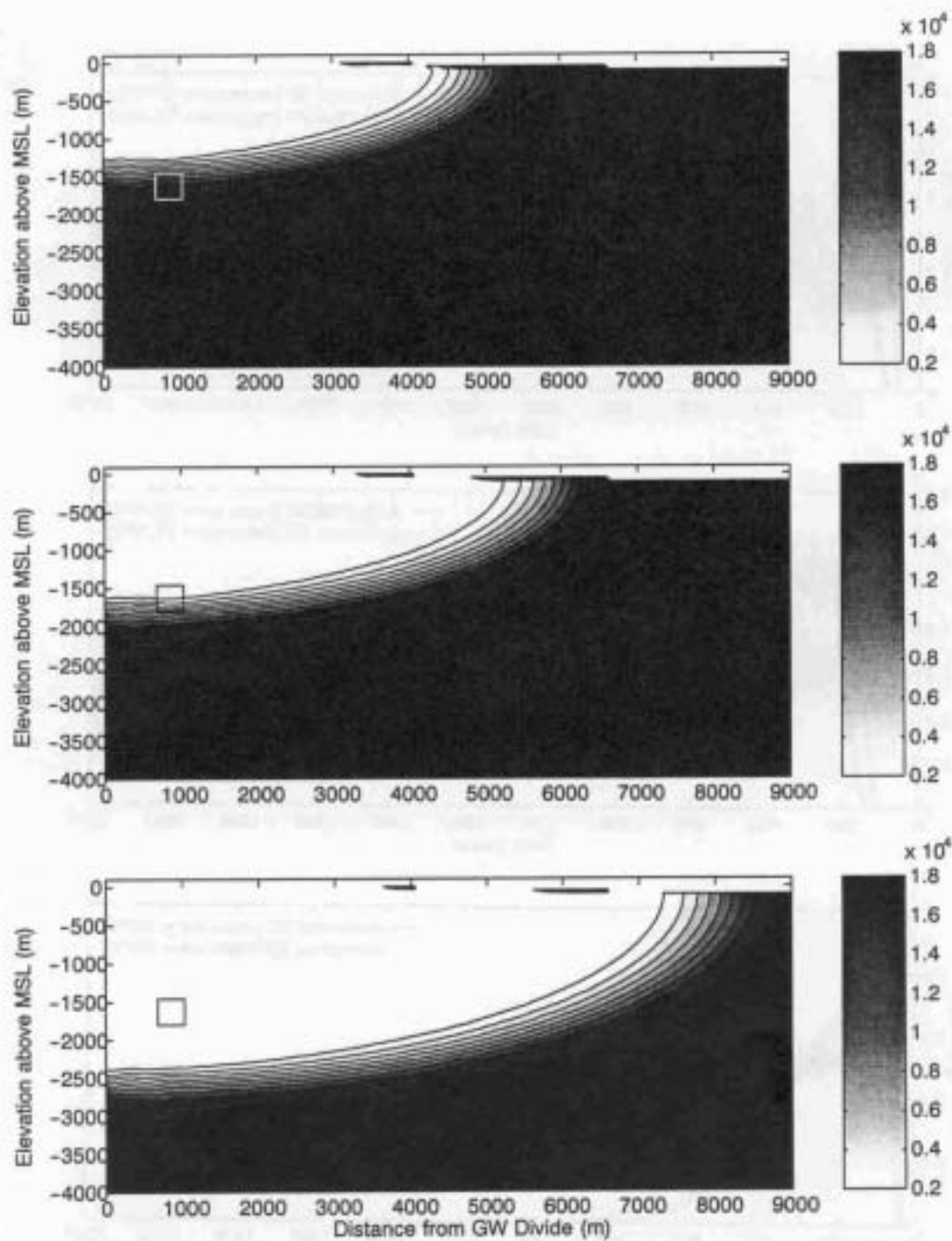
210

Figure 6.25. Salinity in the island groundwater system, expressed as concentration of chloride in mg/L, for the three select realizations, for the 3-D model including the nuclear chimney. Compared to the 2-D model (Figure 6.23), the transition zone is shallower.
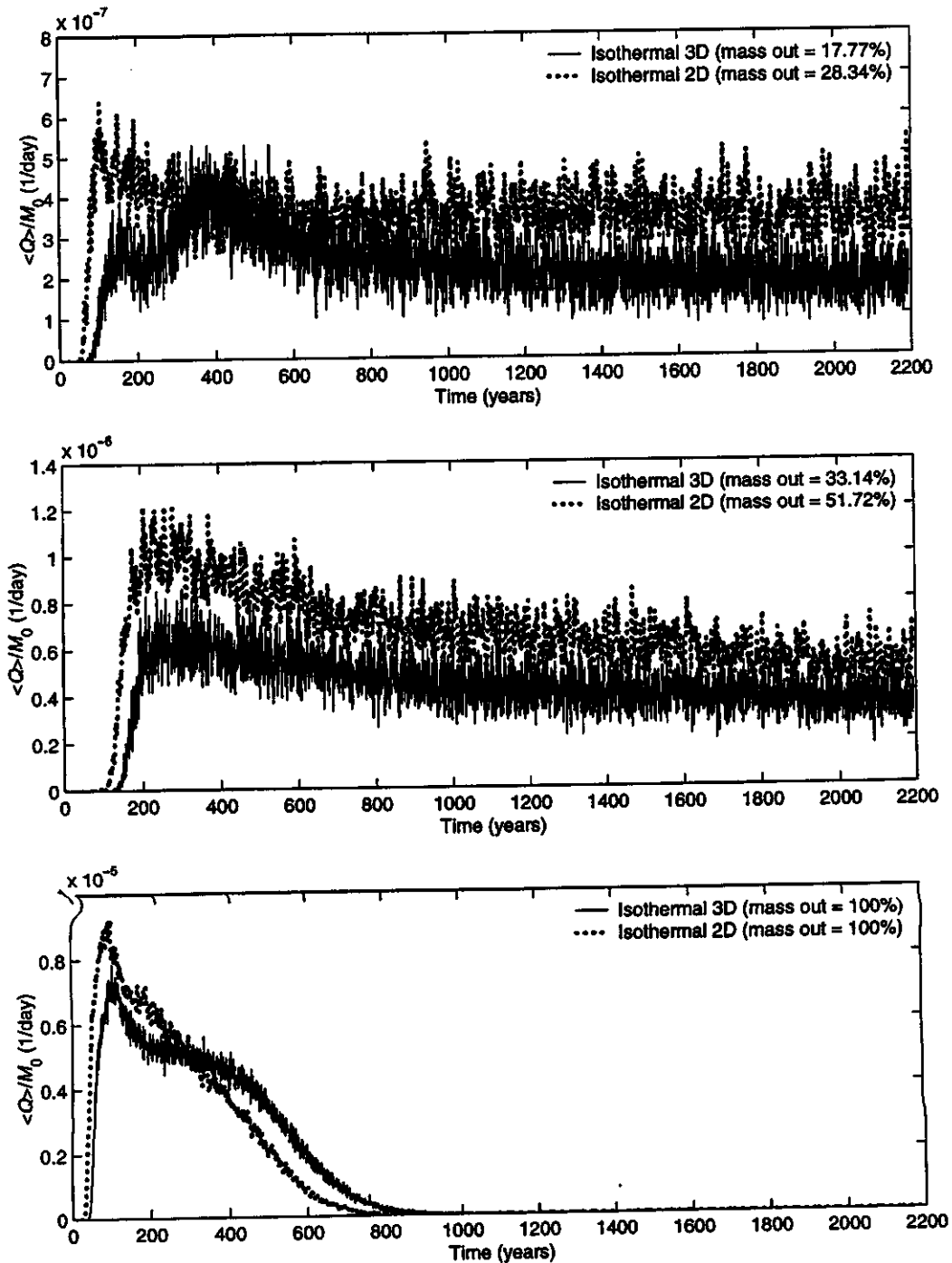
Figure 6.26. Breakthrough of undecayed, non-retarded particles in 2-D and 3-D domains with both including a nuclear chimney. Each graph represents a different case of recharge/conductivity ratio.
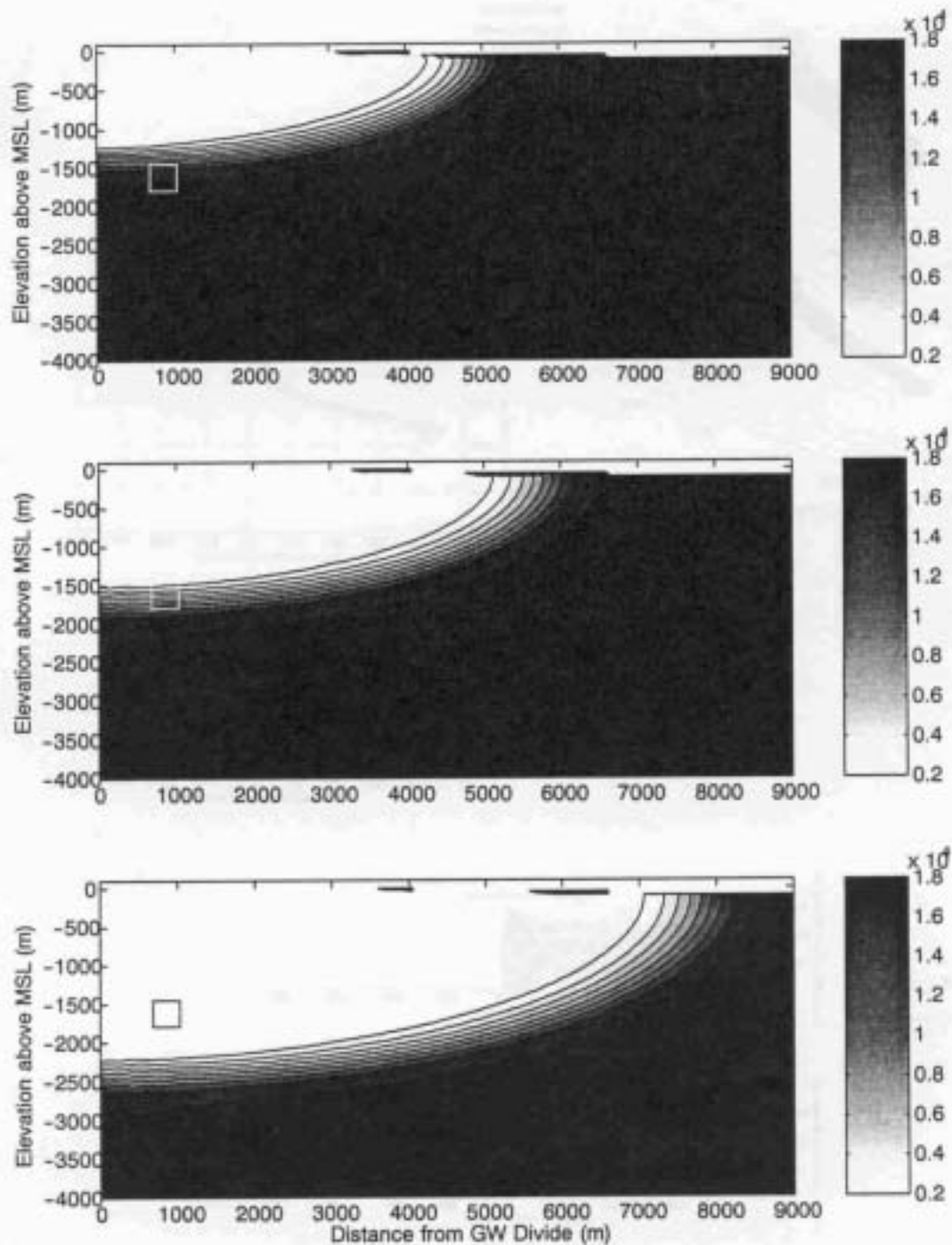
Figure 6.27. Salinity in the island groundwater system, expressed as concentration of chloride in mg/L, for the three sensitivity realizations in 3-D without incorporating the nuclear chimney. Compared to the 3-D case with the chimney (Figure 6.25), the transition zone occurs shallower.

213
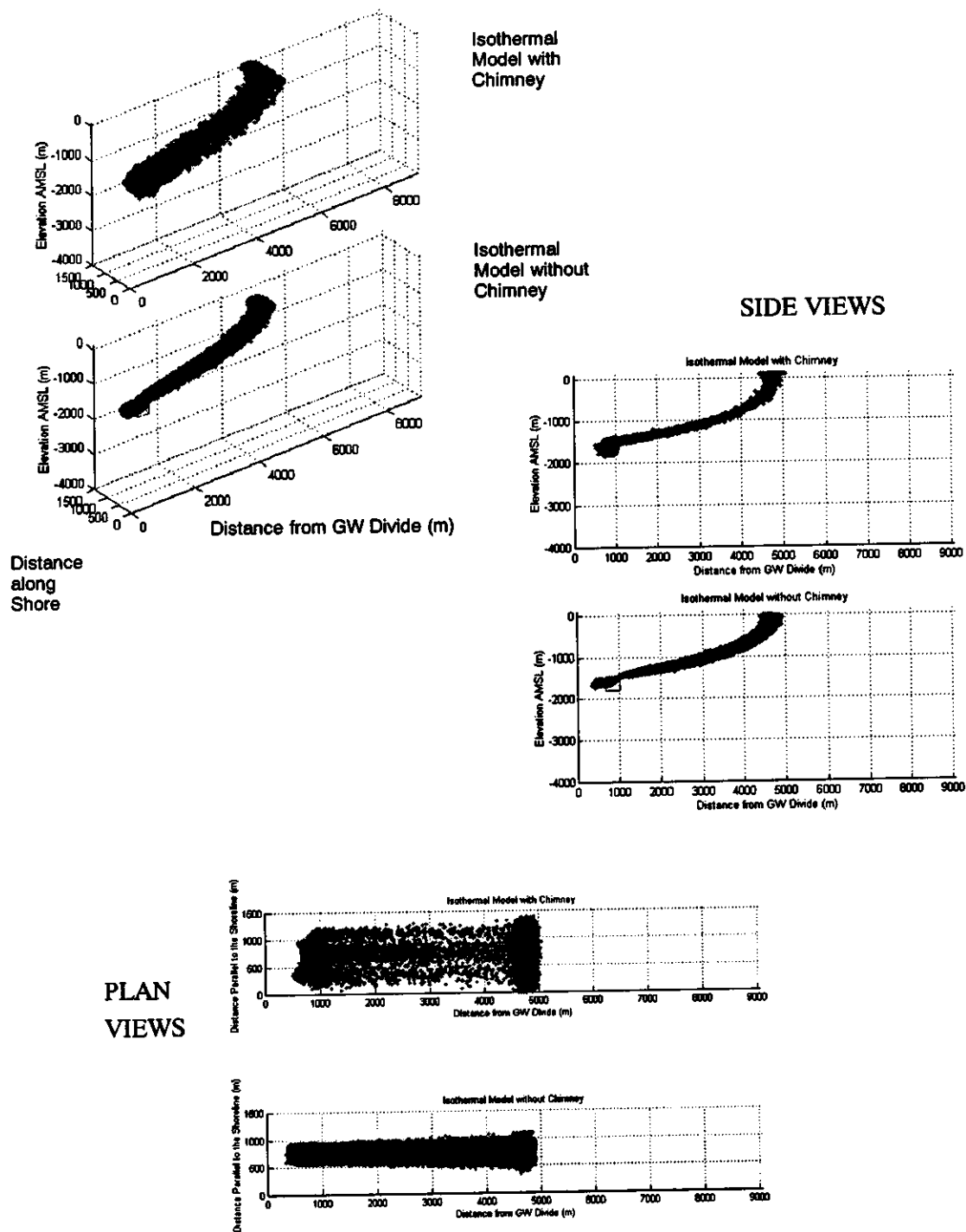
Figure 6.28. Particle trajectories for flow in the Cannikin domain with and without the nuclear chimney simulated, for 3-D realization #1.
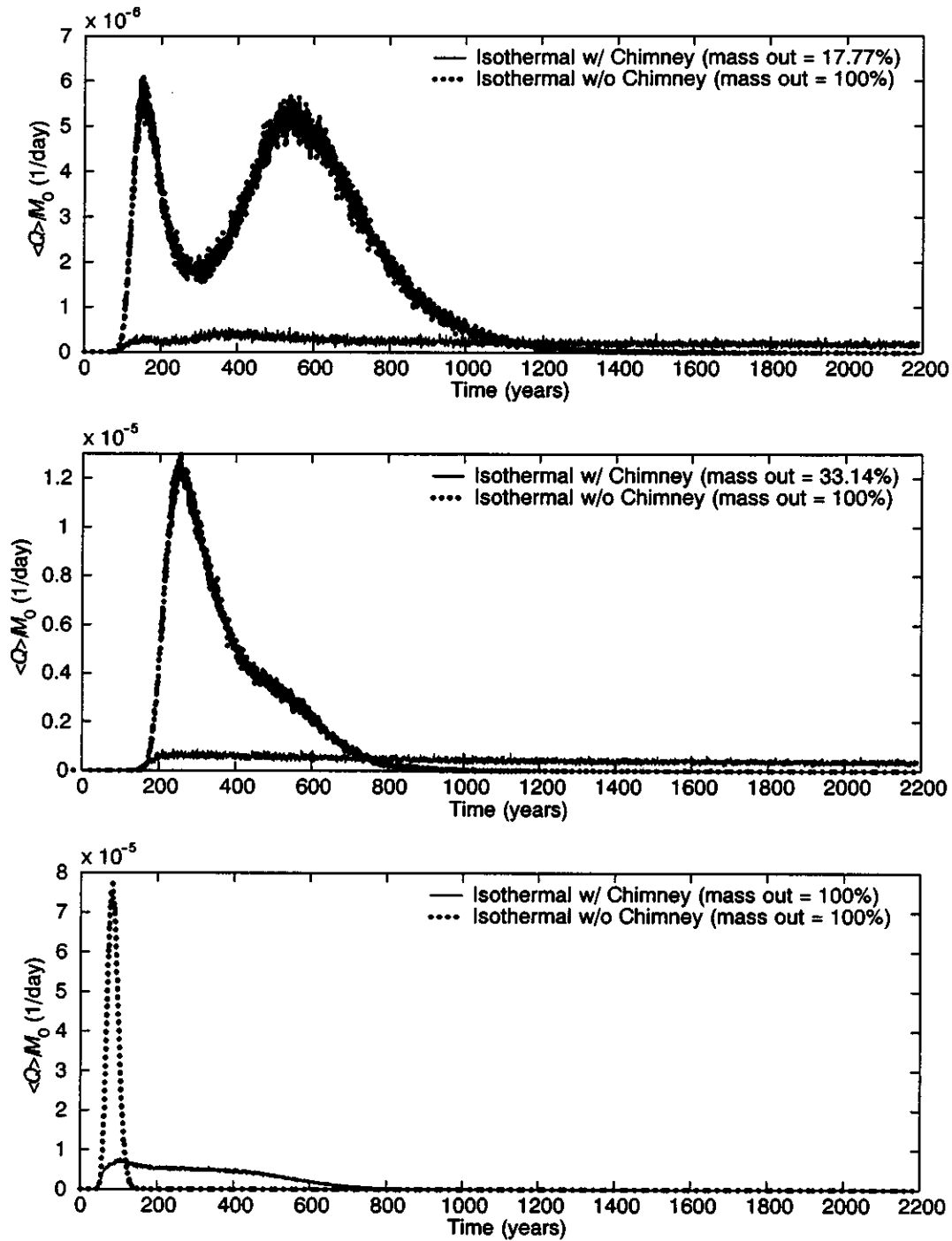
Figure 6.29. Breakthrough of undecayed, non-retarded, particles in a 3-D isothermal flow field with and without a nuclear chimney simulated. Each graph represents a different case of recharge/conductivity ratio for the three selected realizations.

215

the transition zone, but rather is due to the large difference in effective porosity between the chimney and the aquifer. The chimney porosity is 7.0×10^{-2}, based on observations of infill behavior, whereas the aquifer porosity in these three realizations is 2.67×10^{-4}, simulating fracture flow. The time of initial and peak breakthrough is approximately the same for the chimney and non-chimney cases; this indicates that for the chimney case, it is those particles very near the cavity edge (which rapidly escape the cavity to enter the undisturbed aquifer) that account for the first breakthrough. The lower mass for the peak breakthrough in the chimney case reflects the small percentage of particles that have that position. The remainder of the mass is released over hundreds of years as it moves at slow velocity through the cavity and chimney.

6.2.2 Cannikin Lake

The Cannikin explosion cavity was created instantaneously by the nuclear test, and 38 hours later the overlying material collapsed into the void and chimneyed up to land surface. A closed depression was formed, but rather than a circular crater centered on ground zero as typically seen at the NTS, an asymmetric, roughly triangular-shaped collapse occurred, centered over a point about 360 m southeast of ground zero. The form of the sink is controlled in part by one northwest-trending and two east-trending faults (Morris and Snyder, 1972). The maximum amount of subsidence is about 12 m (Morris, 1973). Morris and Snyder (1972) suggest that the displacement of the sink relative to the cavity may be related to stoping normal to the lithologic bedding planes as the roof of the cavity failed along successive bedding surface during collapse.

Eighty-four percent of the White Alice Creek drainage area was temporarily transformed into a closed basin and nearly all the flow was diverted toward the cavity (Gonzalez, 1977). There was no visible filling of the depression for more than 10 months, a period interpreted as the time that the cavity and chimney were resaturating. Starting in September 1972, a lake began to form in the depression, and Cannikin Lake was filled in December 1972 when overflow into the lower reach of White Alice Creek occurred and on to the Bering Sea. The surface area of the lake is reported as $121,400 \text{ m}^2$, with a maximum depth of 10 m (Dudley et al., 1977).

Though part of Cannikin Lake probably does not overlie the chimney directly, the relationship between the filling of the Lake and infill of the cavity and chimney (as reported by Claassen, 1978) demonstrates that there is some hydrologic connection between the features. The impacts of the formation of Cannikin Lake subsequent to the Cannikin nuclear test were investigated using an isothermal 3-D density-dependent flow and mass transport model utilizing the FEFLOW code. The 3-D model incorporating the rubble chimney was modified to include the lake as a zone of specified-head nodes on the top boundary. Other than this modification, the finite-element mesh geometry, the hydrogeologic features (including the chimney), and the other boundary conditions remained unchanged from the chimney model. As was done for the chimney model, the flow and mass transport model incorporating Cannikin Lake is comprised of three cases of recharge-conductivity ratio that cover the range of breakthrough behavior. The values of the parameters used in this flow and mass transport model are the same as those used in the 3-D model that included the rubble chimney.

216

Cannikin Lake is represented as specified head nodes within a zone at ground surface having horizontal dimensions of 600 m by 200 m (surface area of 120,000 m^2), with the long axis oriented parallel to the direction of natural groundwater flow toward the sea (Figure 6.30). Although there is uncertainty as to the nature of the hydraulic connection between the lake, the shallow groundwater system and the chimney itself, the model simulates the lake as covering two thirds of the chimney and being in direct hydraulic connection with it at ground surface. The hydraulic head specified for the lake is determined from the steady-state head simulated near ground surface at the inland edge of the chimney in each of the three cases of the rubble chimney model discussed in section 6.2.1. For each case, this head value is assigned to all boundary nodes on the top surface that are located within the zone of the lake. Under pre-lake steady-state conditions, the profile of hydraulic head at the top of the aquifer generally slopes toward the sea, interrupted only by a depression in head over the more permeable rubble chimney. With the addition of the lake, hydraulic heads (represented by
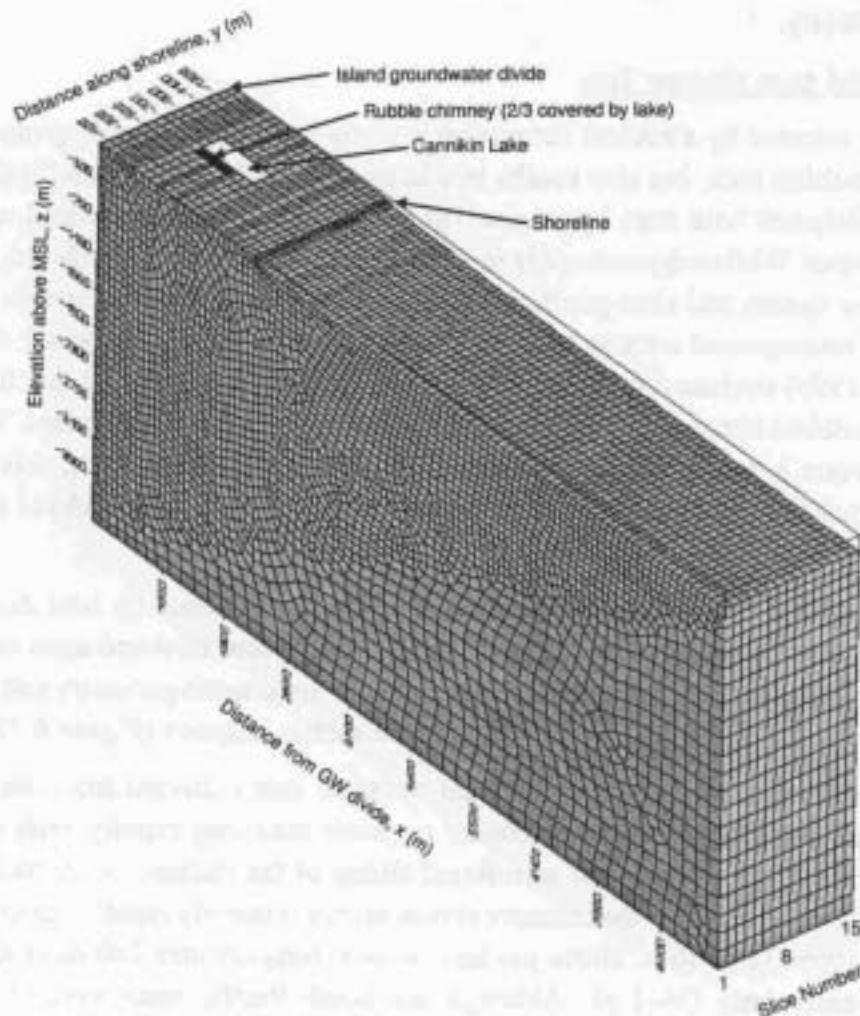

Figure 6.30. Design of finite-element mesh used for the 3-D model incorporating Cannikin Lake. All vertical layers are 100 m wide.

217

the lake elevation) range between about eight and 16 m above heads in the pre-lake underlying aquifer on the seaward edge of the lake, depending on the recharge-conductivity case. This large head difference provides a very large source of recharge to the rubble chimney and surrounding shallow aquifer that is maintained throughout each simulation, and limited only by the conductivity of the chimney and aquifer materials. The flow and mass transport model of FEFLOW is run until steady state is reached and the effects of recharge from the lake are fully incorporated in the distributions of concentration, head, and velocity. At this point the velocities are saved and used as input for the radionuclide transport models.

Examination of undecayed, non-retarded mass transport for the three realizations shows little change in the breakthrough curves for the three realizations (Figure 6.31). The percentage of mass breaking through at the sea floor is slightly higher for realizations 1 and 2 (by two to three percent for the cases with the cavity below and in the transition zone). These results suggest that the impact of neglecting the lake on the flow and transport results in section 5 is minimal compared to other sources of uncertainty.

6.2.3 Heat Derived from Nuclear Test

The energy released by a nuclear detonation is partly consumed through ground motion, and vaporizing and melting rock, but also results in a large increase in temperature in the cavity. This thermal pulse dissipates with time by conduction through the geologic material and convection through groundwater. While temperatures in the cavity region remain above ambient, they affect the groundwater flow system and alter geochemical reaction rates that are temperature dependent. In their analysis of underground nuclear tests in the South Pacific, the International Atomic Energy Agency (IAEA, 1998) evaluated the thermal impact of the tests. It was found that the temperature difference with ambient temperature decays to zero over a period of about 500 years. The hydrologic impact was to create a vertically upward flowpath above the cavity-chimney, driven by thermal buoyancy. Thermal impacts of the Cannikin test are investigated here to address concerns about buoyancy-driven movement of water heated by the nuclear test.

The impacts on flow patterns and radionuclide transport caused by heat derived from the Cannikin nuclear test are addressed using a 3-D density-dependent flow and mass transport model. These simulations are run using the FEFLOW code and the same mesh geometry and hydrogeologic features as used for the 3-D simulations of flow in the rubble chimney (Figure 6.32).

In an analysis of subsurface hydraulic and chemical data collected from the Cannikin test, Claassen (1978) reports that hydraulic recovery occurred relatively rapidly, with chimney voids nearly filled within 280 days after the test. Rapid filling of the chimney with cooler water from surrounding aquifers also caused the chimney region to cool relatively rapidly; cavity temperatures had declined to about 35 to 40°C above pre-test ambient temperatures 280 days after the test, as measured in re-entry hole UA-1-p1. Although the South Pacific tests were of much smaller magnitude than the reported yield of Cannikin, the IAEA (1998) reports that nuclear explosions in basalt result in temperature increases between 25 and 50°C, regardless of yield. IAEA (1998) also suggests that for the purposes of hydrologic modeling, the initial temperature increase is confined to a region within 1 R_c of the working point, because simulation of heat transfer by conduction
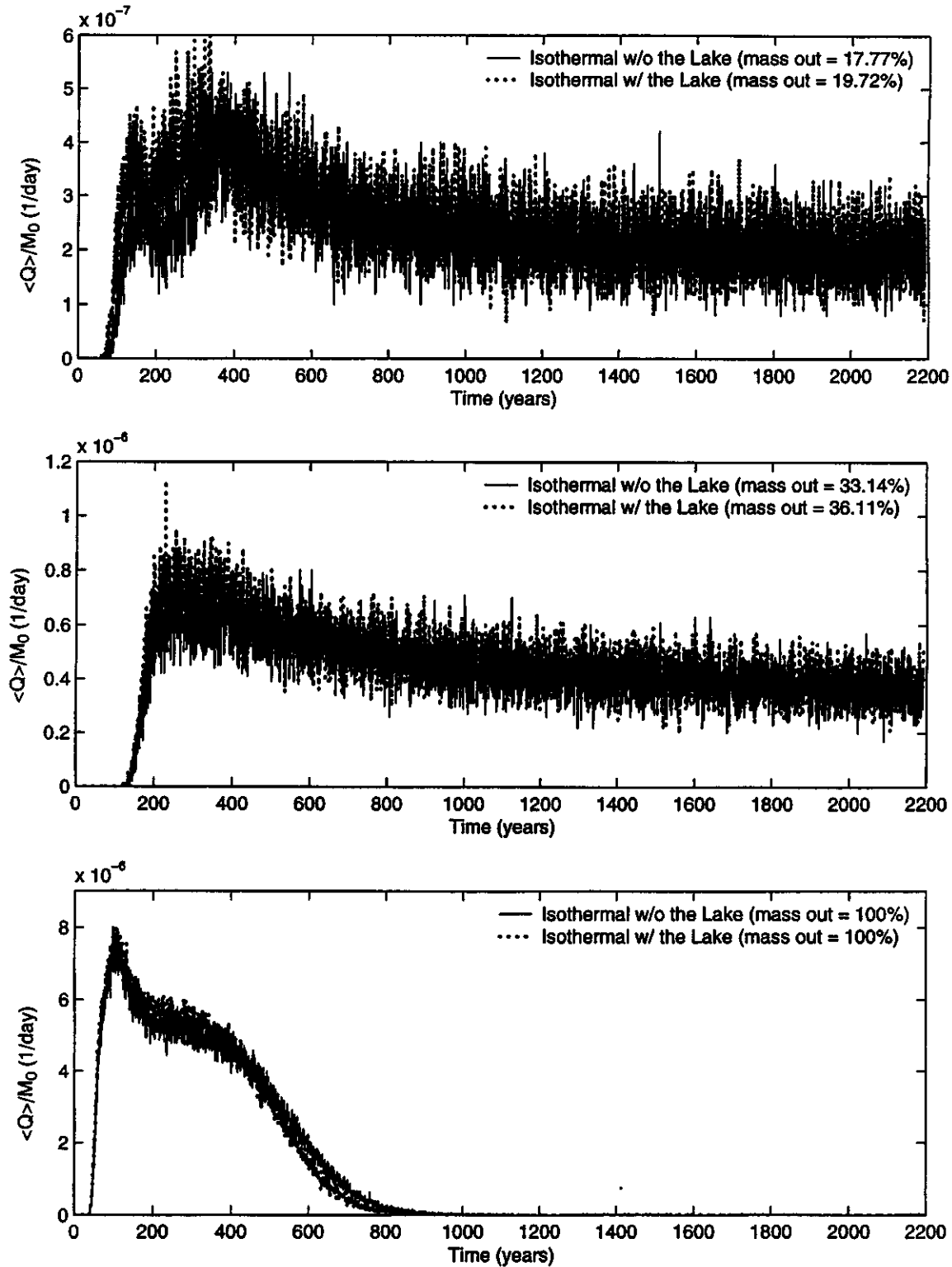
218

Figure 6.31. Breakthrough of a non-decayed, unretarded, solute using the steady velocity fields generated from isothermal simulations with and without including Cannikin Lake above the chimney.
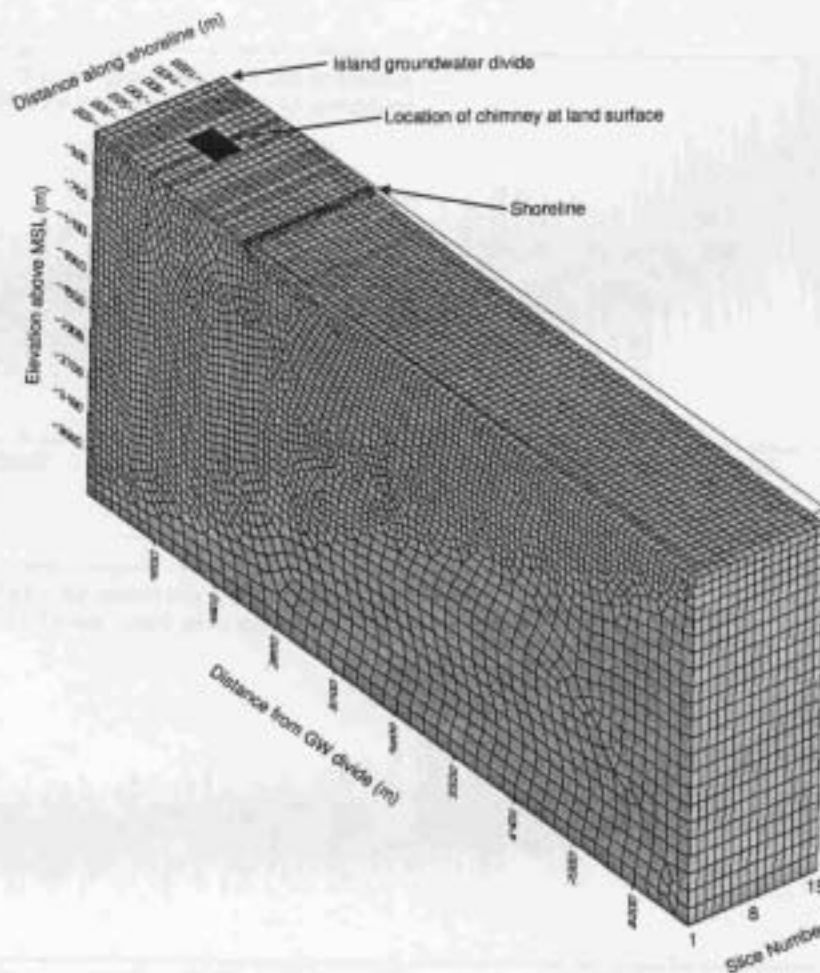
Figure 6.32. Design of finite-element mesh used for the 3-D model incorporating heat derived from the Cannikin nuclear test. All vertical layers are 100 m wide.

outside this radius will occur very slowly. In the present model, nodes within $1\ R_c$ of the working point are assigned an initial temperature of $50°C$ above the pre-test ambient temperature. All other nodes are assigned an initial temperature of $4°C$, the mean annual ground-surface temperature.

Three cases of the model are run, with values of the groundwater flow and mass transport parameters the same as the three cases of the 3-D chimney model, spanning the range of recharge/conductivity ratios included in the 2-D Monte Carlo analysis. The values of the thermal parameters are the same values used in the geothermal model (section 6.1.6). All of the values are shown in Table 6.6. Geothermal aspects would be overwhelmed by the large thermal pulse simulated here, so for reasons of computational efficiency, the geothermal process is not incorporated. Instead, the upper, lower, and right side temperature boundaries are assigned values of $4°C$.

Table 6.6. Values of parameters used in three-dimensional simulations incorporating heat derived from the Cannikin test.

Parameter	Realization #1	Realization #2	Realization #3	All Cases
Horizontal Hydraulic Conductivity, K_{xx} and K_{yy}	1.86×10^{-2} m/d	6.48×10^{-2} m/d	1.78×10^{-2} m/d	
Vertical Hydraulic Conductivity, K_{zz}	1.86×10^{-3} m/d	6.48×10^{-3} m/d	1.78×10^{-3} m/d	
Cavity and Chimney, K_{xx}, K_{yy} and K_{zz}	1.86×10^{-2} m/d	6.48×10^{-2} m/d	1.78×10^{-2} m/d	
Specific Storage, Ss				$1. \times 10^{-4}$
Recharge, $Rech$	6.13 cm/yr	3.33 cm/yr	1.89 cm/yr	
Fracture Porosity, θ	2.81×10^{-4}	2.71×10^{-4}	2.67×10^{-4}	
Chimney Porosity				0.07
Mass Longitudinal Macrodispersivity, A_L				100
Mass Longitudinal Macrodispersivity, A_T				10
Mass Diffusion, $D*$				1.0×10^{-9} m^2/s
Density Ratio				0.025
Rock Volumetric Heat Capacity, $\varrho_s c_s$				1.9×10^6 J/m^{3}C
Water Volumetric Heat Capacity, $\varrho_0 c_0$				4.2 J/m^{3}C
Rock Thermal Conductivity, λ_s				2.59 J/m^{3}C
Water Thermal Conductivity, λ_0				0.56 J/m^{3}C
Thermal Longitudinal Dispersivity, β_L				100 m
Thermal Transverse Dispersivity, β_T				10 m
Water Density and Viscosity, ϱ_0 and μ_0				6th order function of temperature
Initial Temperature in Cavity				54°C
Initial Ambient Temperature				4°C

The results show temperatures in the cavity region remain elevated above pre-test temperatures for hundreds of years (Table 6.7 and Figure 6.33). Within $2 R_c$ of the cavity, temperatures rise to no more than about 8°C above pre-test temperatures and show very slow declines to pre-test levels. Thermal effects are minor at distances greater than about $4 R_c$ from the working point.

Table 6.7. Locations of selected points around the Cannikin cavity and chimney where temperatures are presented in Figure 6.33.

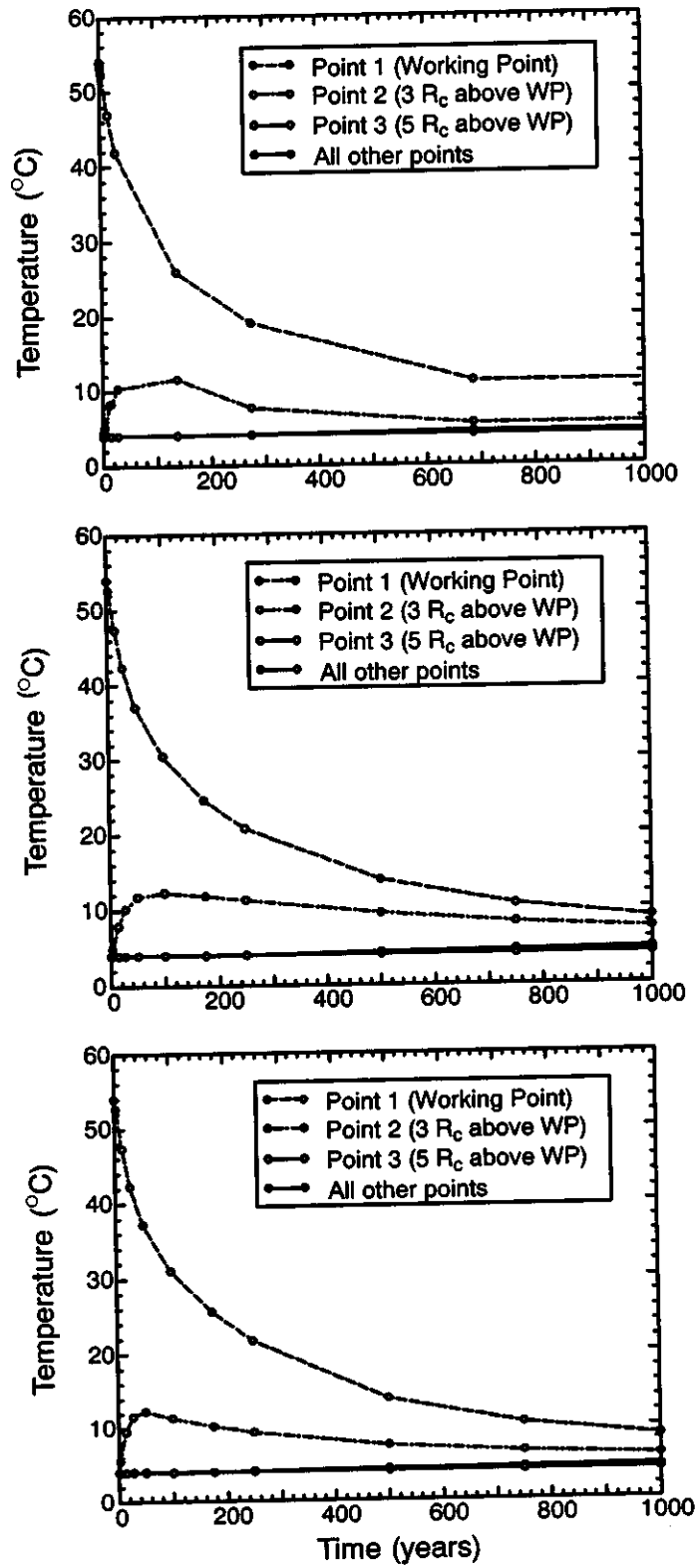| Point No.	Location
1	Working point (WP)
2	3 R_c above WP
3	5 R_c above WP
4	5 R_c below WP
5	3 R_c above and 5 R_c seaward of WP
6	5 R_c above and 5 R_c seaward of WP
7	3 R_c above and 5 R_c parallel to shore of WP
8	5 R_c above and 5 R_c parallel to shore of WP

Figure 6.33. Variation of temperatures at selected points around the cavity and chimney, following addition of heat derived from the Cannikin test. Each graph represents a different case of recharge-conductivity ratio.

The long-term elevated temperatures within the cavity cause thermally driven buoyant flow in the cavity region for several hundred years. With the exception of the center of the cavity, upward Darcy velocities within $2R_c$ of the working point reach maximum values about fivefold higher than pre-test ambient values, followed by slow declines. Horizontal flow is enhanced as increased vertical flow in the cavity/chimney drives lateral flow into the base of the cavity and out of the chimney above the cavity. Though a maximum twentyfold increase in the vertical and horizontal components of Darcy velocity is simulated at the working point, other points within $2R_c$ show less than fivefold increases. Within $2R_c$, velocities return to near pre-test values within about 400 years. The effects of heat-driven buoyant flow are small beyond $4\ R_c$ in both vertical and horizontal directions.

The addition of thermal energy from the nuclear test has a limited impact on the position of the transition zone for the three cases evaluated (compare Figure 6.34 and Figure 6.25). The simulations with thermal input have slightly shallower transition zones, presumably due to thermal buoyancy. Mixing induced by thermal convection cells is noticeable, however, when particle movement is tracked. Increased spreading in the y-axis direction (parallel to shore) is easily seen for realization #2 (Figure 6.35) and is believed to result from thermally driven flow exiting radially from the chimney. The nuclear test heat drives some particles upgradient, thereby increasing their flowpath length to the sea (Figure 6.36). This increased spreading may result in some particles being effectively stranded in low velocity portions of the flow field once the heat pulse decays. This is not observed in the transport results here because transport was calculated for the velocity field at 100 days after the test, not on the transient velocity fields. As a result, some of the particles simulated at the seaward edge of the domain, particularly for realization #3 (Figure 6.37), would not be expected to travel that distance in the transient flow field as they are located in the saltwater portion of the domain that will rapidly return to very slow velocities as the heat pulse decays. Indeed, the flow field directions return to near-steady state within 25 years of the test, so that particles forced counter to the steady-state gradient by the thermal pulse (particularly those moved into the saltwater portion of the domain) will then reverse, inducing a looping trajectory (Figure 6.38).

The impact of nuclear heat on the transport results varies greatly depending on the position of the cavity relative to the transition zone (and thus the recharge/conductivity ratio) considered. The evaluation of transport is performed for the velocity field at 100 days after the test, when the thermal impact is still very large; as such, it overestimates the impact of the thermal pulse by maintaining the high velocity field for the simulation time rather than allowing the velocities to decay. When the cavity is below the transition zone, the inclusion of the 100-day nuclear thermal effect causes a factor-of-three increase in the peak mass breakthrough, but the time of the peak breakthrough is considerably delayed over the isothermal case (Figure 6.39). Over the model period of 2,200 years, twice as much mass is calculated to discharge at the sea floor for the thermal case as compared to the isothermal calculations. The same general behavior is found when the cavity is within the transition zone, though the time delay between the isothermal and thermal peaks is greater and the difference in peak mass reduced to less than a factor of two. The overall increase in total mass discharged for the thermal case is one and one-half times the isothermal case. The impact of thermal conditions on transport when the cavity is above the transition zone is minimal compared to the
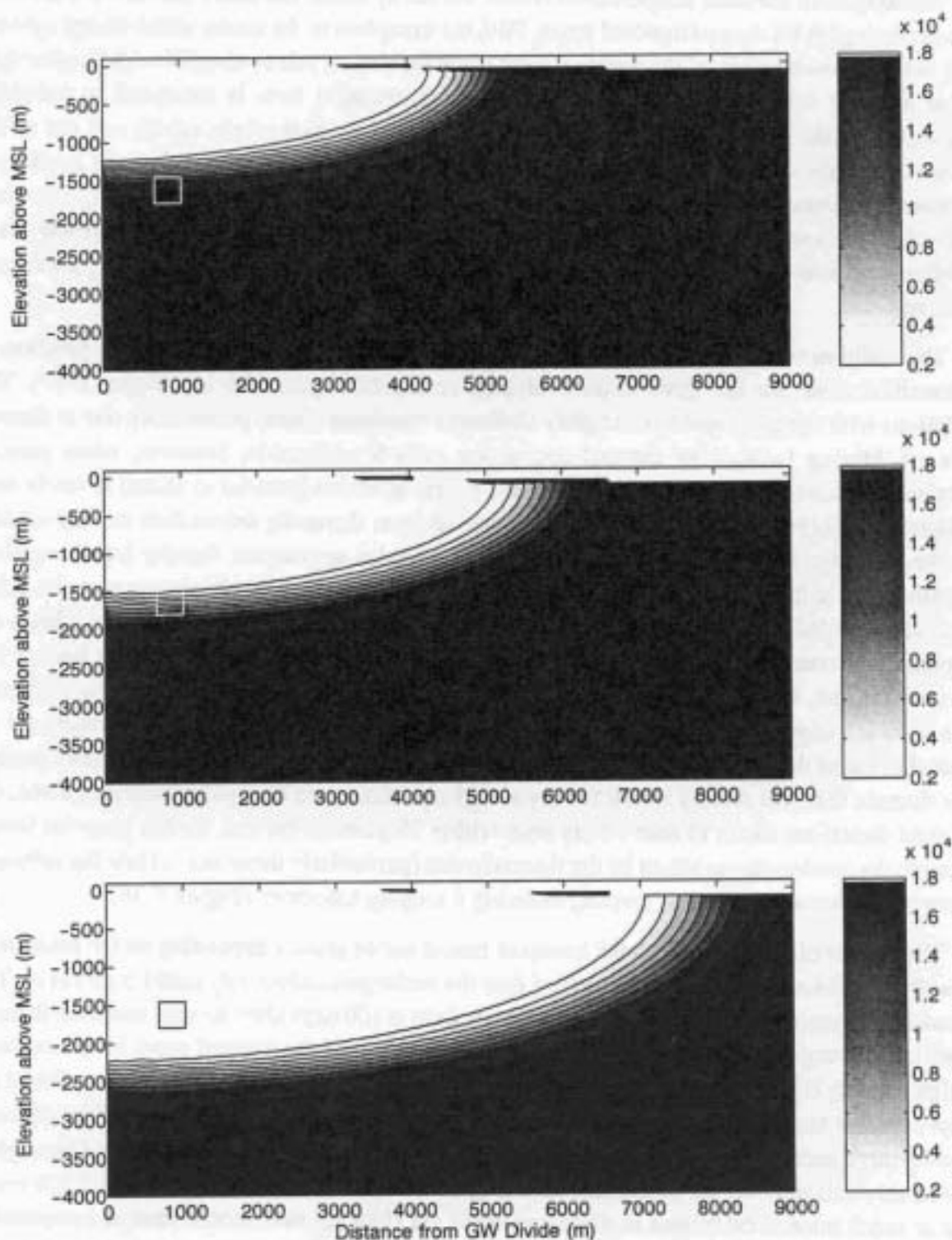
Figure 6.34. Salinity in the island groundwater system, expressed as concentration of chloride in mg/L, for the three select realizations, for the 3-D model including the nuclear chimney and heat from the nuclear test.
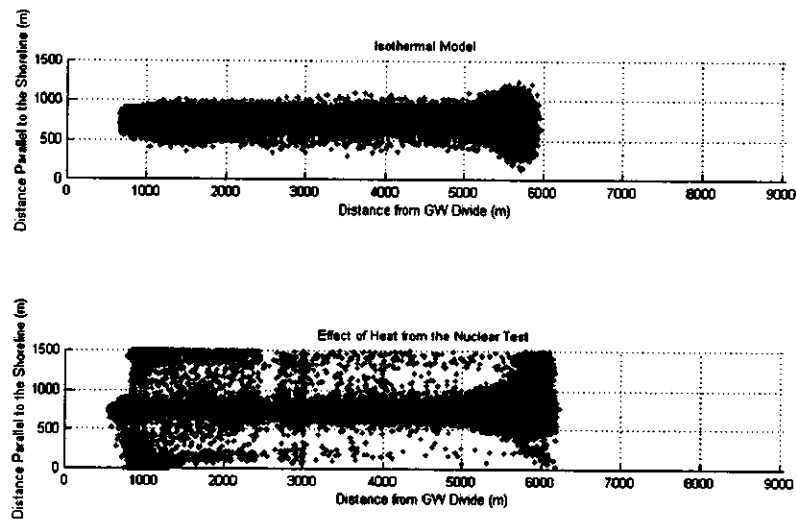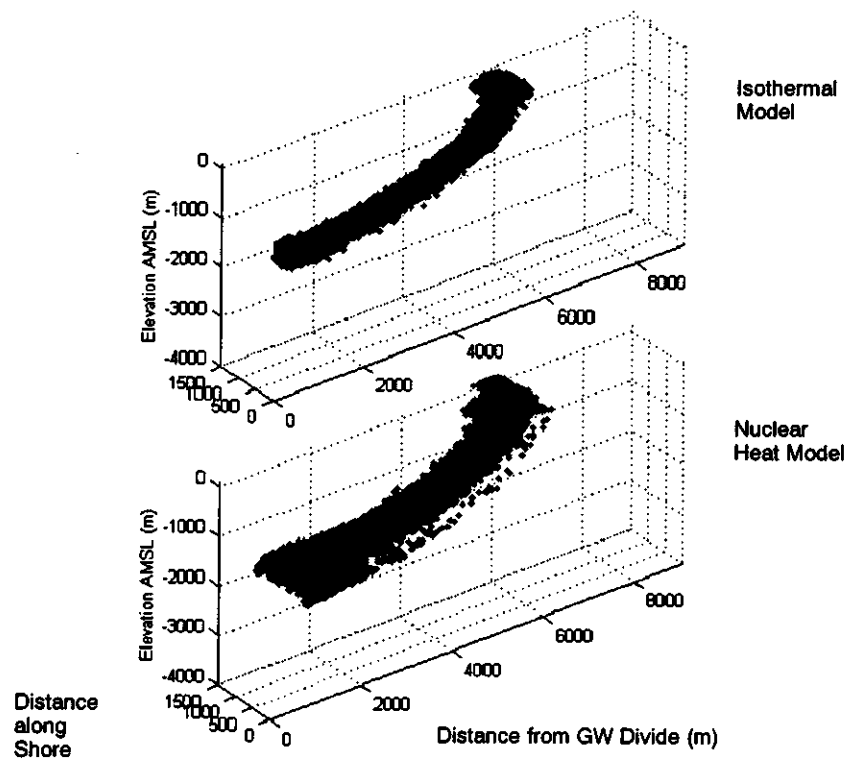
Figure 6.35. Particle trajectories from the Cannikin cavity with and without nuclear heat for realization #2 (cavity within the transition zone). The velocity field is representative of 100 days after the test.
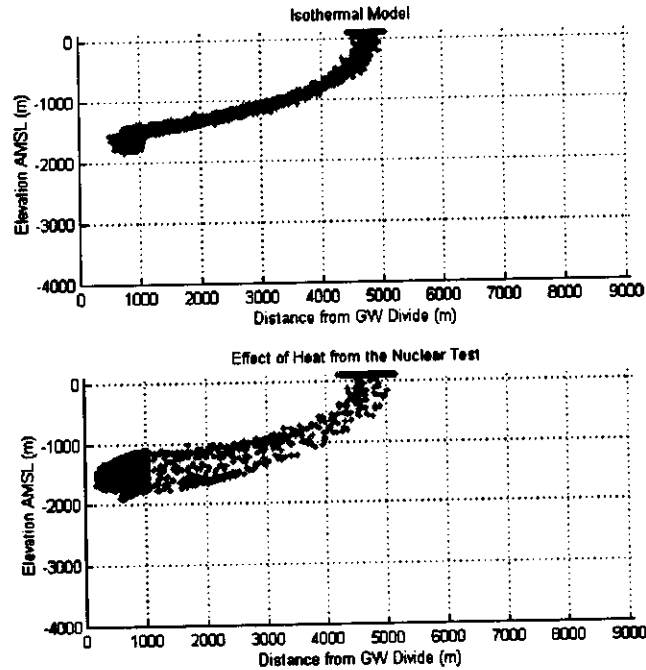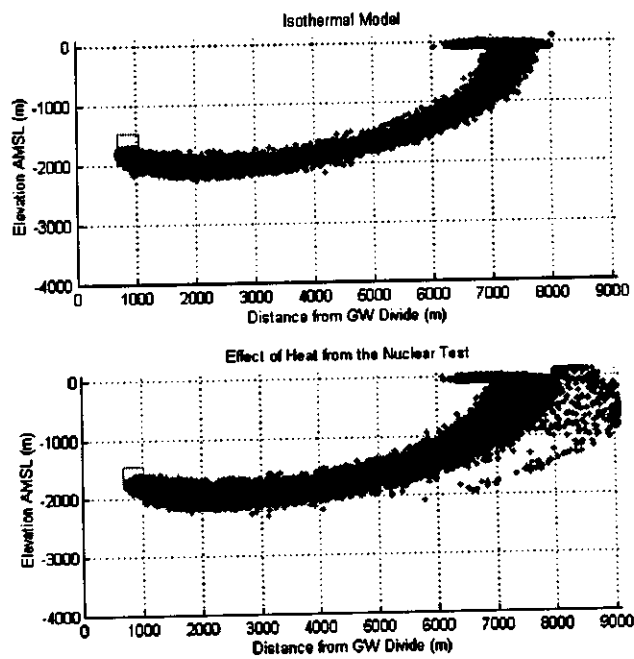
Figure 6.36. Cross section view of particle trajectories from the Cannikin cavity with and without nuclear heat for realization #1 (transition zone above the cavity). The velocity field is representative of 100 days after the test.
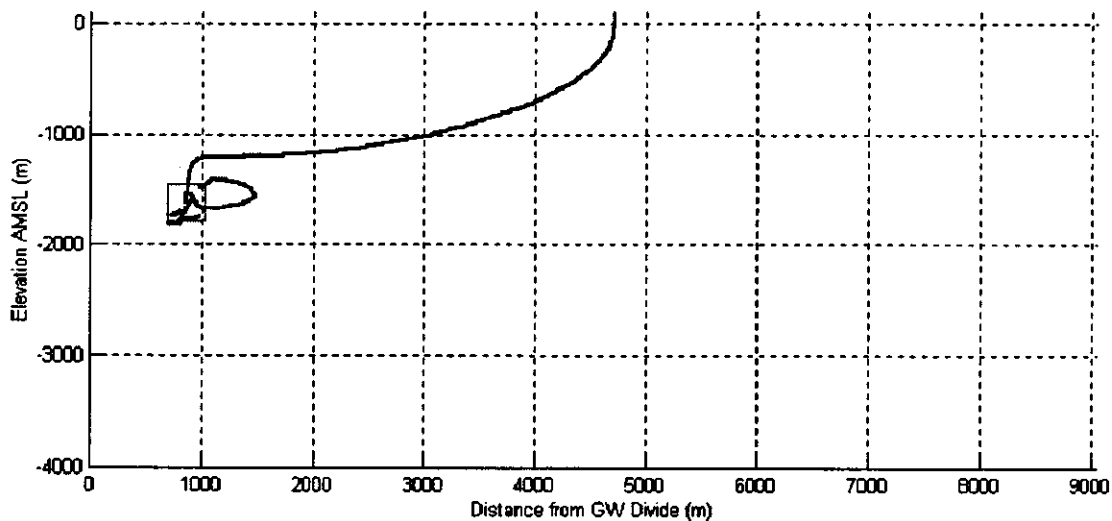

Figure 6.37. Cross-section view of particle trajectories from the Cannikin cavity with and without nuclear heat for realization #3 (transition zone below the cavity). The velocity field is representative of 100 days after the test.

Figure 6.38. A vertical 2-D view of particle trajectories showing the looping pattern in the 3-D thermal model with nuclear heat.

isothermal situation; the thermal peak is very slightly delayed and of slightly lower magnitude than the isothermal case, and both scenarios exhibit 100 percent breakthrough.

The thermal sensitivity runs indicate that neglecting the test-induced thermal effects is not significant for Long Shot and indeed, it is more conservative to not include the thermal process. The net result of neglecting the thermal impact for Milrow and Cannikin will depend on the half-life of the radionuclide considered. If tritium is the nuclide of concern, the isothermal case will be more conservative as it allows an earlier peak. Despite the higher mass calculated at later time for a non-decaying solute under thermal conditions, a short-lived radionuclide mass will decay to negligible amounts by the time the thermal-scenario peak arrives at the sea floor. In contrast, for a long-lived radionuclide that experiences limited decay over 1,000-year time frames, the thermal case will result in more mass being released over the model period, and higher peak fluxes.

6.2.4 Three-dimensional Formulation - Flow with Fault Zones

Numerous fault zones have been identified on the island by mapping lineation features on aerial photographs (Carr et al., 1966) and by analysis of shipborne magnetometer and seismic surveys (von Huene et al., 1971). Most of these faults strike in the east-northeast direction, roughly perpendicular to the axis of the island (Figure 1.4), and dip steeply. Carr et al. (1966) report that the fault zones are composed of highly fractured rock and may be up to thousands of feet wide, although little is known about whether these zones increase or reduce the permeability of the rocks they transect. If the fault zones have significantly lower permeability than the intervening rock, the faults will act as barriers to groundwater flow, with flow oriented parallel to them toward the sea. This is the flow pattern modeled in the 2-D cross-sectional models. However, if the fault zones are significantly more permeable than the surrounding rock, groundwater will flow preferentially toward the faults. The U.S. Army Corps of Engineers and USGS (1965) suggest that fault zones in the Banjo Point
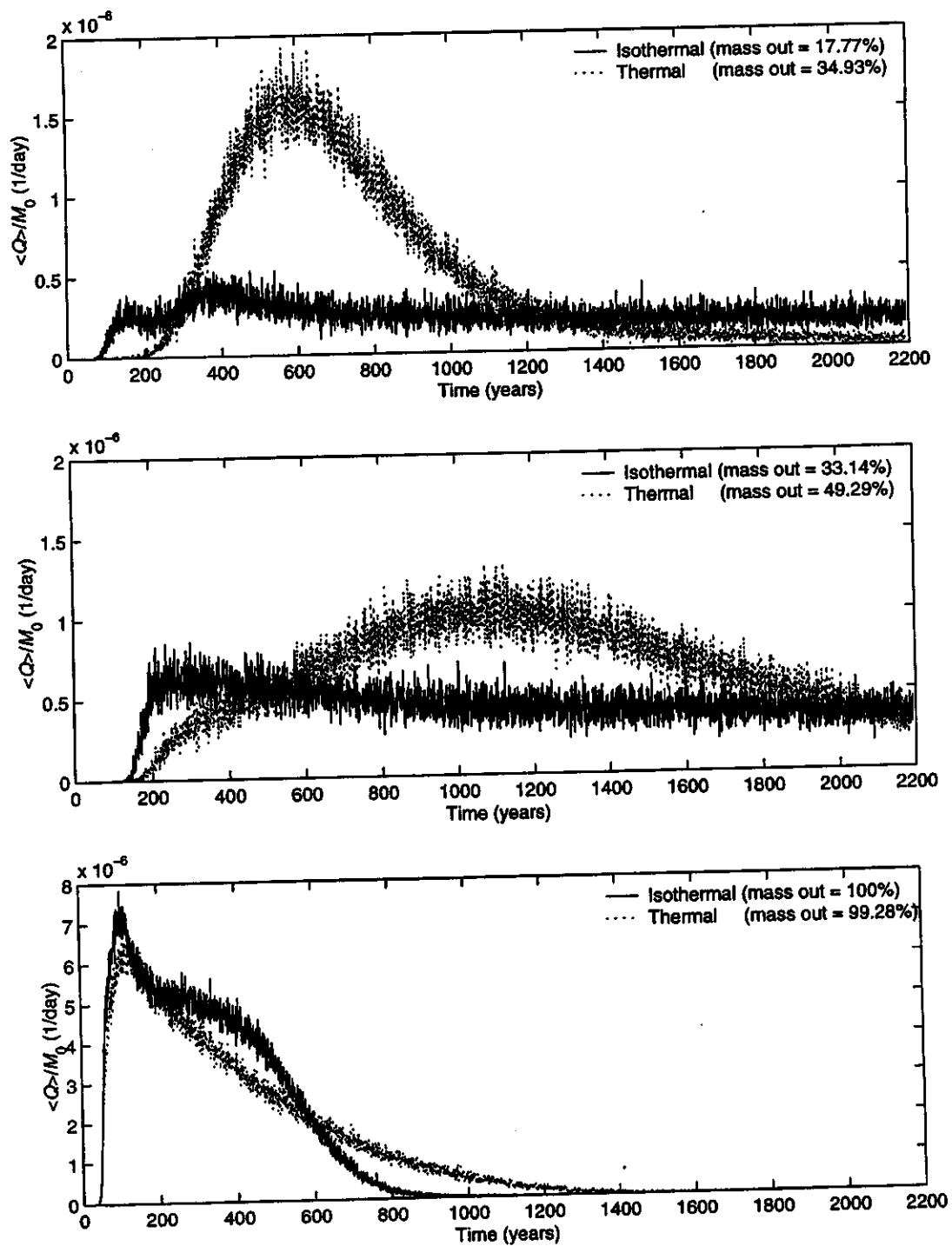
Figure 6.39. Breakthrough of undecayed, unretarded mass from a nuclear chimney with and without heat from the nuclear test. Each graph represents a different case of recharge/conductivity ratio for the three selected realizations.

Formation in the vicinity of the Long Shot site are at least ten times more permeable than the bulk of the formation. If the permeability contrast is sufficiently high, this scenario might produce fast pathways for flow from the chimney toward the sea.

The impacts on flow patterns and radionuclide transport caused by permeable fault zones are addressed here using isothermal, 3-D, density-dependent flow and mass transport models. The simulations are run using the FEFLOW code and a mesh geometry and hydrogeologic features that are similar to those comprising the rubble chimney models. The differences are the addition of one 5-m-wide layer on each outside lateral face of the model, and the addition of four 100-m-wide layers inside the model. The 5-m-wide layers represent fault zones and in the first fault scenario are assigned fault hydraulic conductivity values ten times the values in the unfaulted rock. In the second fault scenario, the faults are assigned hydraulic conductivity values 100 times the values in unfaulted rock. The horizontal to vertical K anisotropy ratio of 10 is maintained within the fault zones in both scenarios. The four additional 100-m-wide layers within the model increase the overall model width to 1,910 m, which approximates the width of the unfaulted structural blocks near Cannikin (Engdahl, 1972). The cavity and chimney are positioned midway between the fault zones at a distance of 800 m from each. Thus, the 3-D models simulate flow and transport within a single structural block bounded on the lateral faces by permeable fault zones. The faults are considered here to be preferred pathways of flow to the sea and do not allow flow across them (Figure 6.40).

Three cases of each fault scenario are run, with boundary conditions and values of the groundwater flow and mass transport parameters the same as the three cases of the 3-D chimney model (Table 6.8). The only differences are the increased K values in the fault zones, as previously described.

Table 6.8. Values of parameters used in three-dimensional simulations incorporating fault zones.

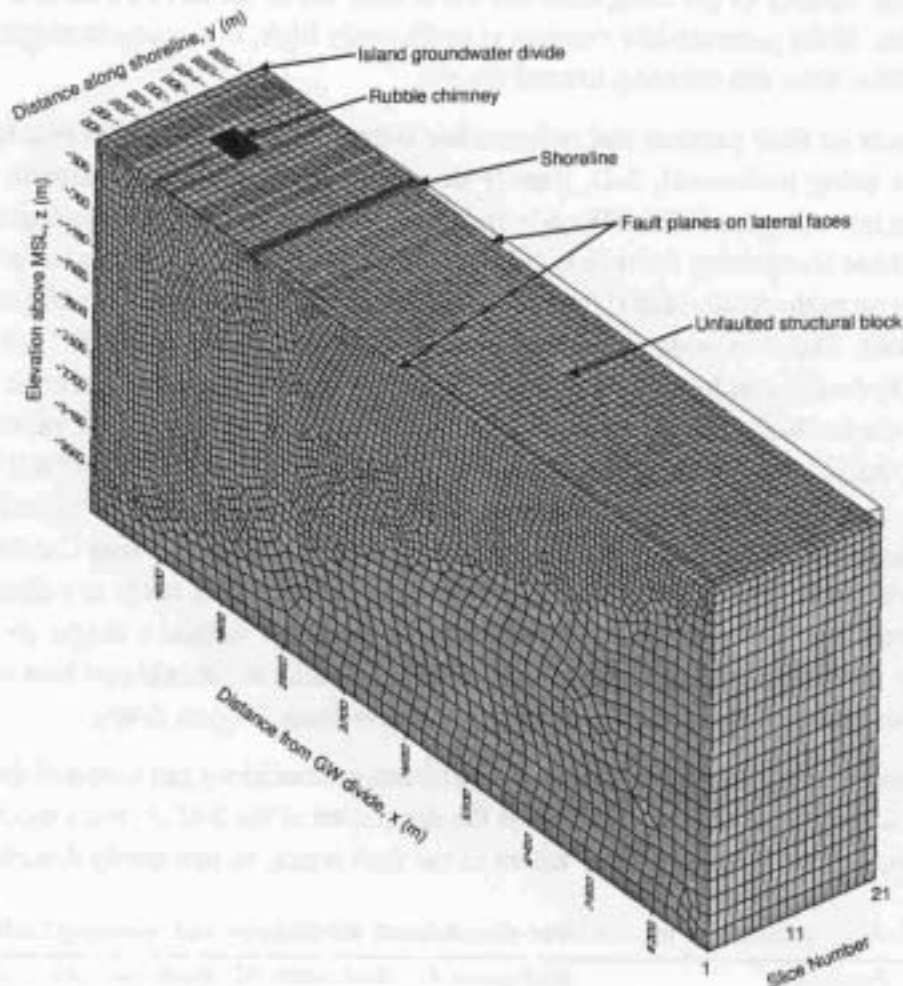| Parameter	Realization #1	Realization #2	Realization #3	All Cases
Horizontal Hydraulic Conductivity, Unfaulted Structural Block, K_{xx} and K_{yy}	1.86×10^{-2} m/d	6.48×10^{-2} m/d	1.78×10^{-2} m/d	
Vertical Hydraulic Conductivity, Unfaulted Structural Block, K_{zz}	1.86×10^{-3} m/d	6.48×10^{-3} m/d	1.78×10^{-3} m/d	
K_{zz} and K_{yy} of Fault Zones, Scenario #1	1.86×10^{-1} m/d	6.48×10^{-2} m/d	1.78×10^{-1} m/d	
K_{zz} of Fault Zones, Scenario #1	1.86×10^{-2} m/d	6.48×10^{-3} m/d	1.78×10^{-2} m/d	
K_{zz} and K_{yy} of Fault Zones, Scenario #2	1.86 m/d	6.48×10^{-1} m/d	1.78 m/d	
K_{zz} of Fault Zones, Scenario #2	1.86×10^{-1} m/d	6.48×10^{-2} m/d	1.78×10^{-1} m/d	
Cavity and Chimney, K_{xx}, K_{yy} and K_{zz}	1.86×10^{-2} m/d	6.48×10^{-2} m/d	1.78×10^{-2} m/d	
Specific Storage, Ss				$1. \times 10^{-4}$
Recharge, $Rech$	6.13 cm/yr	3.33 cm/yr	1.89 cm/yr	
Fracture Porosity, θ	2.81×10^{-4}	2.71×10^{-4}	2.67×10^{-4}	
Chimney Porosity				0.07
Mass Longitudinal Macrodispersivity, A_L				100
Mass Longitudinal Macrodispersivity, A_T				10
Mass Diffusion, D^*				1.0×10^{-9} m^2/s
Density Ratio				0.025

Figure 6.40. Design of finite-element mesh used for the the 3-D model incorporating fault zones near Cannikin. Layers 1 and 21 represent the 5-m-wide fault zones (but are too thin to be visible on this diagram). Layers 2 through 20 are 100 m wide and comprise the unfaulted structural block.

Inclusion of permeable faults is somewhat analogous to increasing K uniformly throughout the model domain, although the magnitude of the response is considerably less due to the limited areal extent of the more permeable zones. In the density-driven flow system modeled here, an increase in K generally causes the transition zone to be established at a higher elevation, as was shown previously for the 2-D case. Similarly, in the case of 3-D flow with fault zones, faults with K values 10 times greater than the unfaulted rock result in a slightly higher location of the transition zone, although the difference is well within the uncertainty of the measurements. Increasing the fault K further shows a greater impact on the transition zone; faults with K values 100 times greater than rock K start to dominate the flow pattern, causing the transition zone to be established at an elevation about 200 m higher (Figure 6.41 and Figure 6.42). The high contrast in K also is reflected in the upper portion of the head profiles, which show about a 4-m difference in head between the center
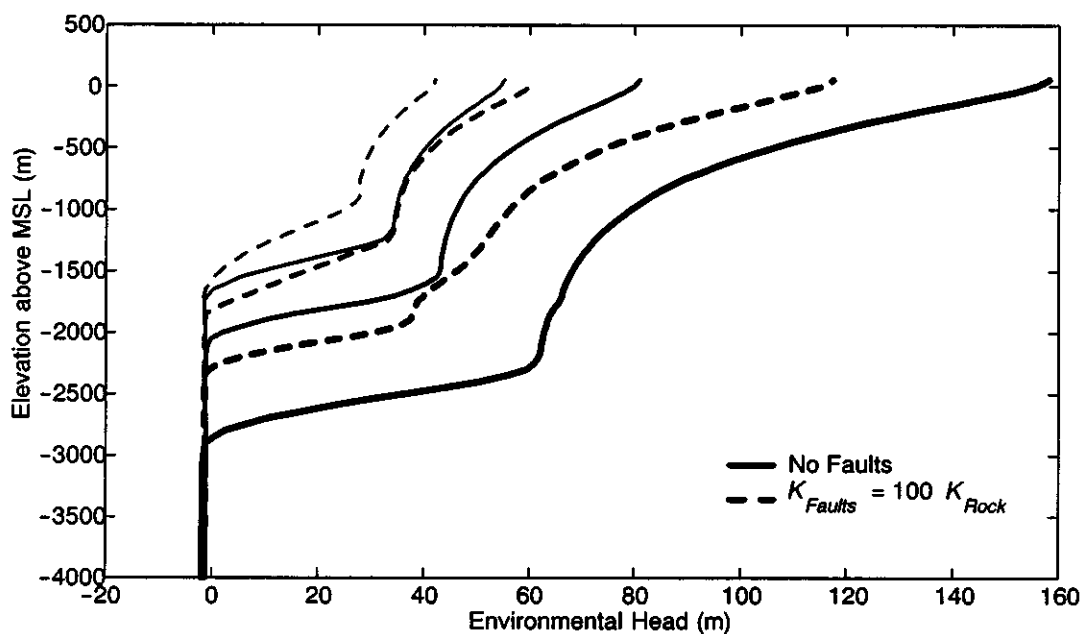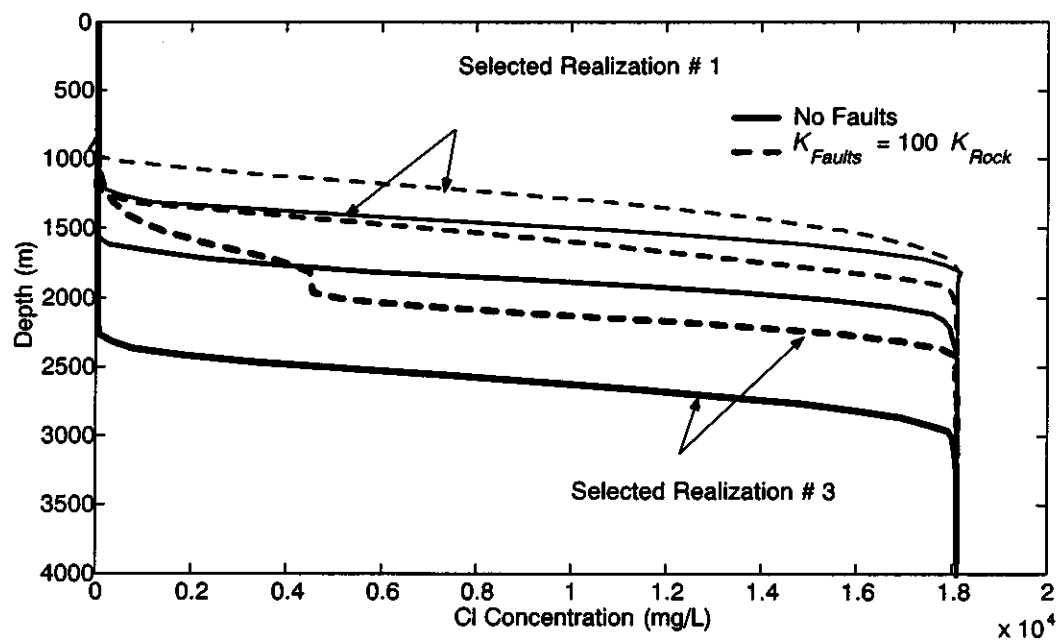
230

Figure 6.41. Profiles of concentrations and heads along a vertical line through the working point of Cannikin showing the effect of faults with K-ratio of 100.
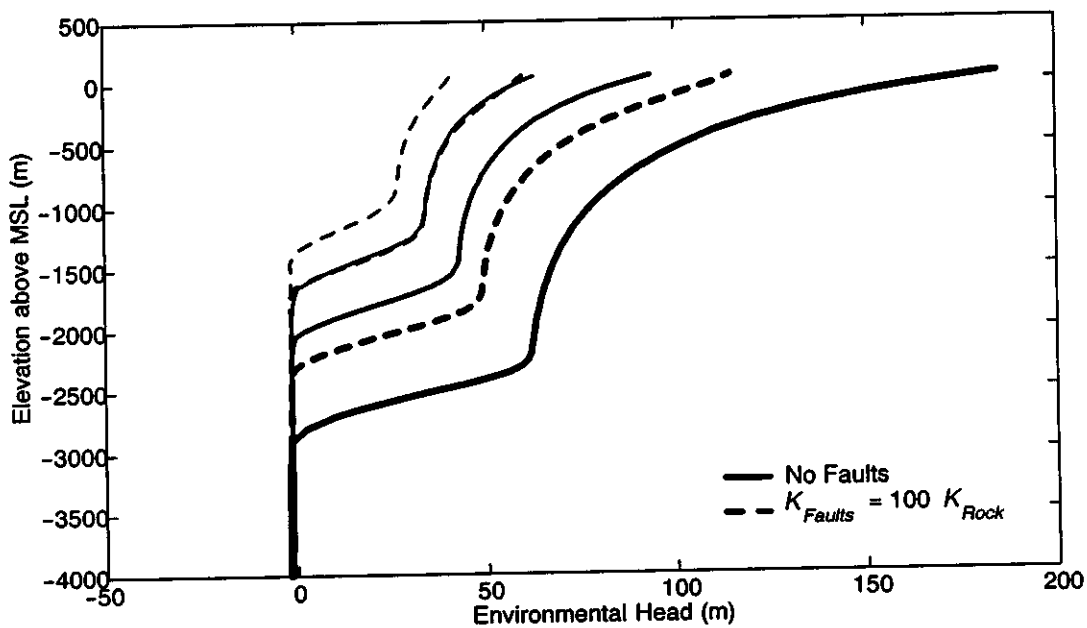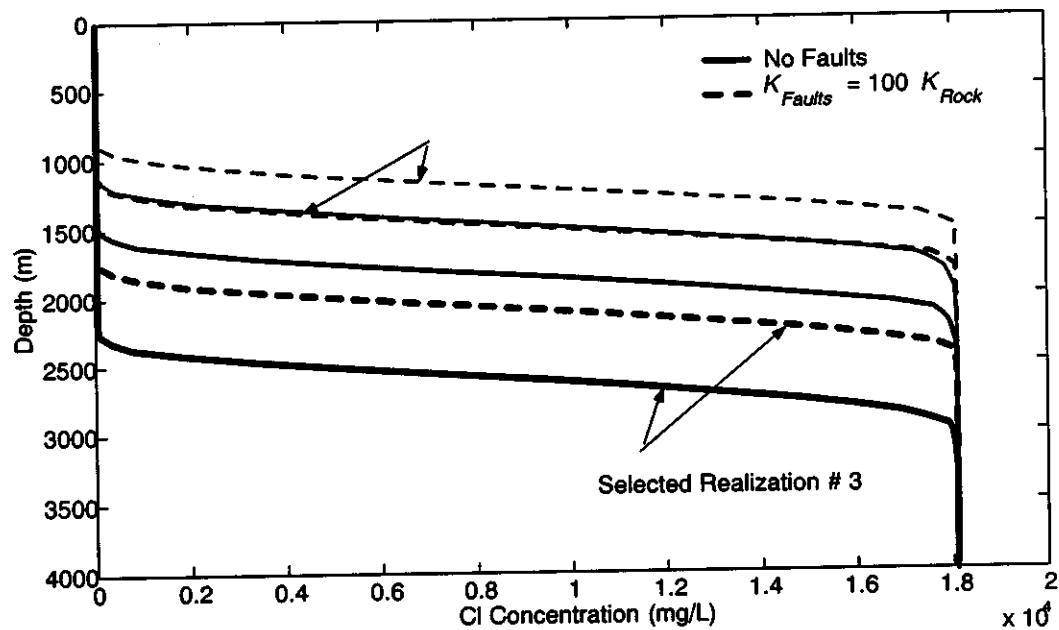
Figure 6.42. Profiles of concentrations and heads along a vertical line through the faults (at same x as the working point) showing the effect of faults with K-ratio of 100.

of the structural block and the edge. This head gradient has the effect of driving groundwater flow from the center of the model where the cavity is located, toward the faults.

The results of the flow model for the three selected realizations are analyzed in terms of transport of particles from the cavity to the seafloor. Figure 6.43 shows a snapshot of the particles' distribution at 2,200 years for selected realization #2 comparing the three-dimensional model with and without fault zones. The faults are assigned a conductivity value 100 times higher than the unfaulted rocks. The impact of the shallower transition zone is apparent on the 3-D and the vertical views. Particles break through between 4 and 5 km from the island axis in the faulted system, but they break through between 5 and 6 km in the unfaulted scenario. In the plan view of Figure 6.43, the impact of fault zones is most apparent where a strong lateral (parallel to the shoreline) preferential flow drives a large number of particles toward the faults in both directions. These particles then migrate along the transition zone within and parallel to the faults until they reach the seafloor. This selected realization has the cavity within the transition zone and the shallower transition zone resulting from the effect of the faults leads to the cavity being below the transition zone. Particles thus move upward with the saltwater and then shoot outside the cavity in the four directions: toward the sea, toward the island axis and toward the two faulted blocks. When the recharge-conductivity ration is large and the cavity is located above the transition zone as in selected realization #3, the impact of the faults on spreading the particles laterally is very minor as can be seen from Figure 6.45. This is to be expected since the dynamics of the freshwater lens and the velocity pattern therein are mainly controlled by the recharging freshwater. The high-K faults lead to a shallower transition zone and thus break through closer to the shoreline as compared to the unfaulted scenario.

The breakthrough curves for the three selected realizations and the comparison between the faulted and unfaulted cases are shown in Figure 6.45. Again, the impact of the faults depends on the location of the cavity with respect to the transition zone. The first realization shows an increase in the mass arriving to the seafloor and a higher peak of mass flux, but at a later time as compared to the breakthrough peak of the unfaulted scenario. The other two realizations (with cavity within or above the transition zone) show the same or lower mass arriving to the seafloor within 2,200 years and lower mass flux peak. As mentioned earlier, the significance of this impact depends on the radionuclide's half-life, with short-lived nuclides being more conservatively evaluated using the unfaulted scenario.
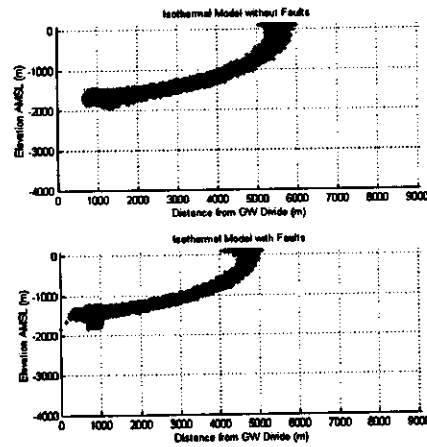
Selected
Realization
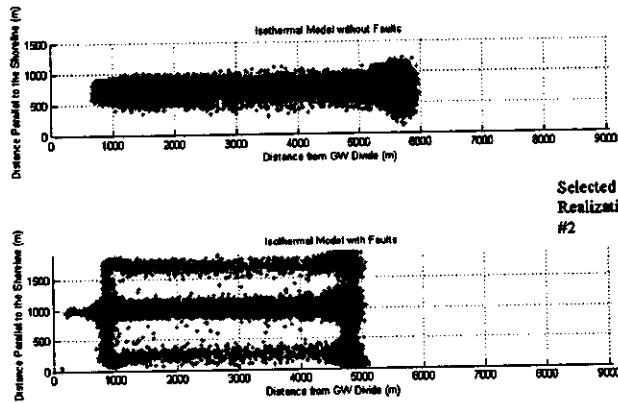#2
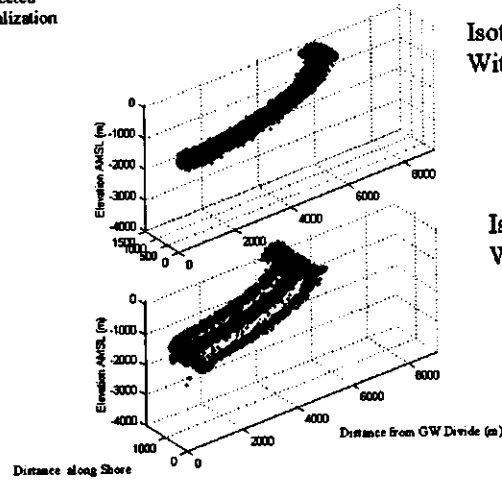
Isothermal Model
Without Faults

Isothermal Model
With Faults

$K_{Fault} = 100 \, K_{Rock}$
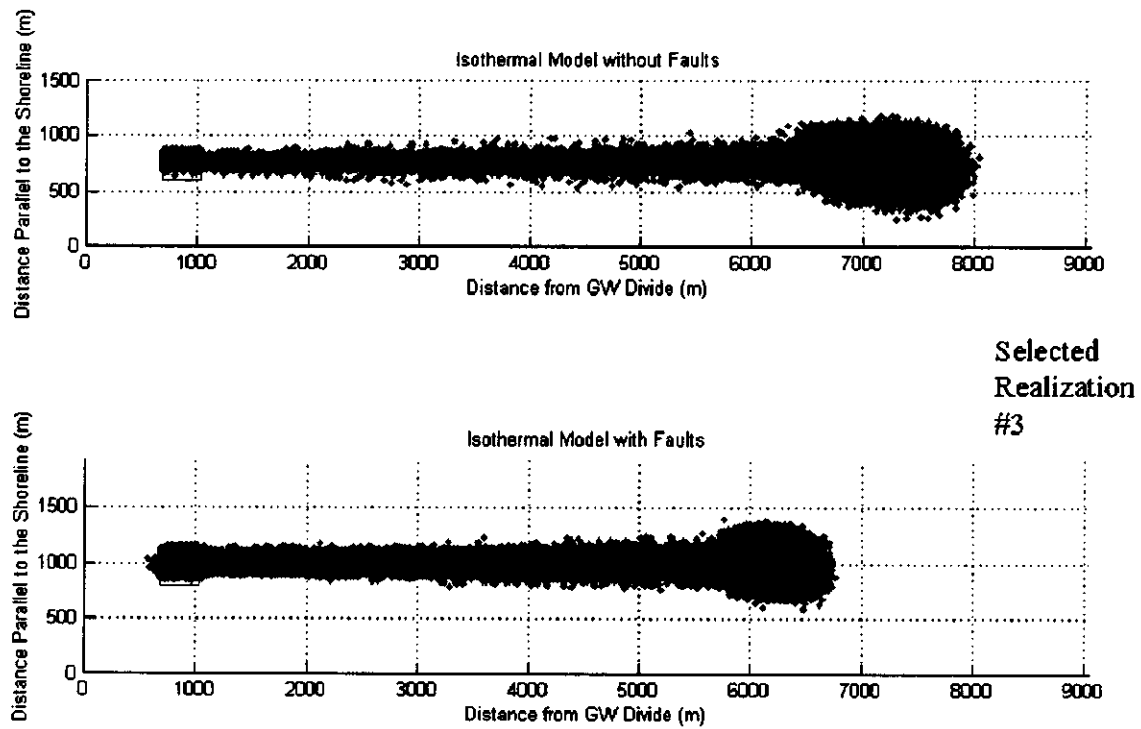
Selected
Realization
#2

$K_{Fault} = 100 \, K_{Rock}$

Selected
Realization
#2

$K_{Fault} = 100 \, K_{Rock}$

Figure 6.43.   Particle distributions comparing faulted and unfaulted scenarios for Cannikin 3-D model
for selected realization #2.

234

Figure 6.44. Plan view of particles' distribution for realization #3 showing the effects of faults when the transition zone is below the cavity.
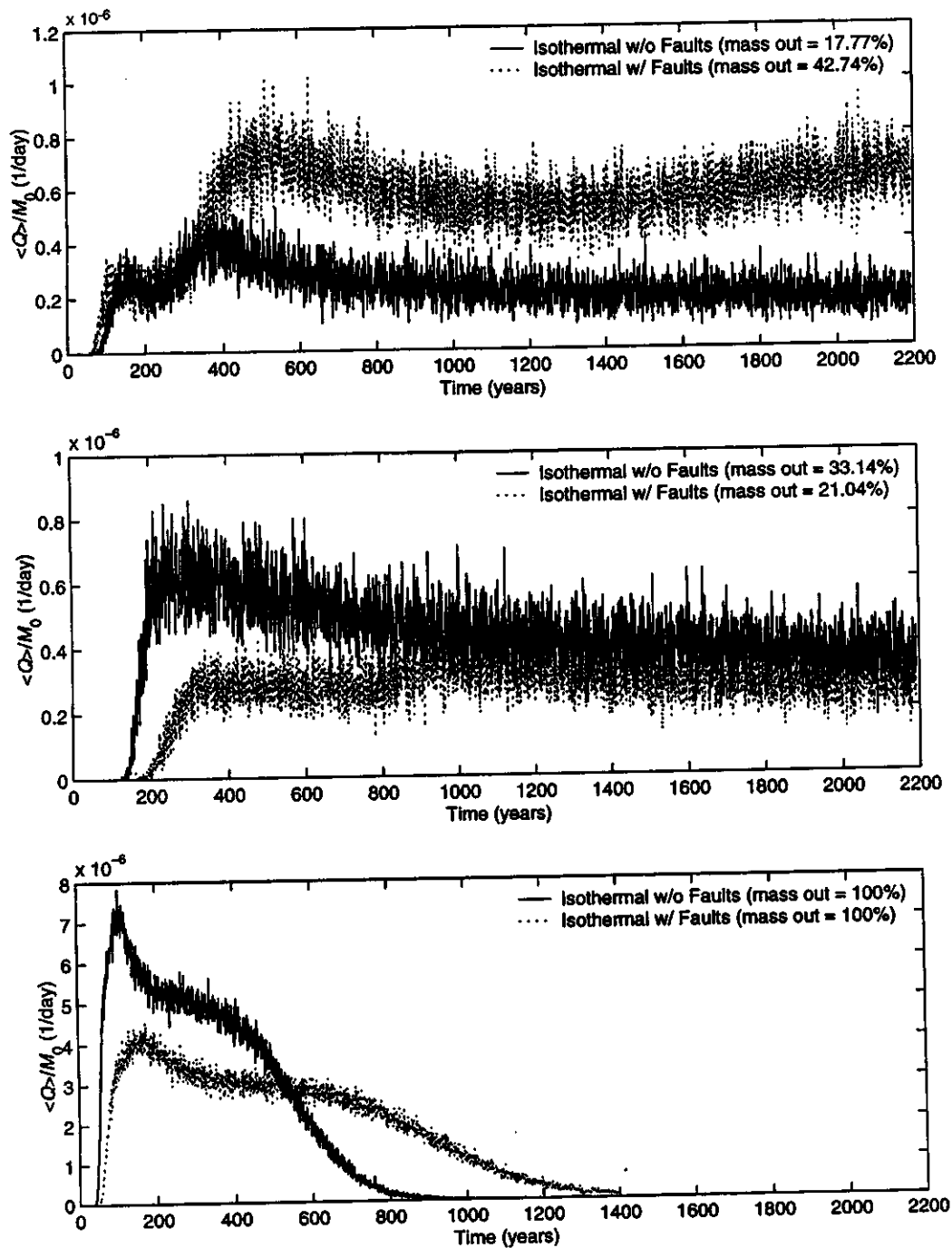
Figure 6.45. Breakthrough of undecayed, unretarded mass from Cannikin cavity with and without fault zones. Each graph represents a different case of recharge-conductivity ration for the three selected realizations.